MEASUREMENT AND IMAGE PROCESSING TECHNIQUES FOR PARTICLE

IMAGE VELOCIMETRY USING SOLID-PHASE CARBON DIOXIDE

THESIS

Mei-Ling Liber, Captain, USAF

AFIT-ENY-14-M-32

DEPARTMENT OF THE AIR FORCE
AIR UNIVERSITY

AIR FORCE INSTITUTE OF TECHNOLOGY

Wright-Patterson Air Force Base, Ohio

AFIT-ENY-14-M-32

MEASUREMENT AND IMAGE PROCESSING TECHNIQUES FOR PARTICLE

IMAGE VELOCIMETRY USING SOLID-PHASE CARBON DIOXIDE

THESIS

Presented to the Faculty

Department of Aeronautics and Astronautics

Graduate School of Engineering and Management

Air Force Institute of Technology

Air University

Air Education and Training Command

in Partial Fulfillment of the Requirements for the

Degree of Master of Science in Aeronautical Engineering

Mei-Ling Liber, B.S.M.E.

Captain, USAF

March 2014

AFIT-ENY-14-M-32

MEASUREMENT AND IMAGE PROCESSING TECHNIQUES FOR PARTICLE

IMAGE VELOCIMETRY USING SOLID-PHASE CARBON DIOXIDE

Mei-Ling Liber, B.S.M.E.
Captain, USAF

Approved:

//signed//	14 Mar 2014
Mark F. Reeder, PhD (Chairman)	Date
//signed//	14 Mar 2014
Maj James L. Rutledge, PhD (Member)	Date
//signed//	14 Mar 2014
Marcus D. Polanka, PhD (Member)	Date

AFIT-ENY-14-M-32

Abstract

Proper seeding material for particle image velocimetry (PIV) should not contaminate closed circuit wind tunnels and minimize residual deposits on walls. Solid carbon dioxide (dry ice) particles are ideally suited to meet this requirement. However, to obtain accurate velocity measurements, either particle size must be controlled or advanced image filtering and processing must be implemented. Both of these approaches are explored and advanced in the following research.

Refined data processing was conducted on previously collected turbulent boundary layer PIV data utilizing a similar particle generation system. The re-processed data trended more closely with corresponding pitot probe data than the original results. Free stream velocity measurements were within 0.97% of wind tunnel data free stream calculations.

Particle sizing measurements of solid-phase carbon dioxide (CO_2) were demonstrated in bench test experiments using an image-based approach. Dry air and gaseous CO_2 were introduced into a specific CO_2 injector in an attempt to control particle diameter, for diameters that ranged from 20 μm to 2800 μm. Average particle diameter was represented by an area-equivalent diameter and Sauter mean diameter. The greatest reduction in particle diameter was measured using dry air in conjunction with the CO_2 injector, where a 21% decrease in average area-equivalent diameter was observed. In contrast, there was only about an 8% decrease in the average area-equivalent diameter with gaseous CO_2.

Dry air was introduced into the same CO_2 injector for particle sizing experiments in the test section of an Air Force Institute of Technology (AFIT) Educational Wind Tunnel (EWT). Shadow images were taken at the inlet section of the EWT and at the test section for a comparison of the particle size distribution at each location. Changes in particle size with free stream velocity and increased mass flow rates of air were observed.

iv

Acknowledgments

First and foremost, I would like to sincerely thank my advisor, Dr. Mark Reeder, for his patience, guidance and encouragement throughout my research. Thank you for allowing me the opportunity to learn and giving me a story worth telling. Next, I would like to thank Mr. Chris Zickefoose, Mr. Jay Anderson and Mr. John Hixenbaugh, for their excellent support during my thesis. Chris, thank you for your help with the cameras and piping equipment. Jay, thank you for making sure I always had access to any equipment I needed. John, thank you for always going above and beyond in helping me, whether it was personally delivering dewars of carbon dioxide or accompanying me to the hardware store. I could not have completed this thesis without your help.

I'd like to thank my sponsors at AFRL: Dr. Larry Leny, Dr. Ryan Schmit, Capt Tim Cleaver, and Lt Mitch Haverkamp for helping me set up the experiment in the Educational Wind Tunnel and providing me with any equipment I needed. Mr. Ben Hagen, thank you for supporting me from the start a year ago and teaching me as much as you could about PIV. I really appreciated your expertise in experimental techniques and the background knowledge you gave me with the previous research.

A few unsung heroes worthy of a notable mention are Capt Mike Wilkinson and Lt Hayden Richards. It may have seemed small, but not the least bit unimportant!

Lastly, but certainly not the least, I'd like to thank Lt Col Tony Deluca for his advice that only previous PhD students can give. Thank you for helping me build a coherent path to succeed and keeping me on the right track. Capt Tan Van, thank you for being the most generous person I know.

Mei-Ling Liber

Table of Contents

List of Figures

xiii

List of Tables

List of Symbols

Symbol   Definition

A Surface area of a particle

C Characteristic frequency of particle motion

C_D Drag coefficient

δ Boundary layer thickness

δ^* Displacement thickness

d Magnification factor

d_p Particle diameter

D Displacement for all particles inside interrogation volume

D_{32} Sauter mean diameter

H Shape factor

I Image intensity field of first exposure

I' Image intensity field of second exposure

λ Wavelength of light

μ Dynamic viscosity of a fluid

m Refractive index of a particle

Q Peak validation correlation coefficient

ρ, ρ_f Fluid density

Symbol	Definition
ρ_p	Particle density
Re_p	Reynolds number with particle diameter as characteristic length
Re_x	Reynolds number with streamwise distance as characteristic length
s	Separation vector of particle displacement between exposures
St_k	Stokes number
τ_p	Characteristic response time of a particle
θ	Momentum thickness
Δt	Time between image capture
U	Local velocity
U_0	Free stream velocity
$\widehat{U}_f$	Instantaneous velocity of a fluid
$\widehat{U}_p$	Instantaneous velocity of a particle
$\widehat{V}$	Instantaneous relative velocity between a particle and fluid
$V_0(X)$	Interrogation volume of particles of first exposure
$V_0'(X)$	Interrogation volume of particles of second exposure
V_x	Streamwise velocity
V_y	Normal velocity
ξ	Same as τ_p

Symbol	Definition
x	Streamwise distance
x_i	Position of a single tracer particle
x_M	Particle scattering cross section
y	Coordinate normal to a boundary (such as a wall)

List of Acronyms

Acronym	Definition
AFIT	Air Force Institute of Technology
AFRL	Air Force Research Lab
Al_2O_3	Aluminum Oxide
BBO	Bassett Boussinesq-Oseen
CO_2	Carbon Dioxide
CCD	Charge-coupled device
CFD	Computational fluid dynamics
CMOS	Complementary metal-oxide semiconductor
CTA	Constant-temperature anemometry
DEHS	Di-Ethyl-Hexyl-Sebacat
EWT	Educational wind tunnel
FFT	Fast Fourier Transform
IPC	Individual particle correlation
ISSI	Innovative Scientific Solutions, Inc.
IR	Interrogation region
LDA	Laser-doppler anemometry
LED	Light-emitting diode
MgO	Magnesium Oxide
Nd:YAG	Neodymium-doped yttrium aluminum garnet
PSV	Particle shadow velocimetry
PTV	Particle tracking velocimetry
RMS	Root-mean square
SNR	Signal-to-noise ratio

Acronym	Definition
SLPM	Standard liters per minute
TiO_2	Titanium Dioxide
TGF	Trisonic Gas-dynamics Facility

MEASUREMENT AND IMAGE PROCESSING TECHNIQUES FOR PARTICLE

IMAGE VELOCIMETRY USING SOLID-PHASE CARBON DIOXIDE

I.   Introduction

THE study of fluid motion dates back to ancient civilization, where humans gained an understanding of hydrology needed for flood protection, irrigation, drainage and water supply [1]. Visualization of fluid flows, especially around objects, has always been a curiosity and goal to understand because of their homogenous and optically transparent natures. In 1904, Ludwig Prandtl suspended mica particles in his manually-powered water tunnel to study separated flow behind a wing [2]. This is the first documented example where a fluid was "seeded," or sprinkled with particles in order to understand the motion and description of the flow field. A similar experiment, visualized with more modern equipment, is shown in Figure 1.1. Although Prandtl's flow visualization method would be considered rudimentary by todays standards, it paved the way for the modern flow technique called particle image velocimetry (PIV).

Contemporary PIV uses tracers referred to as seed particles that are dispersed into a flow field. Unlike early researchers, who could only observe the mica particles with their own eyes, the seed motion is illuminated by a light source within a short time interval and captured on high-resolution digital cameras for 2-D or 3-D flow visualization. With his water channel experiment, Prandtl could only gain a qualitative understanding of the flow field. Today, velocity, vorticity, strain rate and other spatial gradients can be deduced from PIV due to the simple principle that velocity equals distance traveled divided by time. By illuminating the tracer particles on a "light sheet" at least twice within the plane of the
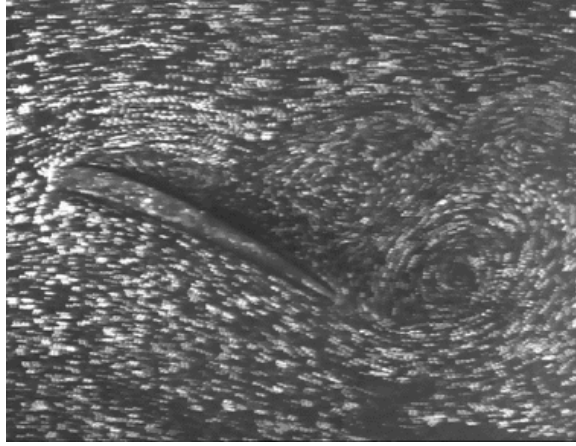
Figure 1.1: Replica of Ludwig Prandtl's water tunnel experiment with separated flow behind a wing [2]

flow and recording the light scattered by the particles on a sequence of frames separated by the time between illuminations, the distance of the particles can be determined by comparing the difference in position between the two successive frames [3]. Then, the velocity of the particles are calculated by dividing the distance of the particles by the time delay between illuminations. The process by which the velocity vectors are calculated is called correlation. Two grayscale images acquired digitally may be considered as a matrix of intensity, where bright pixels correspond to larger values and dark pixels correspond to lower values. Each image is then divided into sub domains called interrogation regions (IRs) that can vary in size, shape and concentration of particles present. An IR from the first image is correlated with its corresponding IR from the second image using the same process described previously to determine the pixel shift resulting in the best correlation of that region. With the known time between images, one velocity vector is generated per IR and ultimately represents the velocity of the particles within that region. Each IR is processed until the entire image domain in the planar cross section has been mapped with velocity vectors. This yields a near-instantaneous velocity field which can be added sequentially with the other velocity results and divided by the number of image pairs to determine the
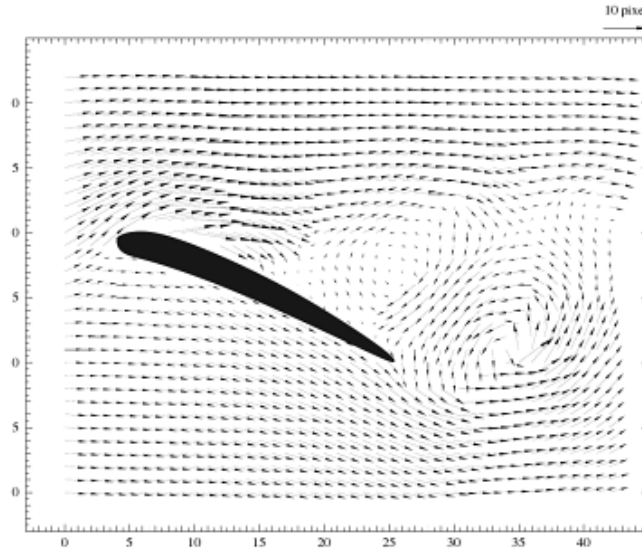
Figure 1.2: Sample PIV output of Prandtl's flow around a wing
[2]

average velocity field of a target region. A sample output of the instantaneous velocity corresponding to Figure 1.1 and computed using PIV is shown in Figure 1.2. Further details regarding the setup, components and processing of data for PIV will be discussed in Chapter 2.

Because of its ability to produce near-instantaneous velocity measurements of an entire flow field, PIV does not have the limitations of point-source experimental techniques such as laser-doppler anemometry (LDA) and constant-temperature anemometry (CTA). Generally speaking, it is a non-intrusive method; therefore it does not disrupt the flow profile. Another advantage is that results can be directly compared with computational fluid dynamics (CFD).

Challenges facing PIV stem from the development of technology components that lie outside the field, i.e., computers, lasers and cameras [4]. Limitations on spatial resolution (minimum distance between distinguishable objects in an image, such as pixels) and

temporal resolution (minimum time to process incoming data, as with a high resolution or high-speed camera) affect the accuracy and precision of the vector mapping in addition to the signal-to-noise ratio (SNR). On the post-processing side, algorithms for locating and pairing particle images with maximum reliability could be optimized. One of the most critical challenges, and the core focus of this thesis, is whether or not the seed particle motion corresponds precisely to the flow dynamics. Extensive research was conducted by Melling [5] to determine the tracking characteristics of different particles in a variety of flow fields, i.e., the discrepancy between the velocity of particles and the fluid. Melling calculated response times for various particle sizes in turbulent flow and downstream of an oblique shock. Results of his research quantified the "velocity slip" of heavy, large particles compared to small particles with a density close to that of the fluid. Ideal particles will match, or be close to the density of the fluid. In terms of size, the particles should be small enough that the response time of the particles to the motion of the fluid is short enough so that they accurately follow the flow, but must be large enough to scatter enough light from an incident light source. The determination for how well the particles follow the flow is governed by the Stokes' number. This non-dimensional parameter corresponds to the ratio of the characteristic time of a particle to a characteristic time of the the flow. For Stokes' numbers much less than 1, the particles are assumed to be tracking the flow accurately. For Stokes' numbers less than 0.1, the tracing errors become less than 1% [3]. Homogeneity of the particles is linked to spatial resolution, where there must be a sufficient amount of uniformly dispersed particles entrained in the fluid to provide an accurate input to the correlation analysis. This is also related to the image density, or the average number of scatterers in an interrogation cell [4]. All of these seeding requirements have led to the use of solid seed materials such as Titanium Dioxide (TiO_2), Aluminum Oxide (Al_2O_3), Polystyrene and Magnesium Oxide (MgO). Liquid seed materials have included oil-based particles such as Di-Ethyl-Hexyl-Sebacat (DEHS), glycol, and water.

1.1 Motivation

The correct choice of seed particles is critical for PIV and depends on the application. For wind tunnels, the most common seeding materials are TiO_2, DEHS and water. Though generally considered good seeding materials based on size, composition, density, shape and concentration, these materials often leave a residue or corrode tunnel components. Solid seed materials like TiO_2 can sometimes clog filters, damage tunnel compressor blades, flow dryers, flow straighteners and flow turning elements if introduced into high-speed gas flows. A known fact about DEHS is that it requires extensive clean-up of the tunnel walls and test section after PIV experiments are conducted in closed-circuit wind tunnels. In one extreme case, DEHS caused damage to one of the coolers used in the transonic wind tunnel owned by the French aerospace research center ONERA [6]. In addition to these concerns, many tunnel conditions are run close to the auto-ignition temperatures of certain seed particles like olive oil and Al_2O_3, which have the potential for starting a fire. The consequences of using such seed materials are obvious: safety concerns for personnel and risk of damage to tunnel components.

As a viable alternative to these traditional seeding materials, this thesis investigates the use of solid carbon dioxide (CO_2), or dry ice, due to its physical properties–it transforms into a solid at temperatures less than -78.5 °C at atmospheric pressure before quickly sublimating back to its gaseous form above this temperature. CO_2 can easily be stored as a liquid in a high-pressure tank and injected as solid particles, which can be used as seed material for the test section of a wind tunnel experiment. Ideally, downstream of the test section the particles would sublimate directly from a solid to a gas in the diffuser portion of the wind tunnel. This eliminates the need for any cleanup, prevents corrosion, and avoids fire hazards. Herein, dry ice is often referred to as "clean" seed. Though the non-residual properties of dry ice make it an attractive option for many closed-circuit wind

5

tunnel applications, multiple challenges exist that hinder its ability to be widely accepted as a seed material. To date, six proof-of-concept experiments have been demonstrated in three wind tunnels at the Air Force Institute of Technology (AFIT) and Air Force Research Lab (AFRL). All of the experiments were able to successfully generate discrete dry ice particles in the test section and witness sublimation in the diffuser section. However, issues with the basic seeding requirements of ideal size, shape and concentration were present in all experiments and affected the validity of the results compared to other experimental or theoretical data. The next section provides further details of the aforementioned experiments and discusses the follow-on work to be accomplished.

1.2 Research Focus

The overall goal of the current research effort is to build upon the previous research to produce dry ice tracer particles of homogeneous distribution at "medium" density (more details about this will be explained in Chapter 2) via a seeding method and to improve the spatial resolution in the test section with image processing. A desired output of this research is to produce better quality PIV vector maps consistent with other seed materials. To accomplish this, the following goals for each path are outlined below:

Seeding Method

- Continue efforts to generate homogenous, "medium-image" density, solid-phase carbon dioxide particles for wind tunnel use by conducting small-scale, particle sizing experiments with various injector designs

- Apply the knowledge gained from the particle control experiments based on previous and current research for use in a wind tunnel demonstration

Image Processing

- Improve flow tracking accuracy by using an appropriate image processing method while maintaining acceptable particle image density (recommended 10 or more particles per interrogation region or 1,000 to 10,000 vectors per image)

- Demonstrate the ability to obtain particle size measurements using a new automated imaging technique with subsequent image processing

The next chapter provides an overview of PIV and its components used for research. In addition, outlines of Particle Shadow Velocimetry (PSV) and the algorithm used for PIV + Particle Tracking Velocimetry (PTV) are given due to their relevance for the particle sizing technique and refined data processing for previous boundary layer profiles, respectively.

II. Background

The purpose of this chapter is to provide the reader with the necessary background on PIV, including its components: illumination source, imaging system and flow seeding. Velocity field generation via cross correlation methods, including the particle tracking algorithm used to refine the vector map of the boundary layer measurement in the AFRL Trisonic Gasdynamics Facility (TGF), will be discussed. Next, an overview of a similar experimental technique called Particle Shadow Velocimetry (PSV) will be summarized, since a variation on the technique was leveraged for the particle sizing analysis. Fourth, an explanation is given of the particle sizing and characterization methods used to generate the particle distribution graphs in the results section, including a thermodynamic model for comparison of theoretical particle size. Lastly, turbulent boundary layer flow theory as pertaining to the subsonic wind tunnel testing in the TGF will be examined to provide a background for the velocity profiles generated in the results section.

2.1 PIV Overview

Particle Image Velocimetry is an optical method of flow visualization in experimental fluids research. A fluid under study is seeded with small particles so that they accurately follow the fluid motion and do not alter the fluid properties or characteristics [3]. The particles are illuminated by a light source so that they appear visible when captured with a high-resolution charge-coupled device (CCD) or complementary metal-oxide-semiconductor (CMOS) camera. Using a correlation technique, the near-instantaneous velocity and other fluid properties can be calculated from the motion of the particles. Figure 2.1 shows a typical setup for single-camera PIV in a wind tunnel experiment. PIV was developed from Laser Speckle Velocimetry (LSV), where displacements of speckle patterns were measured instead of particle images [7]. LSV utilizes images where the
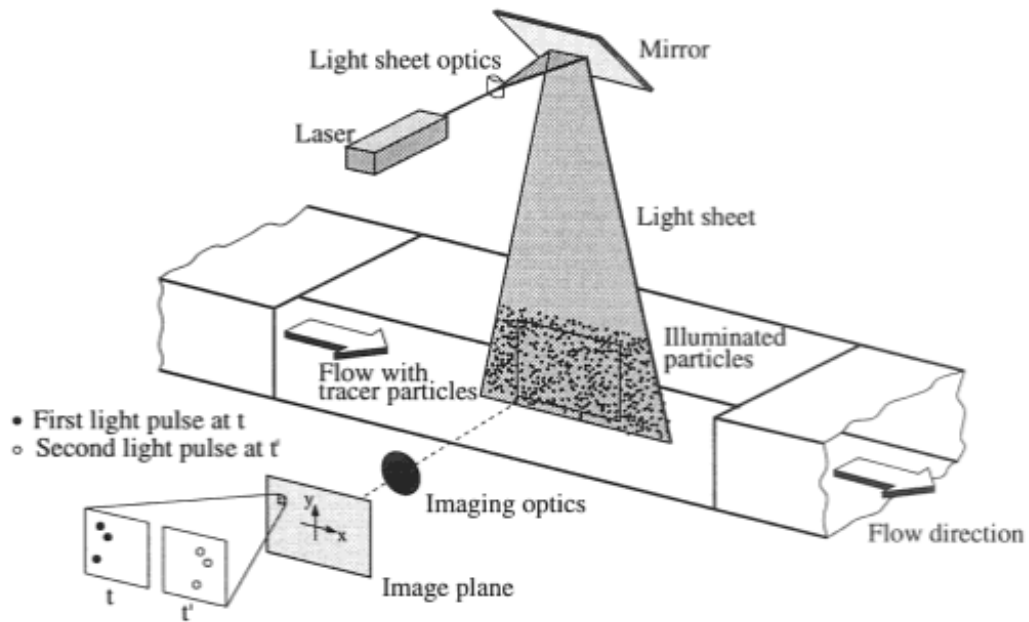
Figure 2.1: Typical PIV experimental setup in wind tunnel [2]

particle concentration is too high to observe individual particles, whereas PIV is more suited for medium particle concentration (approximately 10 particles per interrogation region). When the particle concentration is low enough to observe individual particle motion, Particle Tracking Velocimetry (PTV) is used. Figure 2.2 shows the three different types of image density. For this thesis, medium image density was required to perform the statistical PIV evaluation techniques. Where image density was too low, PTV techniques were applied and identified [2]. For a more in-depth review of PIV and its components, please refer to either the text by Adrian & Westerweel, [7] or the text by Raffel, et. al.

2.1.1 Illumination Source and Optics Requirements.

The light illuminating the particles must be short in duration, formed into a thin light sheet, and have enough power for the particles to be detected by an imaging system. The most common illumination source for PIV is the solid-state frequency-doubled
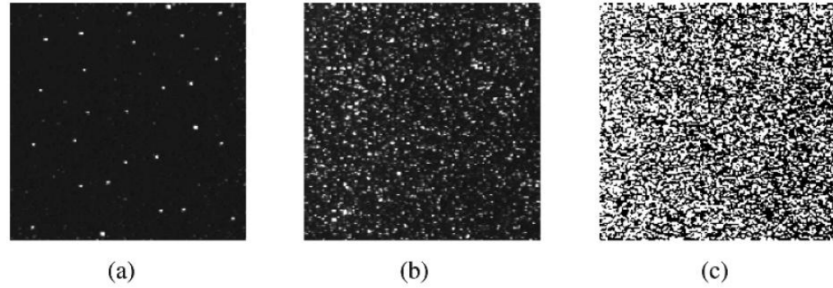
Figure 2.2: The different types of image density: a) "low-density" suitable for PTV, b) "medium density" ideal for PIV, and c) "high density" suitable for LSV [2]

neodymium-doped yttrium aluminum garnet (Nd:YAG) laser that emits visible green light with a wavelength of 532 nm. This laser is able to produce a collimated and monochromatic light beam that has a pulse duration between 5-15 ns and pulse energies ranging from 10 mJ to 1 J, ideal for a variety of flow conditions and seeding materials. Double-pulsed illumination (particles illuminated twice and observed twice between a time separation) is currently the standard for PIV because the illumination source is really two separate lasers firing independently at a required pulse separation [3]. However, as lasers become less expensive and more compact, the hope is for PIV systems to use more than two pulses [7]. Because the laser emits a focused, circular-cross section beam, cylindrical and spherical lenses are used to arrange the beam into a thin light sheet. Cylindrical lenses are used to expand the laser into a plane while spherical lenses focus the beam at a distance equal to the focal length of the cylindrical lens. The desired sheet width and uniformity can thus be controlled for each experiment. It is sometimes challenging to align the laser beam with the imaging area due to the physical constraints of a wind tunnel or other experimental setup. Therefore, reflective mirrors are often used to align the laser sheet in the proper location and orientation [3].
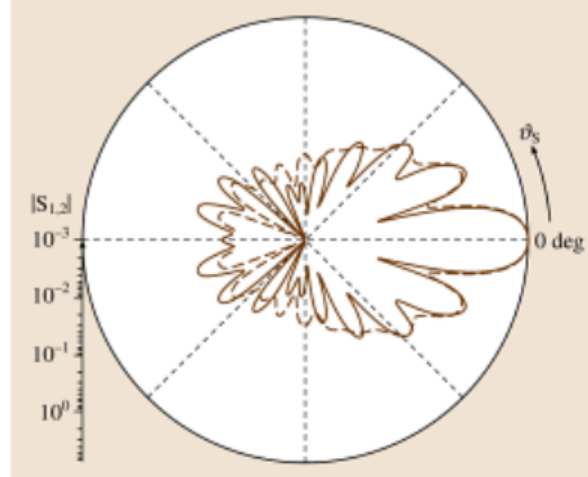
Figure 2.3: An example Mie scattering function for a water droplet in air. Most of the light is scattered forward as shown by the large intensity at 0°. [3]

Most PIV applications use particles larger than the wavelength of the illumination source due to their higher signal-to-noise ratio. These particles rely on Mie scattering, where most of the light is scattered forward and less scattered backwards and to the sides. The scattered light intensity is proportional to the number density of particles in a given volume, so a limiting factor of Mie scattering is spatial resolution [8]. A diagram of Mie scattering is shown in Figure 2.3.

2.1.2 Imaging Requirements.

In the past, PIV images were captured and stored on film. Due to the slow shutter speeds of these cameras, two images, or exposures, were captured on the same frame. A statistical method called autocorrelation was then used to determine the displacements of the particles. Unfortunately, this method led to some ambiguity in particle movement between the first and second laser pulse unless the operator had some initial information about the observed flow [9]. Today, PIV images are captured as double frame/single exposure digitally with either high-resolution CCD or high-speed CMOS cameras and then evaluated using cross-correlation.

Though many forms of PIV are conducted today, the most common PIV setup uses either one camera (simple) or two cameras (stereoscopic). In single camera PIV, the camera is positioned perpendicular to the plane of the light sheet and records a pair of single exposure images with a small time separation between. This setup was shown in Figure 2.1. In stereoscopic PIV, single exposure images are still acquired but two cameras are utilized to obtain a third out-of-plane component of velocity. There are two generic optical configurations for stereoscopic PIV: the angular displacement configuration and the translation configuration. The angular displacement configuration is most commonly used today because it allows for larger viewing angles as shown in Figure 2.4. The optical axes of the imaging lenses are each at an angle θ with respect to the normal of the light sheet plane, and the image sensors of the cameras are tilted using Schiempflug mounts so that they coincide with the image focal plane [7].
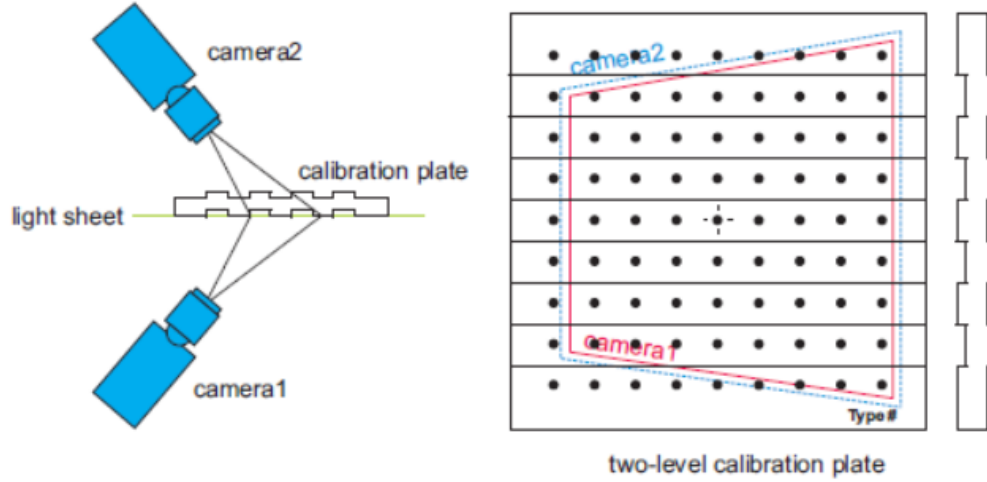
Figure 2.4: An example Forward-Forward scattering or Backward-Backward scattering stereoscopic PIV configuration. In Forward-Forward scattering, most of the light scattered forward from the particles are detected by the cameras. The opposite is true for the Backward-Backward scattering, where most of the light is scattered backwards [9]. The Backward-Backward configuration was used in the turbulent boundary layer measurement experiments.

2.1.3 Flow Seeding Requirements.

The generic requirements for flow seeding are that the particles must be sufficiently small to track the flow field but must scatter sufficient light to provide a strong signal to noise ratio for the measurement [10]. Ideally, seed materials are spherical in nature and their motion in a fluid is governed by the Stokes' number. This is defined as the ratio of the characteristic time of a particle to a characteristic time of the the the flow. Using Melling's approach for the equation of motion of a small spherical particle immersed in a fluid flow with low Reynolds number,

13

$$\frac{\pi d_p^3}{6}\rho_p \frac{\mathrm{d}\widehat{U}_p}{\mathrm{d}t} = -3\pi\mu d_p \widehat{V} + \frac{\pi d_p^3}{6}\rho_f \frac{\mathrm{d}\widehat{U}_f}{\mathrm{d}t} - \frac{1}{2}\frac{\pi d_p^3}{6}\rho_f \frac{\mathrm{d}\widehat{V}}{\mathrm{d}t} - \\ \frac{3}{2}d_p^2(\pi\mu\rho_f)^{\frac{1}{2}} \int_{t_0}^{t} \frac{\mathrm{d}\widehat{V}}{\mathrm{d}\xi}\frac{\mathrm{d}\xi}{(t-\xi)^{\frac{1}{2}}} \tag{2.1}$$

This equation is known as the Bassett Boussinesq-Oseen (BBO) equation and relates the instantaneous relative velocity $\widehat{V} = \widehat{U}_p - \widehat{U}_f$ between the particle and the fluid to the instantaneous velocities $\widehat{U}_p$ and $\widehat{U}_f$ of the particle and fluid, respectively [5]. The first term on the left side of the equation is the acceleration force according to Stokes' law. The second term on the right side of the equation is the viscous resistance. The third term is the non-inertial force due to a pressure gradient. The fourth term represents the quasi-steady viscous force, as given by potential theory. The fifth and last term is the "Basset history integral" and is the resistance caused by the unsteadiness of the flow field. For the dynamics of solid particles in gaseous flow neglecting shear effects and centrifugal forces, only the first two terms are important because $\rho_p >> \rho_f$. This greatly simplifies Equation (2.1) to:

$$\frac{\mathrm{d}\widehat{U}_p}{\widehat{U}_f} = -C(\widehat{U}_p - \widehat{U}_f) \tag{2.2}$$

where C is the characteristic frequency of the particle motion, defined in terms of the drag coefficient C_D as:

$$C = \frac{3}{4}C_D Re_p \frac{\mu}{\rho_p d_p^2} \tag{2.3}$$

where:

Re_p is the Reynolds number of the particle

μ is the dynamic viscosity of the fluid

ρ_p is the density of the particle

d_p is the particle diameter

For Stokes' resistance, $C_D = 24/Re_p$. Substituting into the above equation for C,

$$C = \frac{18\mu}{\rho_p d_p^2} \tag{2.4}$$

A single exponential decay law can be used to model the particle response to a stepwise variation in the flow velocity, which is equal to the inverse of the characteristic frequency as shown in Equation (2.5):

$$\tau_p = \frac{\rho_p d_p^2}{18\mu} \tag{2.5}$$

The Stokes' number can then be defined as:

$$St_k = \frac{\tau_p U_0}{L} \tag{2.6}$$

where U_0 is the fluid velocity well away from an obstacle (such as a wall), τ_p is the characteristic response time of the particle, and L is a characteristic length usually taken to be either the integral scale or Kolmogorov scale in turbulent flows. For the purposes of this research, L was taken to be the length of the largest eddies in the flow, or the boundary layer thickness. For Stokes' numbers much less than 1, the particles are assumed to be tracking the flow accurately. For Stokes' numbers less than 0.1, the tracing errors become less than 1% [3].

Although the particles need to be sufficiently small for good fidelity, they also need to scatter sufficient light to be visible. As described in the illumination source section above, scattering for PIV typically occurs in the Mie regime, where the particle diameter is larger than the wavelength of light. The amplitude of the function of a scattering particle depends on the particle diameter (d_p) and the wavelength of the light (λ) as shown by Equation (2.7):

15

$$x_M = \frac{\pi d_p}{\lambda} \tag{2.7}$$

This equation is known as the Mie parameter. From diagram Figure 2.3, most of the light is scattered in the forward direction, presenting a challenge for single-camera PIV with an optical axis normal to the light sheet plane since the scattering amplitude is typically very low. This is why strong illumination sources such as lasers are utilized in PIV in comparison to other experimental techniques like Laser Doppler Anemometry (LDA). The scattering cross section for particles in the Mie regime is roughly proportional to the particle surface area (d_p^2) but is also heavily dependent on the angle of the incident light, which creates a problem when trying to accurately measure particle size.

In addition to accurate flow tracking and light scattering requirements, the particles must not pose health and safety concerns, should not be corrosive or reactive and should not leave undesirable residues that require tedious maintenance concerns. These additional requirements have spurred the motivation behind this thesis and highlights the advantages of using solid-phase carbon dioxide as a seed material. A table of traditional seeding materials used in PIV is shown in Figure 2.5 [2].

Type	Material	Mean diameter in μm
Solid	Polystyrene	0.5 – 10
	Alumina Al_2O_3	0.2 – 5
	Titania TiO_2	0.1 – 5
	Glass micro-spheres	0.2 – 3
	Glass micro-balloons	30 – 100
	Granules for synthetic coatings	10 – 50
	Dioctylphathalate	1 – 10
	Smoke	< 1
Liquid	Different oils	0.5 – 10
	Di-ethyl-hexyl-sebacate (DEHS)	0.5 – 1.5
	Helium-filled soap bubbles	1000 – 3000

Figure 2.5: Traditional seeding materials used for gas flows [2]

2.2 Digital Image Processing: Mathematical Background of Interrogation Including Correlation Methods

2.2.1 Cross-correlation for PIV.

Due to the large volume of data acquired with PIV, images today are processed using a cross correlation analysis using Fast Fourier Transforms (FFTs). In cross-correlation of double frame/single exposure, each image is subdivided into interrogation regions (IRs) with an area $A_I = D_{Ixx}D_{Iy}$ in the X-Y plane of the image and each particle is described by a position vector X_i. Each interrogation window ideally contains a minimum of 10 particles, and is described as high-image-density PIV [5]. For the first image, the image intensity field can be described by the convolution product of the imaging lens $\tau(x)$ with the geometric image of the tracer particle at position x_i, or by Equation (2.8):

$$I = I(x, \Gamma) = \sum_{i=1}^{N} V_0(X_i)\tau(x - x_i) \tag{2.8}$$

and for the second image recorded at a time $t + \Delta t$:

$$I' = I'(x, \Gamma) = \sum_{i=1}^{N} V_0'(X_j + D)\tau(x - x_j - d) \tag{2.9}$$

17

where D is a constant displacement for all particles inside the interrogation volume, d represents a magnification factor and $V_0'(X)$ defines the interrogation volume during the second exposure.

Then the statistical cross-correlation function of the two interrogation regions can be written as the following FFT:

$$R_{II}(s, \Gamma, D) = \frac{1}{a_I} \sum_{i,j} V_0(X_i) V_0(X_j + D) \int_{a_I} \tau(x - x_i) \tau(x - x_j + s - d) dx \qquad (2.10)$$

When the separation vector s is equal to each displacement for each particle in the IR, the displacement-correlation peak reaches a maximum and is shown graphically in Figure 2.6. When the correlation is coverted from the frequency domain into the time domain by an inverse Fourier transform, the displacement-correlation peak and location correspond to the difference in average pixel shift and direction of window shift between the two images, respectively. The correlation peak produces only one pixel shift (corresponding to a displacement) for that particular IR. The closer all particles move with the same velocity between images 1 and 2, the higher the displacement correlation peak will be. Since the time between exposures is known, the difference in pixel shift can be multiplied by a magnification factor for displacement to calculate a velocity for that particular IR. This process, shown in Figure 2.7, is repeated for each IR until the entire image contains an instantaneous velocity vector field map.
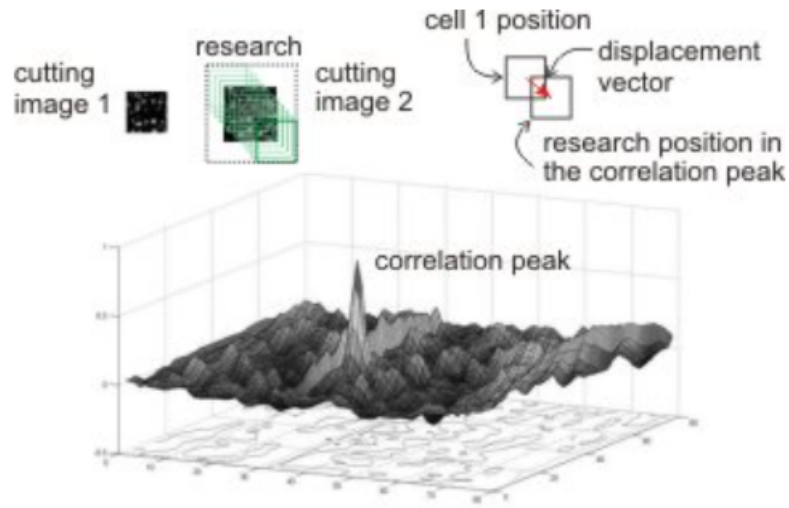
Figure 2.6: Example correlation peak for one IR in PIV [11]
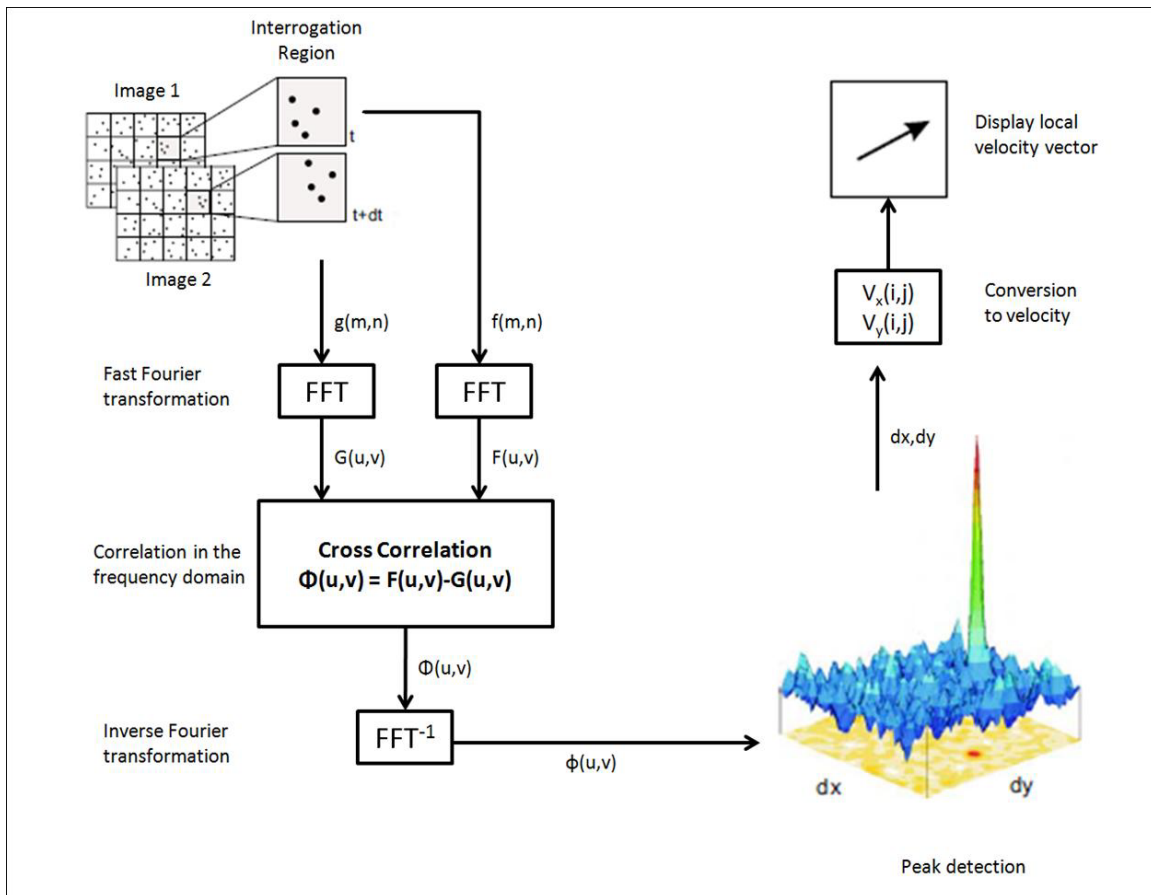
Figure 2.7: The cross-correlation method [12]

2.2.2   Iterative Multigrid PIV Image Processing for Particle Tracking Velocimetry.

As described in the PIV overview, a particle tracking velocimetry (PTV) algorithm may be used for low density seeding. Also known as "super-resolution" PIV, many different methods exist to improve spatial sampling. This research uses a hybrid PIV+PTV method that uses an iterative multigrid approach, also referred to as the Individual Particle Correlation (IPC) method. The algorithm starts with a standard PIV cross correlation evaluation to determine a velocity vector field. Next, the location of the particle with the highest intensity is determined and an interrogation window is centered around the particle in the first image. In the second image, an iterative interpolation is performed based on the displacement results from the PIV to center a window on the same particle. Correlation is performed on a single particle to determine the exact pixel shift of the particle. As with PIV, the pixel shift is converted into a displacement based on a scale factor and divided by the time between the two images to obtain a velocity vector. This time, however, a velocity vector is generated for an individual particle as opposed to a particle ensemble. This process is repeated for every single particle in the image until a vector map of the particles is created [13]. The PIV+PTV method is shown in Figure 2.8.

2.3   Particle Shadow Velocimetry (PSV) Overview

Like Particle Image Velocimetry, Particle Shadow Velocimetry (PSV) is an optical method of flow visualization that is capable of providing accurate and resolved velocity fields in a variety of applications. Particles are still used to seed the flow, however, a backlight is used to create shadows of the particles rather than reflections from scattering with a laser. This allows particle shadow velocimetry to use significantly less illumination power than particle image velocimetry. A schematic of an experiment using PSV is shown in Figure 2.9. Although PSV was not performed directly for this research, the same technique was used to capture single images for particle sizing information. The

20
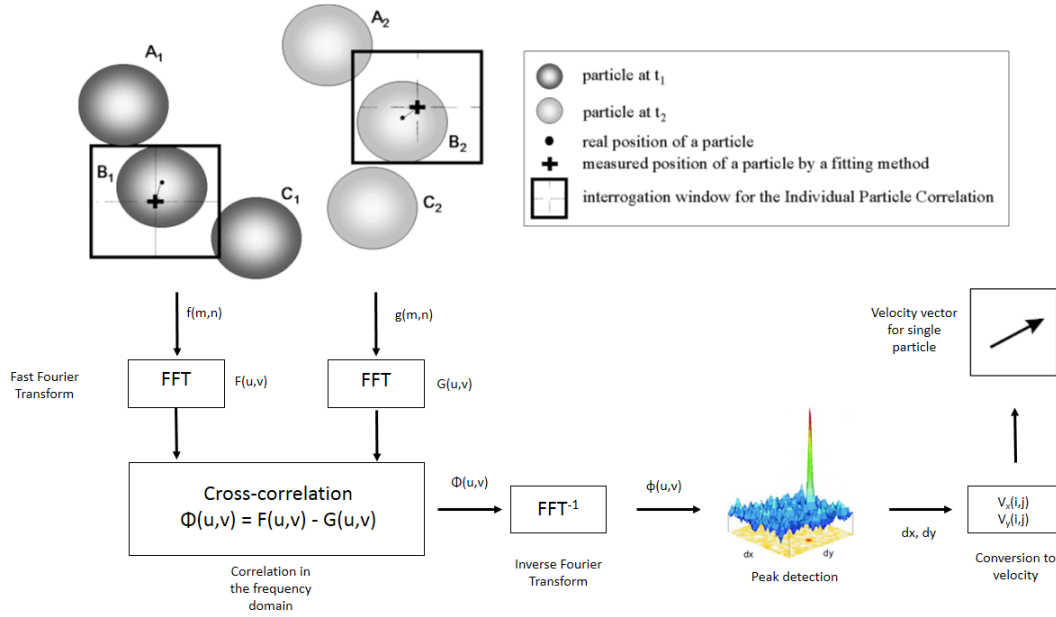
Figure 2.8: The hybrid PIV+PTV (IPC) method [13]

components of PSV are discussed in the next few subsections, such as illumination source, imaging requirements, seeding requirements and correlation methods. Most of these requirements are the same as for PIV, however, noted differences are explained in further detail. For a more in-depth review of PSV, please reference the work by Estevadeordal and Goss in [14] and [15].
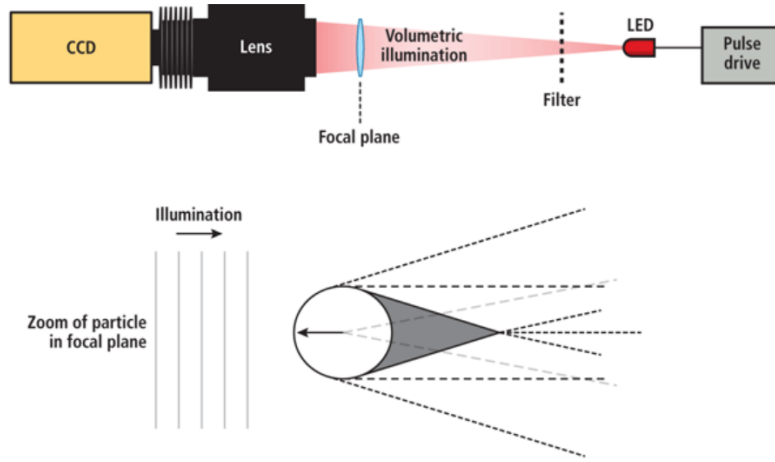
Figure 2.9: Single-camera particle shadow velocimetry experimental setup and demonstration of particle illumination [14]

2.3.1 *Illumination Source and Optics Requirements.*

As described above, PSV does not require high-powered illumination sources to light seeding particles. Rather, using a Light Emitting Diode (LED) pulsed at nanosecond durations and at high repetition rates, direct, in-line shadows of the particles are created against a bright background. Many LEDs are capable of producing monochromatic light and in different colors. Because the technique does not use scattering, fluorescence, Doppler, etc., but uses a zero-degree-deviation direct-illumination setup, accurate diameters of the particles can be obtained from the geometric shadows. The diameter of each particle is influenced only by the intensity of the incident light [14].

In Mie scattering, most of the light is scattered forward and less scattered backwards and to the sides. Forward scattering is not an issue in PSV, because the camera optics would just perceive a brighter background. Obviously, this depends upon the particle size but shadow effects dominate the image. Having a narrow depth of field is also favorable
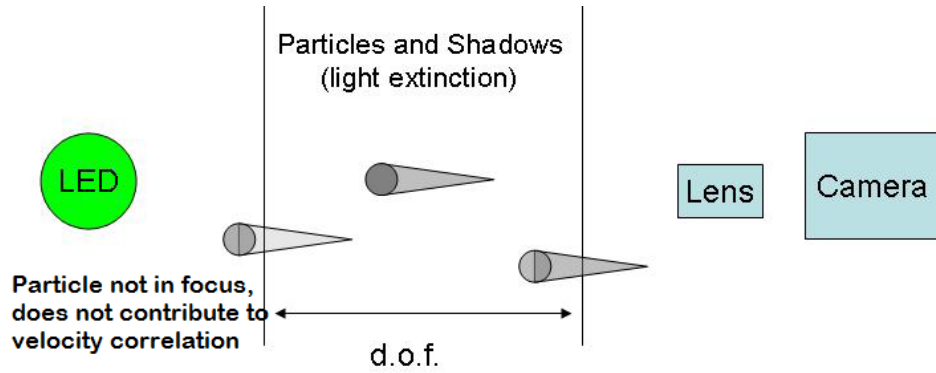
Figure 2.10: Contribution of particle shadows to image is restricted to focal plane, minimizing the contribution to the final velocity calculation [14]

for PSV, since particle shadows are observed only when they are in focus and decrease in intensity as they become out of focus. This concept is demonstrated by Figure 2.10 [14].

The imaging requirements for PSV are identical to PIV, where either a high-resolution CCD camera or high-speed CMOS camera may be used to capture the motion of the particles. Most PSV applications utilize the one camera setup. Nevertheless, stereoscopic PSV has been demonstrated by Estevadoral et. al in Reference [16].

The flow seeding requirements for PSV are identical to PIV, with the exception that the particles must scatter enough light to establish a strong signal-to-noise ratio. Rather, signal-to-noise is increased through filtering, brightness and seeding density [14].

PSV images are processed in the same manner as PIV images, using cross-correlation techniques based on the changing intensities of an image. The dark particles against a light background can be inverted to produce images appropriate for the cross-correlation analysis. The accuracy of the correlation peak finding has not been quantified, but does not seem to have a substantial effect on the velocimetry results. In PIV, the particle intensities have a Gaussian shape distribution. The particle shape distribution for PSV has not yet

23

been determined, although it appears to be influenced by the background light intensity [14].

2.4 Particle Characterization & Size Analysis

2.4.1 Particle Diameter Analysis.

The core of the current research is the ability to influence solid carbon dioxide size, specifically particle diameter. It is important to accurately characterize the particle size of the solid carbon dioxide particles because they are not perfect spheres like other traditional seed materials. Because the particles present in the shadow imaging are 2-D slices of illuminated volume measurements, it can be convenient to describe the particle size using the concept of a surface area-equivalent diameter. This is defined as the diameter of a circle with the equivalent projected area [17] as an irregular particle, or:

$$d_p = \sqrt{\frac{4A}{\pi}} \tag{2.11}$$

The average particle diameter is simply then the sum of each individual area-equivalent diameter divided by the number of particles in an image. In previous particle sizing experiments, the Sauter mean diameter, D_{32}, was used to determine the average particle diameter. For an in-depth discussion of the previous particle sizing technique using the Malvern Spraytec to obtain D_{32}, please see reference [18]. The Sauter mean diameter is defined as:

$$D_{32} = \frac{\sum_{i=1}^{N} n_i D_i^3}{\sum_{i=1}^{N} n_i D_i^2} \tag{2.12}$$

where:

n is the number of particles

D_i is the diameter of a particle

It is calculated by summing the cube of the area-equivalent diameters and then dividing by the sum of the area-equivalent diameters squared [19]. This value was used as a comparison between the particle sizing data obtained for this research and the particle sizing data in previous research.

2.4.2 *A Theoretical Model for the Sublimation Rate of CO_2 Particles.*

Predicting solid CO_2 particle size can be as important as determining solid CO_2 particle size, for example, in the test section of a wind tunnel. Because solid CO_2 particles undergo sublimation as they are expelled into an environment with a large temperature and pressure gradient (details of this exact process are discussed in Chapter 3), a particle sublimation model is necessary to compute an initial particle size distribution. If this initial particle size distribution can be controlled so that all the particles are roughly the same diameter, ideal particles for PIV (Stokes' number less than 1) can be achieved as the particles sublimate downstream. A theoretical model for the sublimation of fixed, cylindrical dry ice pellets in a moving, saturated (cloudy airstream) can be applied from Reference [20] to calculate a sublimation rate of the solid CO_2 particles. This model assumes that temperature effects comprise the greatest influence on particle size. This assumption is valid for this research, however, there are some significant differences between the experimental conditions in Reference [20] and the current research that are important. The first difference was that the sublimation of a large, cylindrical CO_2 pellet was used to derive the theoretical model as opposed to smaller, circular-shaped CO_2 particles. The second difference was that a moving airstream was passed over a stationary cylindrical pellet. This is in contrast to PIV, where the particles are presumed to follow the flow. Nevertheless, the equation can still be used to approximate the "worst case" sublimation rate for spherical particles using a heat flux balance equation:

$$\frac{dD}{dt} = -\frac{2k_a Nu}{\rho_c L_{sd} D}[(T_s - T_a) - (\frac{Pr}{Sc})^{0.63}\frac{\epsilon L_s w}{P c_p}e_a(T_a)] \tag{2.13}$$

The second term in the brackets is more important to take into account in warm environments and high humidity; it is almost negligible for a cold environment with low humidity. Then, the equation can be simplified to:

$$\frac{dD}{dt} = -\frac{2k_a Nu}{\rho_c L_{sd} D}[(T_s - T_a)]$$

(2.14)

where:

k_a is the thermal conductivity of air

Nu is the Nusselt number

ρ_c is the density of the particle

L_{sd} is the specific latent heat of sublimation of dry ice

D is the initial particle diameter

T_s is the temperature of the particle

T_a is the temperature of the air

For a stationary sphere in turbulent flow, the Nusselt number can be written as:

$$Nu = 2 + 0.6 Re_p^{1/2} Pr^{1/3}$$

(2.15)

where:

Re_p is the Reynolds number of the particle

Pr is the Prandtl number

These equations were used to calculate sublimation rates for the wind tunnel experiments in Chapter 4. The values for each of these parameters are listed in Table 4.7. For the full derivation of the above equations assuming a cylindrical CO_2 shape, please reference the article by Kochtubajda et. al [20].

2.5 Turbulent Boundary Layer Flow Theory

The velocity profile of a turbulent boundary layer varies depending on the type of boundary condition, whether it is flow in a channel, a pipe or over a smooth flat plate. Nevertheless, the velocity profile near the boundary will be similar for all cases but will differ in the free stream. The case studied in this research is the circumstance when a turbulent boundary layer is formed over a smooth, flat plate, such as a wind tunnel window. If there is no pressure gradient, and the fluid is considered to be Newtonian subject to viscous effects, the fluid must satisfy the no-slip condition at the wall [21]. The velocity of the fluid increases with perpendicular distance from the wall until it reaches the freestream velocity. The boundary layer thickness is defined as the distance from the wall to the point at which the flow velocity has reached 99% of the freestream velocity, or δ_{99}.

For a turbulent boundary layer, the boundary layer thickness is given by Equation (2.16):

$$\delta = \frac{0.37x}{Re_x^{1/5}} \tag{2.16}$$

where x is streamwise distance along the flat plate and Re_x is the Reynolds number given by Equation (2.17):

$$Re_x = \frac{\rho U_0 x}{\mu_x} \tag{2.17}$$

The velocity profile of a turbulent boundary layer over a wall can be subdivided into two regions: the inner layer, where viscous stress dominates and the outer layer, where the Reynolds shear stress dictates the shape of the profile. Near the wall is the viscous

27

Region	Location	Defining property
Inner layer	$y/\delta < 0.1$	$\langle U \rangle$ determined by u_τ and y^+, independent of U_0 and δ
Viscous wall region	$y^+ < 50$	The viscous contribution to the shear stress is significant
Viscous sublayer	$y^+ < 5$	The Reynolds shear stress is negligible compared with the viscous stress
Outer layer	$y^+ > 50$	Direct effects of viscosity on $\langle U \rangle$ are negligible
Overlap region	$y^+ > 50, y/\delta < 0.1$	Region of overlap between inner and outer layers (at large Reynolds numbers)
Log-law region	$y^+ > 30, y/\delta < 0.3$	The log-law holds
Buffer layer	$5 < y^+ < 30$	The region between the viscous sublayer and the log-law region

Figure 2.11: Wall regions, layers and their defining properties [22]

sublayer, where viscous stress is a maximum. Further out from the wall, the velocity profile is governed by the log-law, where turbulence has more of an effect. Between the viscous sublayer and the log-law region is the buffer layer, which is the transition between viscosity-dominated and tubulence-dominated parts of the flow [22]. Figure 2.11 shows the wall regions, layers and their defining properties. For this research, only the log-law region was considered for a theoretical boundary layer comparison due to the region of interest where the log-law holds ($y^+ > 30, y/\delta < 0.3$). The turbulent boundary layer was also assumed incompressible for purposes of simplicity and because the Mach number was not in the high subsonic regime (Mach 0.5). Equation (2.18) is considered the log law of the inner layer and can be written as:

$$u^+ = \frac{1}{\kappa} \ln y^+ + B \tag{2.18}$$

where

$$u^+ = \frac{<U>}{u_\tau} \tag{2.19}$$

$$y^+ = \frac{y}{\delta_\nu} \tag{2.20}$$

$$\delta_\nu = \frac{\nu}{u_\tau} \tag{2.21}$$

and

$$u_\tau = \sqrt{\frac{\tau_w}{\rho}} \tag{2.22}$$

Equation (2.23) is the log law of the outer layer and can be written as:

$$\frac{U_0 - <U>}{u_\tau} = -\frac{1}{\kappa} \ln \frac{y}{\delta} + B_1 \tag{2.23}$$

The variables above are defined as:

y is the height above the wall

δ is the boundary layer thickness as shown in Equation (2.16).

u_τ is the friction velocity

ν is the kinematic viscosity of the fluid

τ_w is the wall shear stress

ρ is the density of the fluid

$<U>$ is the local mean velocity of the fluid

κ is the von Karman constant, and is generally given as $\kappa = 0.41$

29

B is a constant, and is generally given as $B = 5.2$

B_1 is a constant, and usually ranges from $B_1 = 0$ to 0.7 depending on the characteristics of the flow

For a compressible, turbulent boundary layer the exact solution for the displacement thickness is given by:

$$\delta^* = \int_0^\infty \left(1 - \frac{\rho(y)u(y)}{\rho_e U_e}\right) dy \qquad (2.24)$$

For a compressible turbulent boundary layer the exact solution for the momentum thickness is given by:

$$\theta = \int_0^\infty \frac{\rho(y)u(y)}{\rho_e U_e}\left(1 - \frac{u(y)}{U_e}\right) dy \qquad (2.25)$$

The shape factor, which determines the nature of a flow, is the ratio of the displacement thickness to the momentum thickness and is given by Equation (2.26).

$$H = \frac{\delta^*}{\theta} \qquad (2.26)$$

For further background information for the turbulent boundary layer on a flat plate, please reference the text by White in Reference [21], pgs. 433-434 and the text by Pope in Reference [22], pgs. 273-278.

2.6 Previous Research Using Dry Ice

Research using dry ice as a seeding material has been conducted at AFIT since 2006, where initial work was done by DeLapp [23] in cooperation with AFRL and Innovative Scientific Solutions, Inc. (ISSI). DeLapp demonstrated the ability to produce discrete dry ice particles using a commercially available system called the Sno-Gun II, shown in

Figure 2.12. The Sno-Gun II is marketed as a device for cleaning electronic and optical equipment without leaving a residue. Nozzle diameter size and shape were varied to observe the size and agglomeration effects of the CO_2 particles. The Sno-Gun II hardware was then adapted for use in AFIT's 0.0635 m x 0.0635 m closed-circuit supersonic wind tunnel to determine if velocity maps around a 10-degree half angle cone could be generated at Mach 2.9. The absence of discrete dry ice particles in the test section prevented accurate velocity measurements for this case, but demonstrated the feasibility of CO_2 as a seed material.

Figure 2.12: Sno-Gun II system with various nozzles and metering tubes [23]

The following year, McNiel [24] attempted to increase dry ice particle size by incorporating two different-style injectors in the same closed-circuit, 0.0635 m x 0.0635 m supersonic wind tunnel. He did not achieve much success with the first injector: a capped, multi-port shroud tube (shown in Figure 2.13) since it only produced "cloud-like" particles in the test section similar to the particles generated by DeLapp. Better results were generated when an open-ended feed and shroud tube configuration (shown in Figure 2.14)

was used to inject CO_2 in the tunnel's nozzle sidewall. Though visibly discrete particles were created using the second injector configuration, the cloud-like particles were still present in the images. This reduced the validity of the velocity data results after post-processing and necessitated the need for greater particle uniformity.
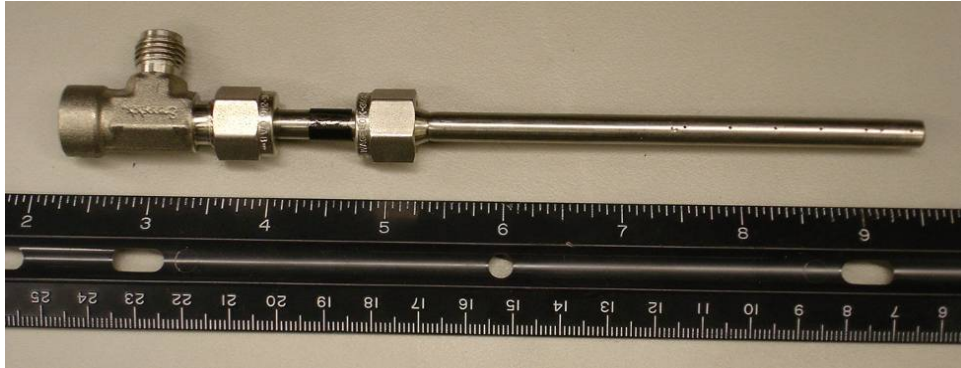
Figure 2.13: Closed multi-port shroud injector with six ejection ports [24]

Figure 2.14: Open-ended feed tube/shroud combination injector [24]

Greene [25] further built upon the work of DeLapp and McNiel in 2008 by exploring different length and diameter sizes of injectors. Research was first conducted using a particle size analyzer at atmospheric conditions to understand the effects of different injectors, the addition of purge air and shroud tube insulation on particle size. He

discovered that increasing the length of the shroud tube, increasing the inner diameter of the shroud tube, decreasing the inner diameter of the feed tube and insulating the shroud tube each increased dry ice particle size. Sizing data were taken using a Malvern Spraytec particle size analyzer, which provides a single-point measurement of particle size distribution based on particle volume. For further details on the Malvern Spraytec particle size analyzer, please refer to Reference [25]. Purging the dry ice particles with dry air prior to entering the test region reduced particle size but reduced concentration levels. Greene was able to successfully complete particle relaxation time measurements across an oblique shock wave in the 0.0635 m x 0.0635 m supersonic wind tunnel and compare them with the results of Scarano et al. (2003) for TiO_2 particles. When attempting to scale the dry ice technique to AFIT's larger 0.154 m x 0.165 m supersonic wind tunnel, particle concentration significantly decreased in the test section due to a longer distance between the injection site and test section and an increase in the air mass flow rate of the tunnel. These two factors prevented quality vector maps from being generated, but showed that an increase in particle size and concentration was needed.

Research by Love [18] in 2010 began similarly to that of Greene's where he conducted small-scale particle sizing and concentration experiments with different size feed tubes and shroud tubes. In addition, Love investigated the use of a static mixer within a shroud tube as shown in Figure 2.15. He deduced that using the static mixer reduced mean particle diameter by one third as opposed to using a simple feed/shroud tube system alone. Love also studied the response time of the dry ice particles across an oblique shock wave in the AFIT 0.154 m x 0.165 m supersonic wind tunnel using three injection points to increase the amount of CO_2 concentration. He was able to produce several suitable vector maps that compared favorably with Schlieren images taken of the same setup. For the first time, Love was able to inject dry ice particles into the stilling chamber at AFRL's Trisonic Gas-Dynamics Facility (TGF), which has a 0.61 m x 0.61 m test cross-section.

Freestream velocities and turbulence levels were successfully measured at three subsonic speeds and four stagnation pressures using a simple 1.727 mm ID feed tube and 10.16 mm ID shroud tube injecting into the stilling chamber of the wind tunnel. PIV results matched predicted velocity values within a few percent and freestream turbulence was within 1-2% error. These tests showed that dry ice seeding could be successfully implemented in a full scale wind tunnel test, but that more work needed to be accomplished to increase particle concentration in localized regions of the flow, such as boundary layer flow.

Figure 2.15: Kenics static mixer used in simple shroud tube [18]

Further work by Wolfe in 2012 [12] aimed at measuring freestream velocities, turbulent boundary layers and turbulence intensities using dry ice PIV in the TGF. Experiments were conducted at three subsonic speeds and stagnation pressures that ranged from 23.94 to 115 kilopascals (kPa). Wolfe was able to produce good particle concentration along the test section window using a dry ice distribution manifold shown in Figure 2.16. Eight feed/shroud tube combinations of the same length and ID were used to inject dry ice into the stilling chamber of the TGF. The connection points for the shroud tubes were designed so that they could be replaced with smaller or larger ID shroud tubes to

Figure 2.16: CO_2 distribution manifold installed in the TGF [12]

characterize particle size and concentration. Wolfe discovered a direct relationship between stagnation pressure and particle size that was common among the various shroud tube sizes: as stagnation pressure increased, particle size increased. While this was acceptable in terms of particle concentration for PIV, it raised doubt as to whether the larger particles were actually following the flow field. Consequently, the boundary layer and turbulence intensity measurements match theoretical trends, but the accuracy of the results remained uncertain. Part of the current work focuses on refining some of the data post-processing methods used to generate the boundary layer profiles to investigate whether more accurate results can be achieved and are consistent with other experimental values. In the next chapter, the methodology for particle size measurements and data processing of the turbulent boundary layer will be discussed.

III. Methodology

This chapter provides an explanation of the improved data processing methods used to re-process the PIV turbulent boundary layer images obtained in 2011. A setup of experimental equipment and test procedures used for the particle size analysis tests conducted at AFIT and AFRL is given, followed by a discussion of the image-based particle size analysis technique. The last section describes the image processing and sizing analysis methods used to generate the particle size distributions and statistics in the results section, which are compared with previous research.

3.1 Refined Data Processing for PIV Turbulent Boundary Layer Profiles

This section encompasses the methodology used in the current research to generate the new boundary layer profiles presented in Chapter 4. It does not discuss the test equipment and procedures used to gather the PIV data. For further information regarding that particular aspect of research, please refer to the methodology section in Reference [12]. The differences between the data processing methods are listed in Table 4.1. A refined PIV processing method was performed on the existing PIV turbulent boundary layer data. A PIV + PTV method was used for further refinement of the velocity vector maps generated from the re-processed PIV method, however, only single-camera images (camera 1) were processed due to limitations within the software. The purpose of the refined data processing was to improve data processing through careful selection of image processing/image calibration techniques in comparison with pitot probe data and theoretical incompressible turbulent boundary layer curves. Only the Mach 0.5, 47.88 kPa (1000 psf) case was considered for evaluation because of the high image count (10,000 image pairs), enabling a higher confidence in flow tracking accuracy. All images were processed using DaVis® 8.1 in four steps: preprocessing, stereo cross-correlation, post-processing and vector statistics

(leading to a velocity vector map). The most significant difference between the original PIV processing method and the refined PIV processing method was the implementation of a re-calibration method called "self calibration." The self calibration feature re-adjusted the coordinate system and the camera calibration with respect to the light sheet, which can be a major source of error in stereoscopic PIV images. The major differences between the original PIV processing method and PIV + PTV processing method were that cross-correlation was performed on single particles as opposed to groups of particles in an interrogation window. The following sections describe the methodologies of the PIV and PIV + PTV processes in further detail.

3.1.0.1 Pre-processing.

In the refined PIV processing, a non-linear noise reduction filter called "subtract a sliding average" was applied before a background subtraction was applied. A scale length of 12 pixels was used to correspond with the observed particle diameter range in the images. A "subtract a sliding background" filter was applied similarly to the pre-processing methodology used in Reference [12]. The pixel scale length was changed to 12 pixels to correspond with the subtract a sliding average noise filter. In the PIV + PTV processing, the subtract a sliding background filter was applied with a scale length of 8 pixels because it appeared to produce the best results.

3.1.0.2 Self-calibration.

This feature recalculates a coordinate system and the camera calibration of a stereoscopic PIV setup so that the plane z=0 mm (calibration plate) will be adjusted exactly in the middle of the laser light sheet. In stereoscopic PIV, the images from camera 1 and camera 2 are dewarped using the original calibration to produce corrected images as if the image had been taken with a single camera viewing perpendicular to the light sheet. When dewarping is completed for each camera, there are typically errors associated with the exact location of the particles due to misalignment of the calibration plate position

37
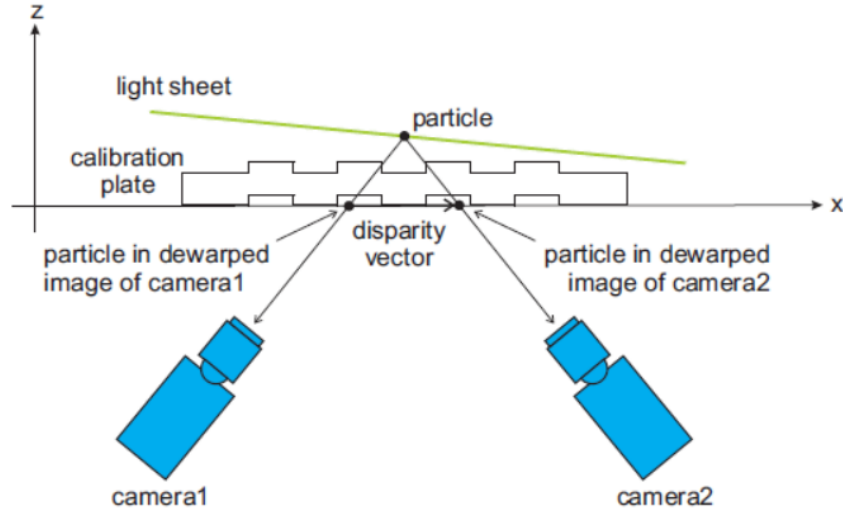
Figure 3.1: A stereo PIV setup where the laser light sheet is misaligned with the calibration plate [9]

and light sheet position. This produces a disparity vector as shown in Figure 3.1. The self-calibration feature in DaVis® was applied to correct this error in the re-processed data of 10,000 images and was based on a disparity map calculation. This is essentially a correlation map corresponding to the location of the correlation peaks from interrogation regions in the dewarped images of camera 1 and camera 2. After successful re-calibration, the disparity vector shown in Figure 3.1 should ideally be zero [9].

Self-calibration was not applied for the PIV + PTV method because processing was performed on a single camera only.

3.1.0.3 Stereo cross-correlation.

Prior to cross-correlation, a mask was applied to camera 1 and camera 2 for the refined PIV processing method to include only the image data that represented the tunnel window and boundary layer leading up to the freestream. All other data (reflections off the tunnel

window) were disabled. The image pairs from Camera 1 were only used in the PIV + PTV processing, and approximately two-thirds of the image field of view were masked (only included boundary layer and free stream) due to processing time constraints.

For the refined PIV processing, stereo cross-correlation was performed on the images using initial elliptical IR regions of 512 x 128 pixels (4:1) with 50% overlap followed by three multi-pass iterations using 256 x 64 pixel elliptical (4:1) regions with 50% overlap. The high-accuracy mode for final passes was selected. The stereo correlation method uses a standard FFT correlation algorithm but performs the correlation on corrected images based on the calibration of cameras 1 and 2. For the PIV + PTV processing, PIV results were generated first using single-camera cross-correlation. The same parameters that were used in the refined PIV processing method were also used for the PIV + PTV method. For the PTV step, a particle size range of 2 to 20 pixels with an intensity threshold of 2 counts was used with a correlation window size of 16 pixels. The allowed vector range relative to the reference was 10 pixels.

The refined PIV and PIV + PTV methods both used multi-pass postprocessing with two iterations: A a median filter was used to "strongly remove & iteratively" replace vectors if they differed by more than two times the RMS of neighboring vectors and reinsert if they differed by less than three times the RMS of neighboring vectors. A 3x3 smoothing filter was also selected by default to reduce noise.

3.1.0.4 *Post-processing.*

Vector post-processing for the refined PIV method was similar to multi-pass postprocessing with the exception of an additional peak validation (Q) of 1.3. The peak validation measures the relative height of the two tallest correlation peaks in an interrogation region and results in a valid vector if the height ratio of the tallest peak to the second tallest peak is 1.3 or greater. The rule of thumb is that the higher the height ratio,

the more likely the signal corresponding to the true velocity of the region is accurate. The median filter and smoothing operations were re-performed in the vector post processing. Vector post-processing for the PIV + PTV method did not include peak validation, however, a denoising polynomial 1st-order fit with six vectors used for smoothing was applied. A polynomial fit (2nd-order) using three neighboring vectors was used to convert the vectors to a grid. The new grid size setting was 16 pixels, where output was disabled if a vector was not found within a distance of 16 pixels.

3.1.0.5   Vector statistics.

After the cross-correlation and post-processing steps were performed, a 2-D velocity vector map (averaged over the entire image set) and a RMS of the velocities were generated with a minimum threshold of 1000 source velocities for the refined PIV processing method, and 200 source vectors for the PIV + PTV processing method. Besides outputting an average velocity magnitude for the entire image set, the streamwise velocity (V_x) and normal velocity (V_y) could be acquired from the calculations.

3.2   Particle Generation System

The dry ice seeding particles were generated from a high-pressure container consisting of liquid carbon dioxide ($CO_{2(l)}$) and gaseous carbon dioxide ($CO_{2(g)}$) shown in Figure 3.2. The container is 180 liters in volume and is pressurized to approximately 2379 kPa (345 psi). The production of dry ice particles occured when a manual gate valve was opened, drawing $CO_{2(l)}$ from a siphon tube in the lower region of the tank. The $CO_{2(l)}$ then flowed through an insulated, flexible stainless steel hose, before entering a series of stainless steel or brass Swagelok® fittings. Next, the $CO_{2(l)}$ either first flowed through a "feed tube" connected to a Washjet ® 1/8-MEG-0002 expansion nozzle with a 0.864 mm (0.034 inch) orifice before it entered a 19 mm (3/4 inch) National Pipe Thread (NPT) stainless steel "shroud tube," or flowed directly through the expansion nozzle before exiting the shroud

Figure 3.2: CO_2 dewar used for all experiments

tube. The expansion nozzle and shroud tube were the same injector system used in the turbulent boundary layer experiments in 2011. The feed tubes varied in inner diameter (ID) depending on the experiment. A picture showing the latter setup (absent the feed tube) is given in Figure 3.3. A view of the different feed tubes, as well as the expansion nozzle, reducing coupling and shroud tube is shown in Figure 3.4.
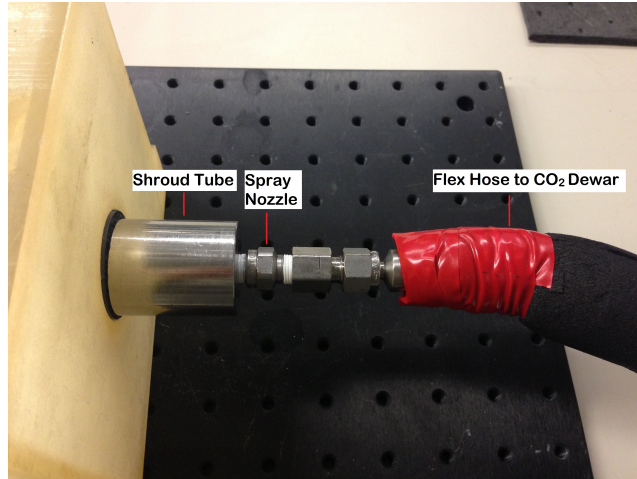
Figure 3.3: A view of the downstream setup of the particle generation system (absent feed tube)
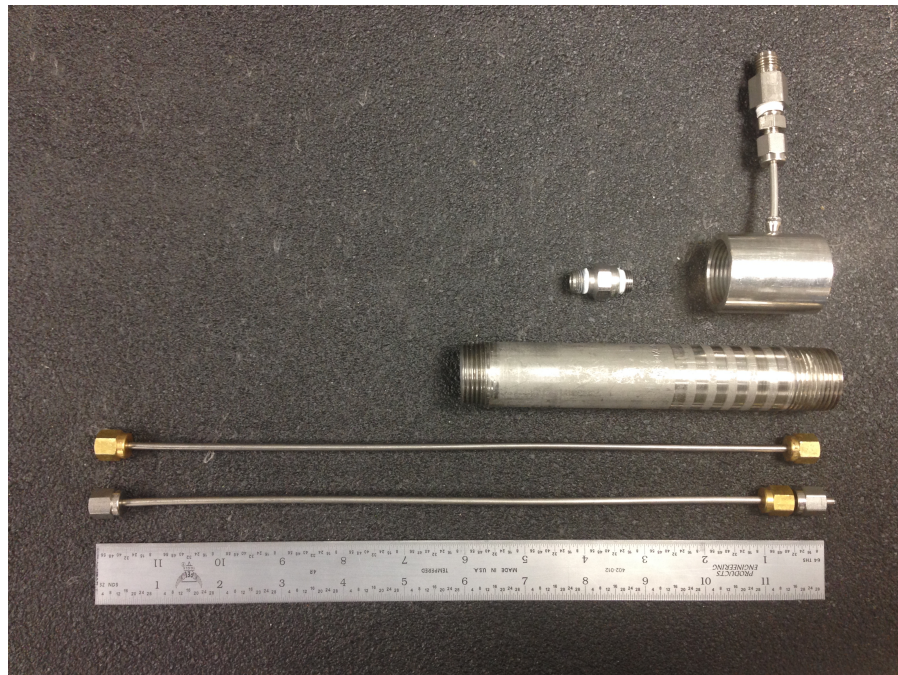
Figure 3.4: Reducing coupling, 1/8-MEG-0002 expansion nozzle, 19 mm (3/4 inch) NPT shroud tube, 0.76 mm (0.03 inch) ID feed tube and 1.4 mm (0.055 inch) ID feed tube (From top right to bottom)

The formation of solid CO_2 particles takes place between the nozzle/shroud tube interface, where the liquid is allowed to rapidly expand from the smaller diameter of the nozzle into the larger diameter shroud tube. This expansion process (shown in Figure 3.5) significantly decreases the temperature of the $CO_{2(l)}$, causing it to form a mixture of $CO_{2(g)}$ and solid CO_2. This generation process is similar to the two-step expansion process used by the BOC Group in 1989 [10]. After the second expansion, the $CO_{2(l)}$ freezes and agglomerates in the shroud tube, producing particles that are larger than if the liquid were expanded through a single nozzle. As the solid CO_2 particles travel downstream of the shroud tube exit, they begin to warm up at ambient temperature and pressure until they reach their sublimation point. This transformation of CO_2 from liquid to solid and then gaseous CO_2 is illustrated by Figure 3.6. A schematic of the expansion nozzle is shown in Figure 3.7.
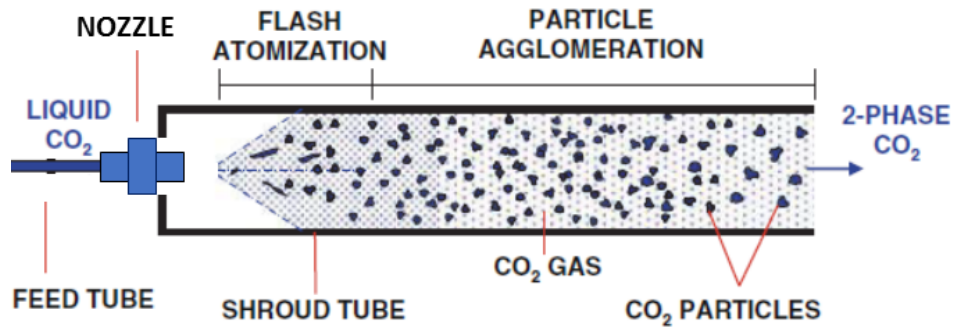
Figure 3.5: Schematic of the system used to generate CO_2 particles [10]
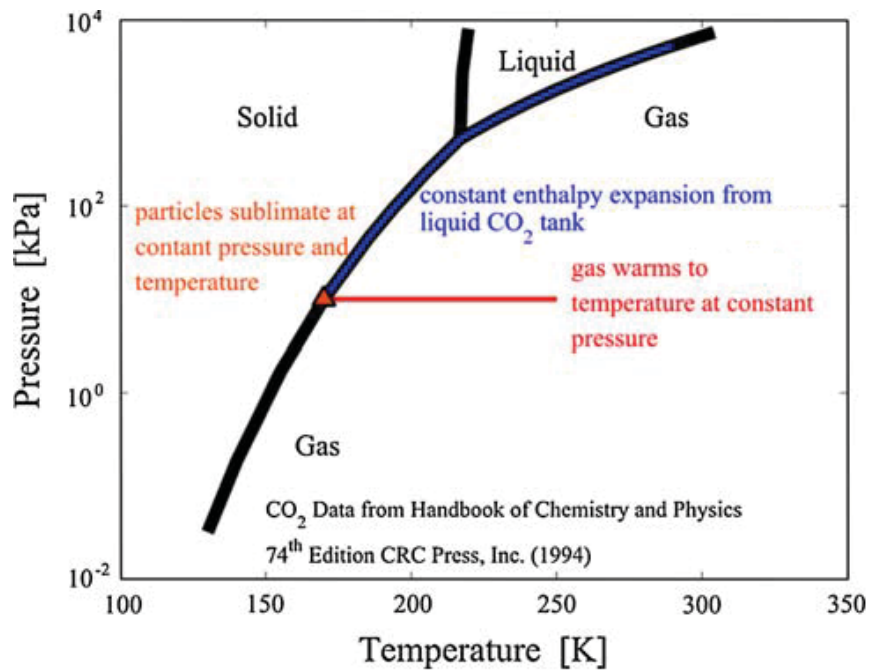
Figure 3.6: Phase diagram showing the life cycle of the CO_2 particles during the experiments [10]

CONNECTION TO
COUPLING
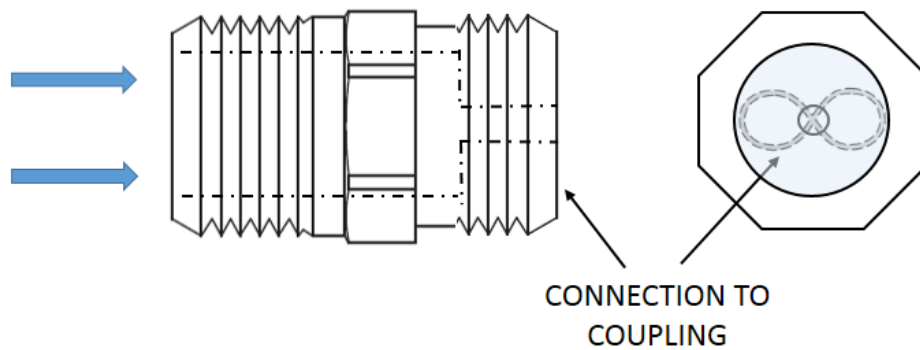
Figure 3.7: Schematic of the expansion nozzle

The same expansion interface (expansion nozzle and shroud tube) were used for all experiments, and two different sizes of feed tube were used in the particle size analysis experiments. Both feed tubes had a 3.18 mm (1/8 inch) outer diameter (OD). The feed tube IDs were 1.4 mm (0.055 inches) and 0.76 mm (0.03 inches) with lengths of 0.31 m (12.1 inch) and 0.29 m (11.63 inch), respectively.

3.3 Particle Size Analysis (PSA) via Particle Shadow Imaging

3.3.1 PSA at AFIT.

Particle size analysis experiments at AFIT were conducted in a testing chamber open to atmospheric pressure and temperature. The chamber had a 0.13 m x 0.133 m x 0.18 m test section, and was surrounded during experiments with a steady flow of 60 Standard Liters Per Minute (SLPM) of dry air to reduce particle agglomeration effects due to condensation. The surrounding air was also applied to approach air flow in a typical wind tunnel configuration, as it was injected through a flow straightening system in the testing chamber as shown in Figure 3.8. 60 SLPM was selected because it was the point at which a noticeable decrease in mean particle diameter was observed in Greene's experiments with dry, purge air in 2008 [25]. The PSA experiments were conducted at AFIT over a one month period, from November 7, 2013 to December 11, 2013. The primary goal was to control particle size through various methods. The secondary goal was to demonstrate the viability of the particle shadow imaging technique to gain particle sizing information from the flow field, which is described in the next subsection. Two different feed tubes were used to control particle concentration, while mixing air or gaseous CO_2 was injected normal to the dry ice flow to determine the effect on particle size. A total of six different injector configurations were tested, as shown in Table 3.1.
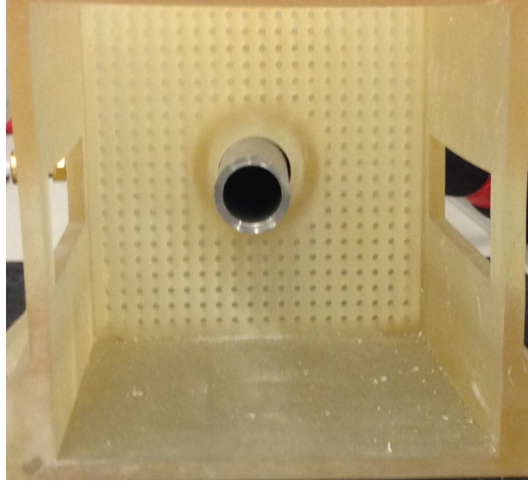
Figure 3.8: Test chamber used for AFIT experiments to replicate wind tunnel conditions

Table 3.1: Particle Sizing Experiments Performed at AFIT

Experi-ment	Date	Mixing gas	Range of Mass Flow Rate for Injected Gas (SLPM)	Feed Tube ID (mm)	Number of Images
1	11/7/2013	Air	0-160	None	255
2	12/11/2013	CO_2	0-80	None	141
3	12/2/2013	Air	0-170	1.4	291
4	12/9/2013	CO_2	0-90	1.4	176
5	12/10/2013	Air	0-170	0.76	421
6	12/10/2013	CO_2	0-80	0.76	183

3.3.1.1 Particle Shadow Imaging System.

CO_2 particle sizing information was collected from high-resolution imaging of the particles. This technique is very similar to that used for Particle Shadow Velocimetry (PSV), where a Light-Emitting Diode (LED) and high-resolution CCD camera are used for backlight illumination of the particles and recording, respectively. This inline arrangement allows the shadows created by the particles that are suspended in the flow to be recorded

46

[10]. For further background on PSV, please refer to Section 2.3. For the particle sizing experiments at AFIT, a PCO 4000 CCD camera with a 14-bit dynamic range, a 4008 pixels x 2672 pixels array and 105mm f/2.8G Nikkor lens was used to record the images while a Monarch Instrument phaser strobe was used in lieu a of a LED illumination source. An Agilent 30 MHz function/arbitrary waveform generator was used to output a square wave function to the phaser strobe and sync with the frame rate of the camera. A 2 μs time delay was set between the phaser strobe and camera. A light filter was applied in front of the phaser strobe to reduce oversaturation of the image and create an even-threshold background. Data acquisition for the images was collected using a CamWare® version 3.11 package compatible with the PCO 4000 camera. All data were attained with the following settings listed in Table 3.2 and Table 3.3. It is important to note that since only particle sizing, not velocimetry data, were required from the images, individual snapshots without regard for the time between image capture (Δt) were taken of the particles. If image pairs for PIV or PSV analysis were necessary, the appropriate Δt would have been mandatory for image processing.

Table 3.2: Camera Settings

F-stop	5.8
Zoom	0.313 m
Exposure	25.005875 ms
Delay	2 μs

Table 3.3: Pulse Signal Settings

Frequency	20 Hz
Amplitude	5 Vpp
Offset	2 V
Duty Cycle	50 %
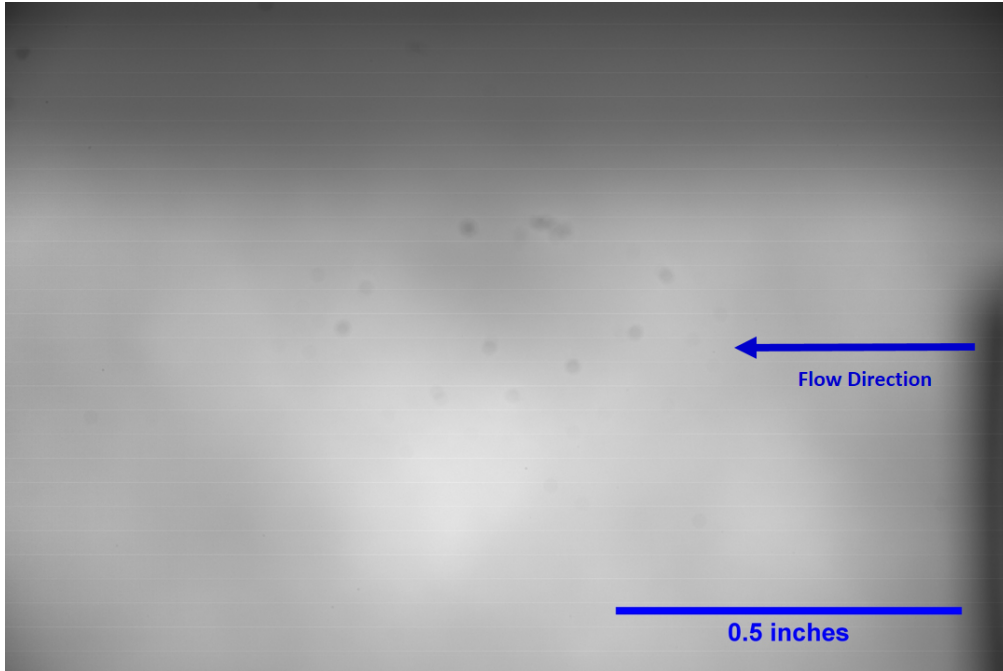
Figure 3.9: Sample field of view #1 for particle sizing experiments at AFIT (at shroud tube exit)

All images were taken at the exit of the shroud tube to approximately 33 mm downstream. The image plane was focused at the center of the shroud tube with a depth of field of 0.89 mm. For the first experiment, images were taken of the upper portion of the particles exiting the shroud tube as shown in Figure 3.9. For every experiment thereafter, images contained the entire flowfield of the particles exiting the shroud tube as shown in Figure 3.10. Image properties are shown in Table 3.4.
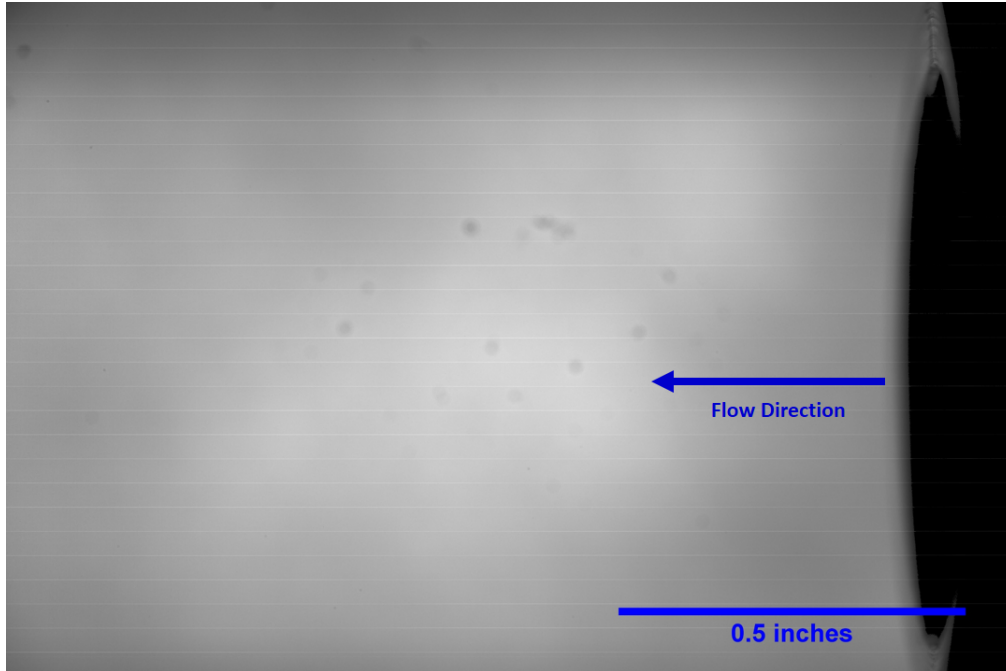
Figure 3.10: Sample field of view #2 for particle sizing experiments at AFIT (at shroud tube exit)

Table 3.4: Image Properties

Depth of Field	0.89 mm
Field of View	36.8 mm x 24.6 mm
Resolution	108.46 pixels per mm
Focus Distance	118.1 mm

3.3.1.2   *Particle Size Control Using Injected Air.*

For particle size control, an injection tube using low pressure air regulated from a supply line was used to mix air perpendicular to the flow of the dry ice particles exiting the shroud tube. As shown in Figure 3.11, the secondary injection system consisted of a a 3.18 mm (1/8 inch) OD, 1.4 mm (0.055 inch) ID, 38.1 mm (1.5 inch) long tube which was fed into an orifice in the reducing coupling. A schematic of the secondary injection system is shown in Figure 3.12. The mass flow rate of the air was regulated by an Alicat Scientific flow controller (also used to regulate the constant flow rate of the surrounding air) shown

49

in Figure 3.13. A goal of the injected air was to observe an overall reduction in particle size due to mixing as the mass flow rate of the air increased.
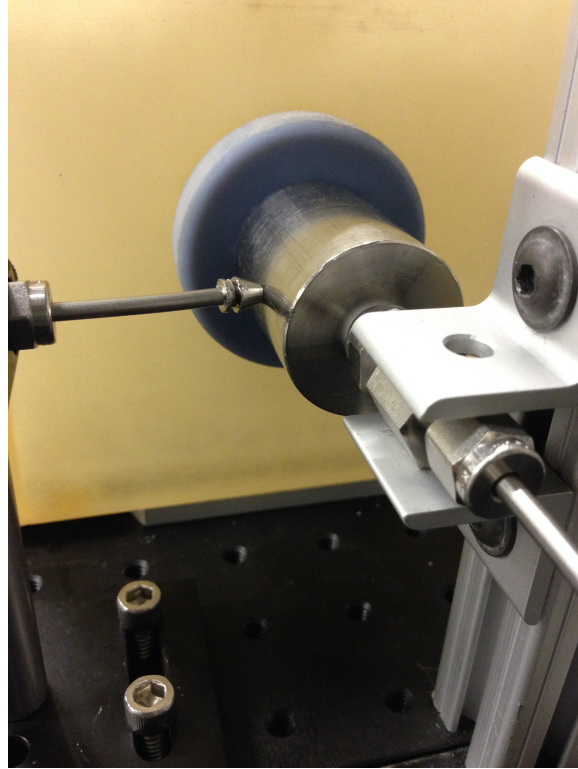
Figure 3.11: Injection tube used to mix gas with dry ice particles exiting shroud tube

3.3.1.3   *Particle Size Control Using Injected* $CO_{2(g)}$.

The same injection system was used to mix $CO_{2(g)}$ perpendicular to the flow of the dry ice particles with the exception that the $CO_{2(g)}$ was supplied from the same CO_2 container. This presented a challenge in keeping a constant $CO_{2(g)}$ supply at the higher mass flow rates. Although more $CO_{2(g)}$ was produced in the container as the $CO_{2(l)}$ was expelled, the rate of production was not sufficient to overcome the demand needed for mixing. This issue is also described in Chapter 4.
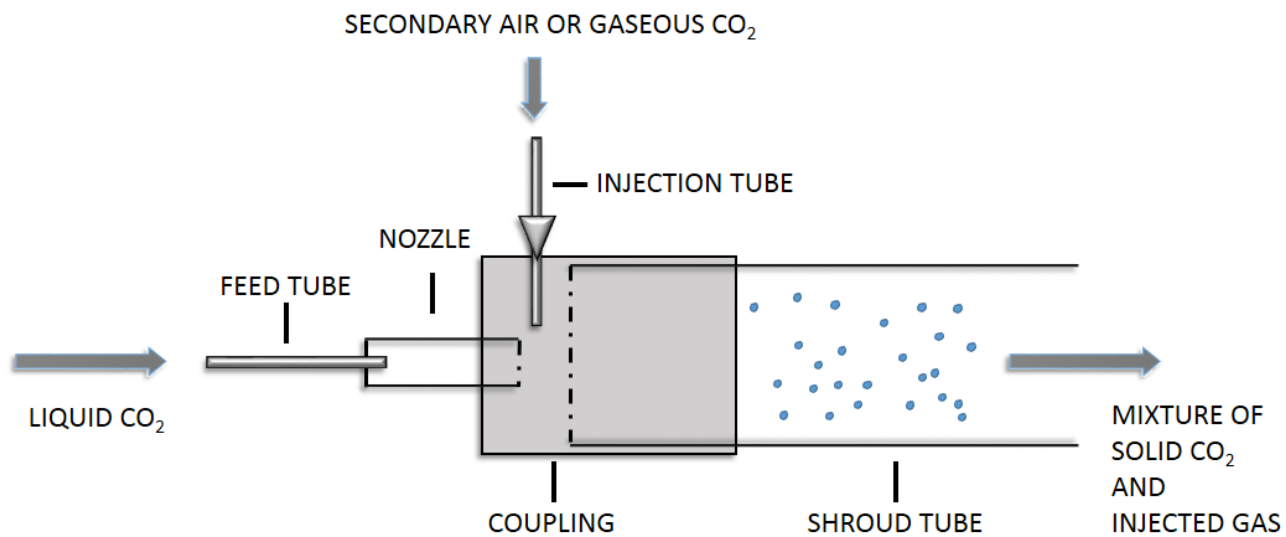
Figure 3.12: Schematic of secondary injection system with CO_2 injector
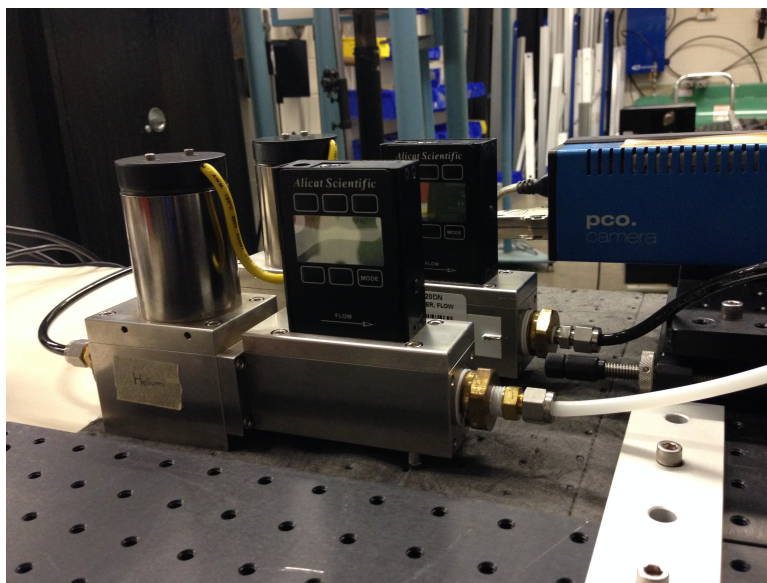
Figure 3.13: Alicat Scientific mass flow meters used for mixing gas and purge air

3.3.1.4 Particle Size Control Using Stainless Steel Mesh Filters.

Another method used to potentially control particle size was the use of different mesh screens to control particle size. The goal was to filter out larger solid CO_2 particles, allowing the smaller CO_2 particles to pass through. Because clogging was anticipated if a filter was simply applied to the exit of the shroud tube, an expansion tube made of PVC piping with a larger cross-sectional area of 60.3 mm (2.375 inch ID) shown in Figure 3.14 was devised. A side view of the shroud tube and expansion tube is shown in Figure 3.15. A plan was developed to first test the feasibility of this method with three different filters using the particle generation system with the 0.76 mm (0.03 inch) feed tube. If particle generation produced uniform, smaller particles, then a more robust filter design could be implemented. Three different filters of 0.66 mm (0.026 inch), 0.203 mm (0.008 inch), and 0.127 mm (0.005 inch) wire diameter with mesh openings of 1 mm x 1 mm (0.04 x 0.04 inch), elongated 4.76 mm x 2.39 mm (0.1875 inch x 0.094 inch), and 0.76 mm x 0.76 mm (0.03 inch x 0.03 inch) were used in the feasibility tests. Although no particle shadow images were taken with the stainless steel mesh filters in place, the results of the feasibility tests with the steel mesh filters are described in Chapter 4.
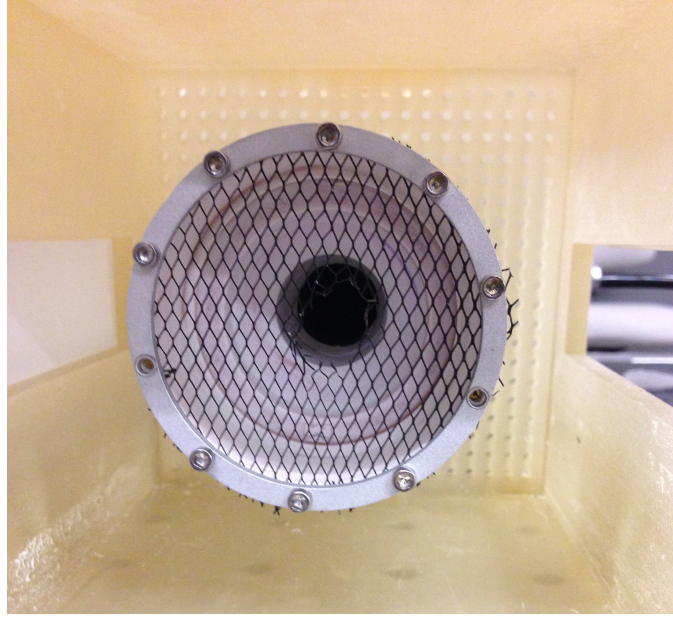
Figure 3.14: Expansion tube attached to the exit of the shroud tube with steel mesh filter
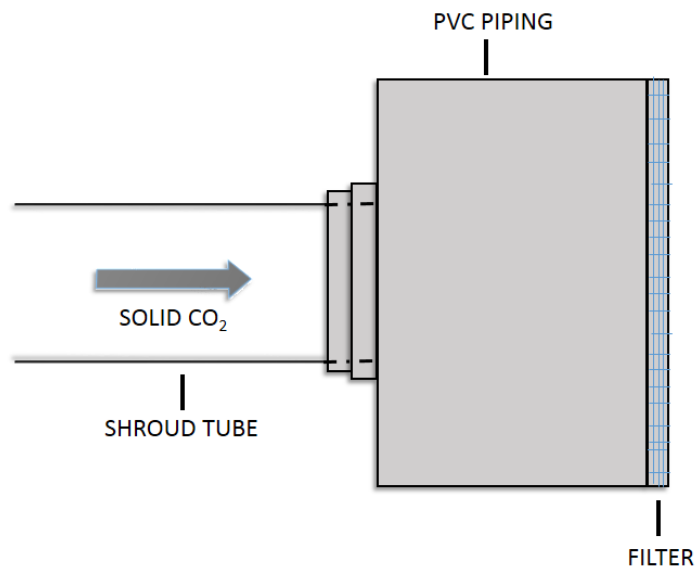
Figure 3.15: Schematic of PVC expansion tube with CO_2 injector

Prior to an experimental run, a calibration image was taken of the field of view (FOV). A sample calibration image is shown in Figure 3.16. A scale factor could then be determined from the calibration image to determine the size of the particles in focus. The measured scale factor was 108.46 pixels per mm, or approximately 9.2 μm per pixel.

With this resolution, it was not possible to resolve the size of the particles with a diameter less than 10 μm. However, the experimental approach worked well for most cases in the experiment as the particles were typically larger than 10 μm. The depth of field was determined by mounting the scale on a traversing block shown in Figure 3.17. A neutral position on the traverse was set as the focal plane and minor adjustments were made to the traverse until the image appeared out of focus on the screen. The neutral position and traversing block position when the image moved out of focus were recorded to determine the depth of field.
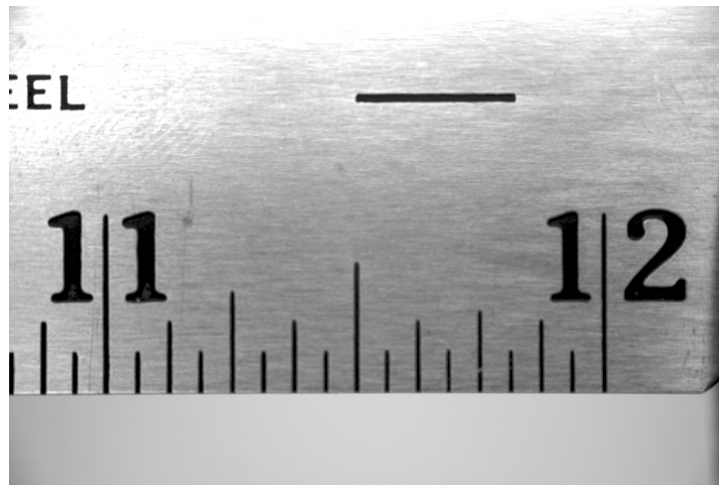
Figure 3.16: Sample calibration image of FOV
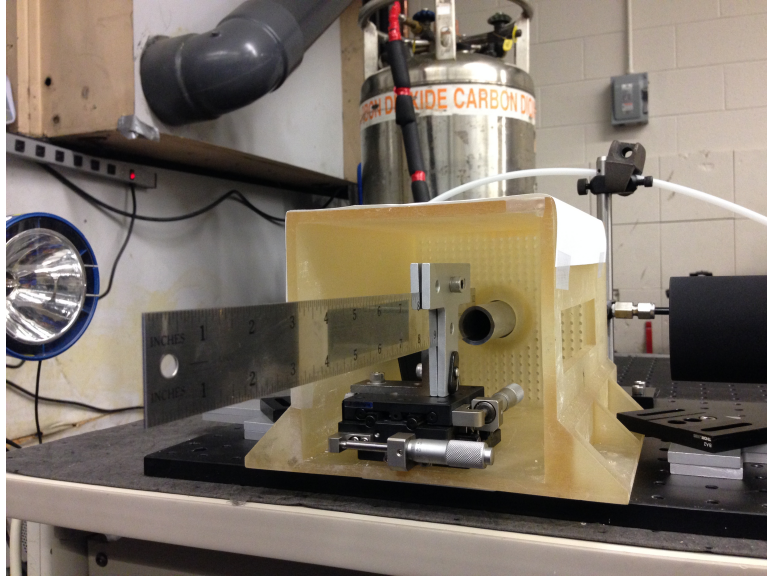
Figure 3.17: Traversing block with calibration scale used to determine depth of field

When ready to perform the experiment, a recording file was opened in the CamWare® data acquisition system and the phaser strobe was manually triggered by the waveform generator. While the images were being captured by the camera, the $CO_{2(l)}$ valve on the container was manually opened. Images of the particles exiting the shroud tube were taken for approximately 30 seconds to 1 minute, depending on the observed steadiness of the flow. For some experiments, especially the tests with the 0.76 mm (0.03 inch) feed tube, the particles would often freeze inside the tube and clog the system until the pressure became too great and released. This caused gaps in the image collection process, requiring a longer test duration. An Adam Equipment scale with a range of 0.1 kg to 500 +/- 0.1 kg and resolution of up to 1:30,000 was used to record the weight of the CO_2 container between and during experiments to determine the mass flow rate of the CO_2 particles. The humidity and temperature of the test chamber enviroment were monitored by an Accu-Rite® weather station device. The experimental setup for the particle size control tests with injected gas
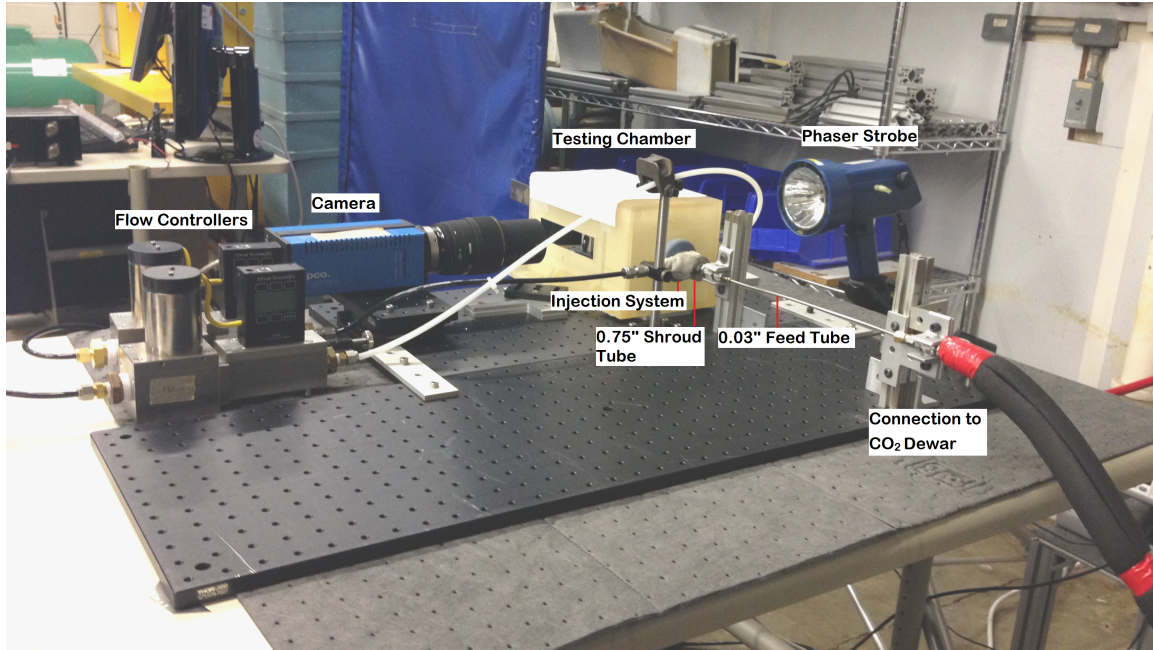
Figure 3.18: Particle size analysis experimental setup at AFIT

using the 0.76 mm (0.03 inch) ID feed tube is shown in Figure 3.18 and a schematic for the experimental setup is shown in Figure 3.19.

All experiments used the same expansion nozzle/shroud tube interface. Each test was run for approximately 30-60 seconds, depending on the configuration. Varying the feed tube diameter led to substantial differences in mass flow rate, which sometimes produced dry ice blockage in the feed tube. For instance, clogging would occur in the tests with the 0.76 mm (0.03 inch) feed tube and would necessitate longer experimental runs (resulting in more images). Images were captured solely for the purposes of sizing data, therefore no attempt was made to control the time between image capture as one would with particle shadow velocimetry. The raw data for each experiment were captured using a test matrix and are listed in the appendix. The test point matrix for experiment 6 is shown as an example in Table 3.5.
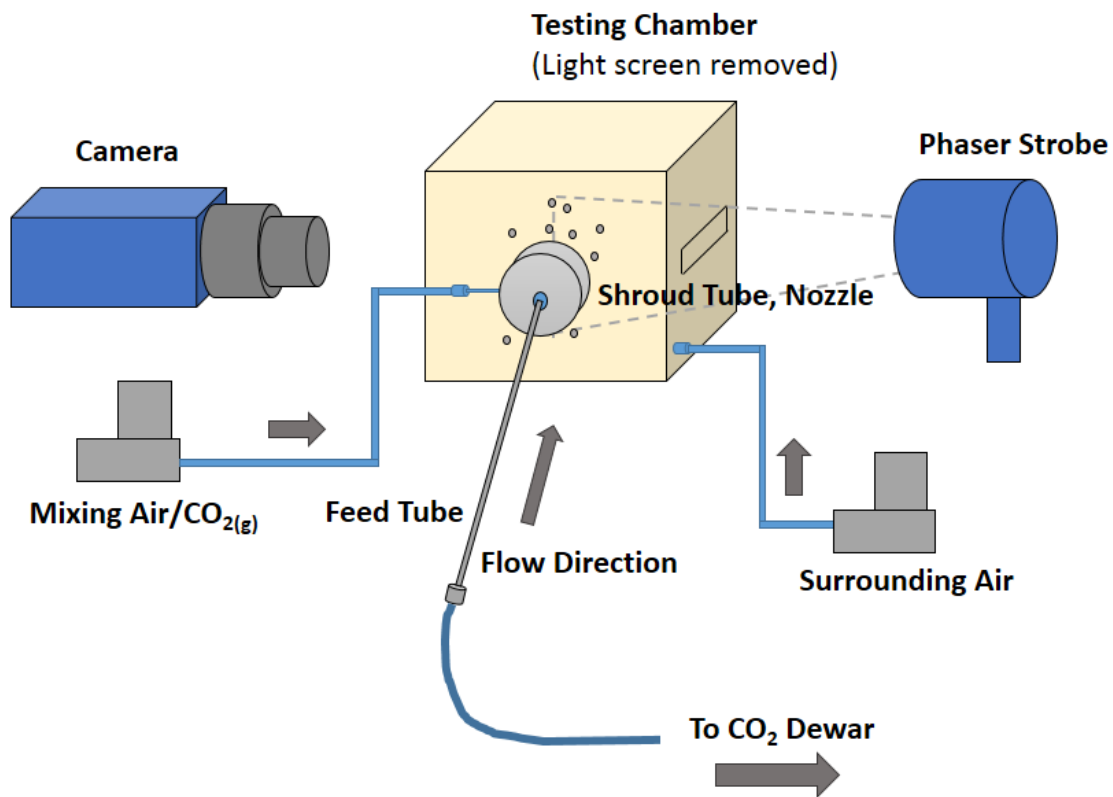
Figure 3.19: Schematic of particle size analysis experimental setup at AFIT

							CO$_2$ **Test Point Matrix for 0.76 mm ID Feed Tube**					
							Distance (at shroud exit)					
Mass flow rate of injected CO$_{2(g)}$ (SLPM)	**Mass flow rate of surrounding air (SLPM)**	**Test time (s)**	**Pulse Δ t (ms)**	**Pulse duration (μs)**	**Number of Images**	**Initial Weight of CO$_2$ dewar (kg)**	**Final Weight of CO$_2$ dewar (kg)**	**Mass flow rate of CO$_2$ (g/s)**	**Chamber temp ($^\circ$C)**	**Chamber humidity (%)**	**Dewar Tank Pressure (kPa)**
0	60	43	500	20	31	268.1	267.5	13.95	19	16	2220
10	60	60	500	20	45	267.5	267.3	3.33	19	16	2220
20	60	60	500	20	23	267.3	267.1	3.33	20	16	2220
30	60	47	500	20	37	267.1	266.8	6.38	18	16	2220
40	60	57	500	20	24	266.8	266.5	5.26	18	16	2220
50	60	52	500	20	34	266.5	266.2	5.77	18	16	2220
60	60	55	500	20	36	266.2	265.8	7.27	18	16	2220
70	60	35	500	20	29	265.8	265.5	8.57	18	16	2206
80	60	50	500	20	63	265.5	265	10	18	16	2206
90											
100											
110											
120											
130					**Inadequate supply of gaseous CO$_2$ to continue testing at higher mass flow rates**						
140											
150											
160											

Table 3.5: Test Matrix for Experiment #6 with 0.76 mm (0.03 inch) feed tube and mixing CO$_2$

3.3.2 *Particle Size Analysis Experiments at AFRL.*

Particle size analysis experiments at AFRL were conducted in an Aerolab, LLC. Educational Wind Tunnel (EWT), which is on loan to AFRL from AFIT, using the same automated imaging technique that was used at AFIT. The purpose of these tests were twofold. One goal was to demonstrate the viability of measuring particle size using the shadow imaging technique in a subsonic wind tunnel, and second, to determine the feasibility of particle size control with the use of injected air in the shroud tube at different test conditions. Images were taken at the inlet section and at the test section of the EWT for a comparison of the particle size distribution at each location. The images at the test section were taken of particles in uniform flow in an empty test section. It is important to note that the goal of these experiments was for merely observing trends in the data and not to achieve a desired particle size.

Five particle sizing analysis experiments were conducted from Jan. 17 to Jan. 23, 2014 at free stream velocities of Mach 0.026, Mach 0.05, Mach 0.08, Mach 0.1, and Mach 0.13. The tests were performed on days of low humidity to prevent vapor from condensing on the dry ice surface. As previously accomplished in the AFIT experiments, increased mass flow rates of air were injected perpendicularly into the shroud tube to control particle size. Data comparison in the results section is only given for the Mach 0.026, Mach 0.08 and Mach 0.13 experiments to show a net particle size reduction effect. The test conditions for each experiment are shown in Table 3.6. The raw data for each experiment were captured using a similar test matrix to the one used for the AFIT experiments and are listed in the appendix.

Table 3.6: Test Conditions for Particle Sizing Experiments at AFRL

Experi-ment	Date	Wind Tunnel Freestream Speed (mph)	Calculated Mach Number @ 17 °C	Test Section Static Pressure Differential (kPa)	Range of Mass Flow Rate of Air (SLPM)	Average Ambient Humidity (%)	Number of Processed Images	Image Location
1	1/22/2014	20	0.026	0.05	0-120	16	320	Inlet Section
2	1/22/2014	40	0.05	0.2	0-120	17.4	320	Inlet Section
3	1/22/2014	60	0.08	0.44	0-120	16.7	320	Inlet Section
4	1/22/2014	80	0.1	0.78	0-120	16	320	Inlet Section
5	1/22/2014	100	0.13	1.22	0-120	17.1	320	Inlet Section
6	1/20/2014	20	0.026	0.04	0-120	N/A	337	Test Section
7	1/20/2014	40	0.05	0.17	0-120	N/A	188	Test Section
8	1/20/2014	60	0.08	0.42	0-120	N/A	199	Test Section
9	1/20/2014	80	0.1	0.76	0-120	N/A	155	Test Section
10	1/20/2014	100	0.13	1.2	0-100	N/A	328	Test Section
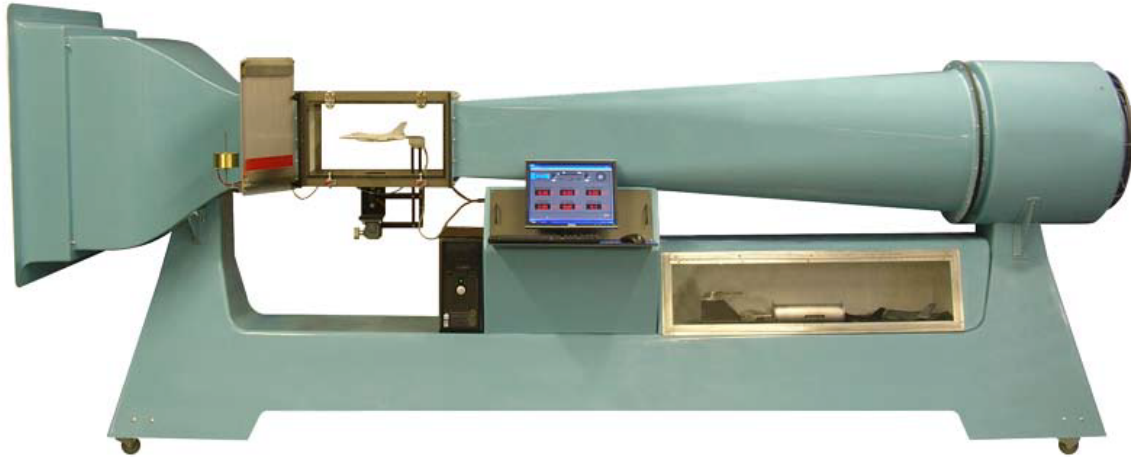
Figure 3.20: Aerolab Educational Wind Tunnel [26]

3.3.2.1 *Educational Wind Tunnel.*

The Aerolab Educational Wind Tunnel (EWT) at AFRL shown in Figure 3.20 is an open-circuit, subsonic tunnel with test section dimensions of 0.3 m x 0.3 m x 0.61 m. The tunnel is capable of airspeeds ranging from 0 to 64.8 m/s (0 to 145 mph), and has a turbulence intensity level of less than 0.2% when the honeycomb flow straightener and stainless steel mesh screens are installed. An orifice ring of four pressure ports on each wall upstream of the test section provides the average static pressure of the section, which can be used as a reference pressure [27].

3.3.2.2 *Particle Shadow Imaging System.*

Experiments in the EWT were conducted with a PCO 1600 CCD camera with a 14-bit dynamic range, a 1600 pixels x 1200 pixels array and 180 mm f/2.8 Nikkor lens. An Innovative Scientific Solutions (ISSI) LM4-X RGB LED lamp with an applied light screen provided backlight illumination of the particles. Red filtered light was used for all experiments since the CCD camera has a higher spectral sensitivity in the upper-red region [14]. Timing of the LED pulses and camera shutter was controlled within

61

the data acquisition software, DaVis 8.1.1 by LaVision in conjunction with an internal Programmable Timing Unit version 9 (PTU 9). Although typically used for precision timing with 16 independent channels for laser firing with PIV, the PTU 9 provided the same ability to control the pulse duration, time between pulses and time of exposure for the LED lamp. Images collected at the inlet and test section were both acquired with the camera settings in Table 3.7.

Table 3.7: Camera Settings

F-stop	2.8
Zoom	1.5 m
Exposure	Various, ranging from 5 μs to 20 μs
Delay	0 μs

The particle shadow imaging system was arranged identically to the setup at AFIT, with the exception that the flow was captured moving left to right. Figure 3.21 shows the calibration images and experimental setups at the inlet and test sections of the EWT. A bellows in lieu of a spacing ring was used to magnify the image plane even further. Calibration to determine the FOV and depth of field was also performed in the same manner with the same calibration scale and traversing block prior to each experiment. A built-in scaling function in the DaVis 8.1.1 was used to calculate the scaling factor and FOV. The image properties for the inlet section are shown in Table 3.8 and the image properties for the test section are shown in Table 3.9.
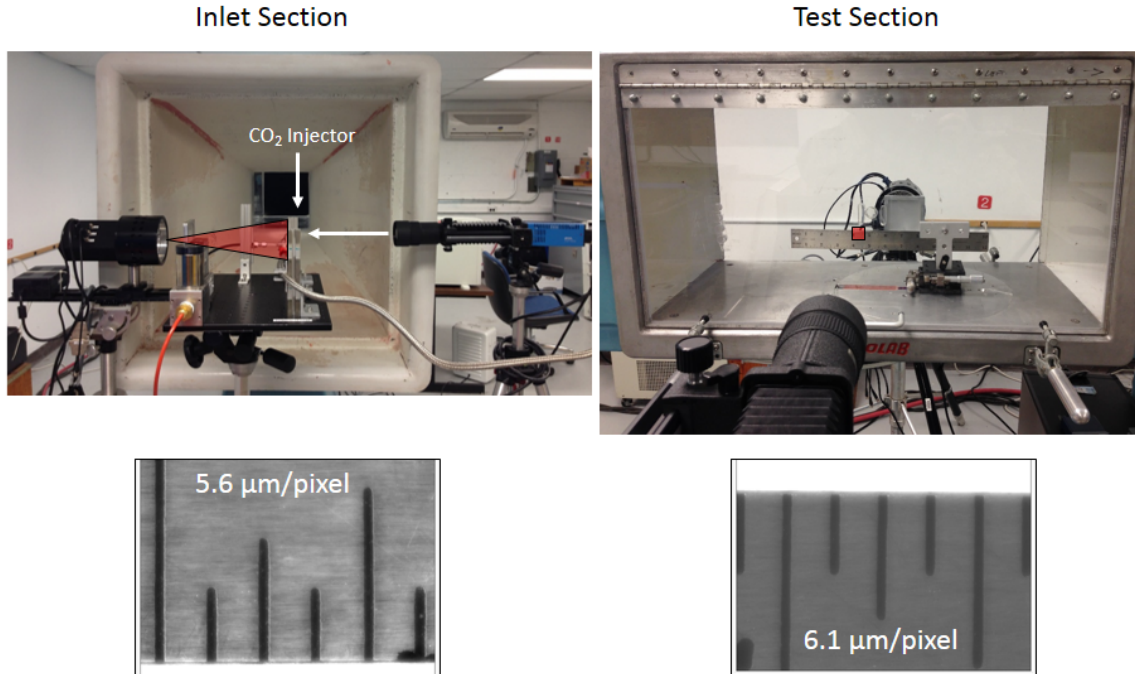
Figure 3.21: Particle shadow imaging setup at AFRL with EWT

Table 3.8: Image Properties for Inlet Section

Depth of Field	0.71 mm
Field of View	9.73 mm x 7.29 mm
Resolution	177.76 pixels/mm (5.6 μm/pixel)
Focus Distance	342.9 mm

Table 3.9: Image Properties for Test Section

Depth of Field	1 mm
Field of View	9.73 mm x 7.29 mm
Resolution	4179 pixels/inch (6.1 μm/pixel)
Focus Distance	0.33 m
Distance from CO_2 injection to test section FOV	1.14 m

Particle generation was conducted in an ambient environment, since the inlet of the tunnel was open to atmospheric pressure and temperature. However, environmental conditions at AFRL differed from the conditions at AFIT (approximately a 15 degree temperature difference) that caused the LCO_2 to turn solid in the stainless steel flexible hose line. A reduction in dewar head pressure from 2379 kPa to 1724 kPa (345 psi to 250 psi) was applied to reduce the expansion ratio from the liquid to solid CO_2. Originally, a configuration utilizing the 0.76 mm (0.03 inch) feed tube with the expansion nozzle and shroud tube was envisioned as the particle generation system of choice as it produced small, discrete particles optimal for image processing. However, seeding density became too low by the time the particles reached the test section. A slight improvement in test section seeding density was not enough to utilize the 1.4 mm (0.055 inch) feed tube either, necessitating the removal of a feed tube altogether.

Injected air was utilized as the particle size control mechanism due to its greater success with reducing average particle diameter with the 0.76 mm (0.03 inch) feed tube. With the exception of one experiment when images were taken at the test section for a wind tunnel speed of 44.7 m/s, mass flow rates of 0 to 120 SLPM in increments of 40 SLPM were introduced to the CO_2 flow. The upper limit of 120 SLPM was selected due to the pressure set point limitations of the AFRL Ingersoll-Rand air compressors.

The honeycomb flow straightener and stainless steel mesh screens were removed during the PSA experiments due to the fact that the dry ice particles tended to aggolomerate on the screens and reduce the seeding concentration in the tunnel test section. The particle generation and air injection system were mounted on a tripod upstream of the tunnel's inlet duct as shown in Figure 3.22. For the images captured in the test section, the shroud tube exit was centered in the middle of the inlet duct and placed 0.15 m (6 inches) downstream of the inlet duct to center the flow seeding in the middle of the test section and maximize the concentration of seed particles, respectively. The distance from the shroud tube exit to
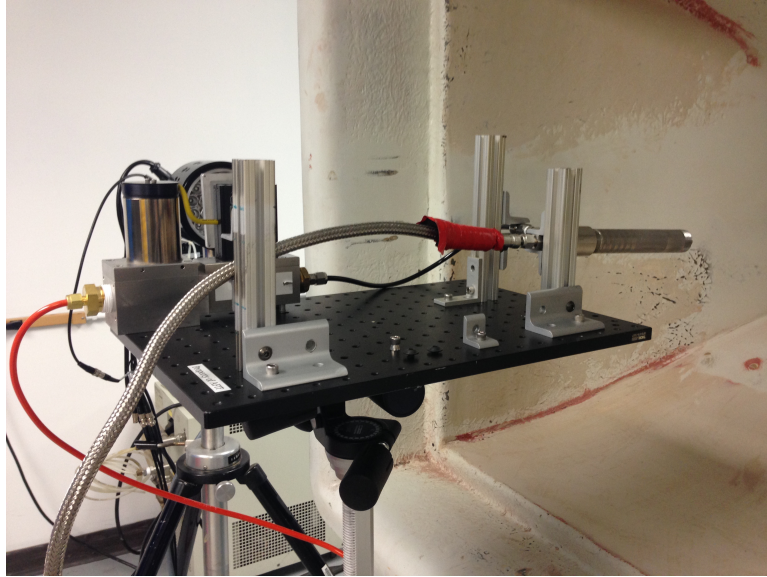
Figure 3.22: Particle generation and air injection setup for use in the EWT

the image field of view was approximately 1.14 m (45 inches). This distance was used as the reference distance used in the sublimation rate calculations (in Chapter 4). Test seeding runs were performed to visually inspect successful generation of particles in the center of the test section on Jan. 17, 2014 and to determine the best location for the particle shadow imaging system. Because the honeycomb flow straighteners and screens were removed for consistent particle persistence into the test section, the flow became extremely turbulent and did not allow for a steady flow of particles to cross into the FOV of the camera. The height of the camera and LED source had to be adjusted several times during the course of the experiments as the Mach number increased in order to acquire images with CO_2 particles. An example image for the Mach 0.08 case that reflects the sparse seeding encountered is shown in Figure 3.23. For comparison, an example image for the Mach 0.08 case at the inlet section is shown in Figure 3.24. The lack of ideal seeding in this area was rectified by increasing the number of images captured in order to increase the sample size for an accurate particle distribution in the test section. This problem would have been an issue if

taking velocimetry measurements, for much higher seeding densities are a requirement for cross-correlation interrogation analysis. However, since the images were captured solely for the purposes of representative sizing data, the sparse seeding was determined to be acceptable.
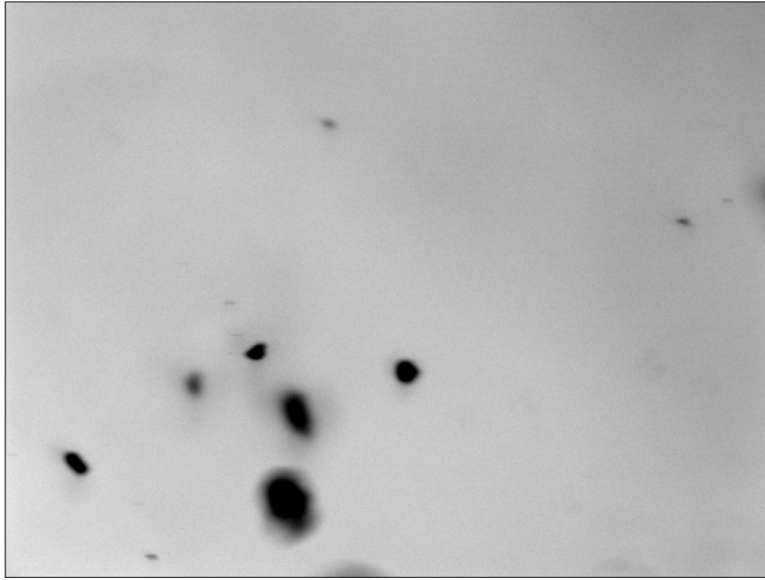
Figure 3.23: Example image of particles at tunnel test section at Mach 0.08 with 120 SLPM of injected air
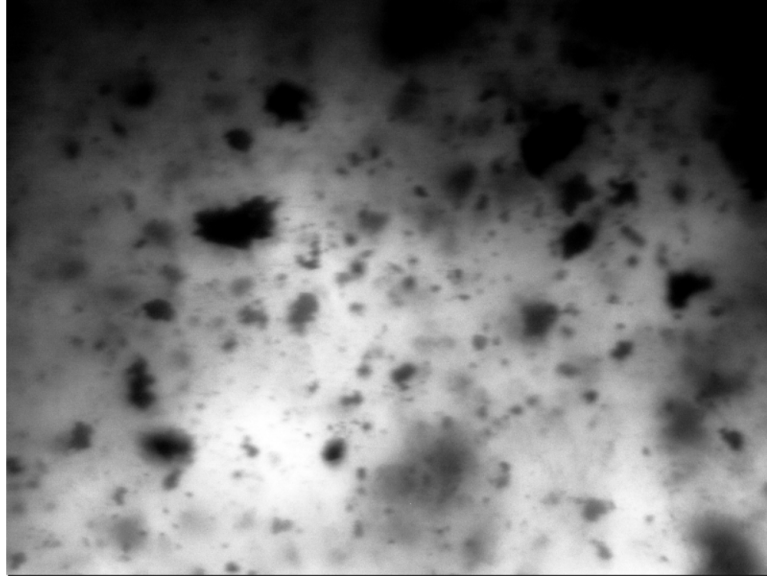
Figure 3.24: Example image of particles at tunnel inlet section
for Mach 0.08 with 120 SLPM of injected air

For the images captured at the inlet section, the shroud tube exit was relocated approximately 0.3 m (12 inches) upstream from the inlet duct but still centered in order to acquire the images with the camera and LED. The images from the EWT inlet section contain many more CO_2 particles, as the flow has not yet fully spread and entered the turbulent environment of the wind tunnel. Unlike the shadow imaging conducted at AFIT, pictures were taken 0.076 m (3 inches) downstream of the shroud tube exit to better capture discrete particles and and increase amount of light entering the CCD in the camera.

3.3.3 Image Processing and Sizing Analysis.

All shadow images were processed using ImageJ, an open-source, Java-based image processing software available from the National Institute of Health (NIH). The software has been used successfully in other areas of research, such as particle size distribution of gravel in Civil Engineering applications [28] and gene expression analysis for biotechnology research [29]. It is is capable of reading many image formats, so there was no loss of resolution in processing the data. ImageJ has many options available to process a series of images, including background subtraction and noise filtering. It is also able to measure particle area statistics in a 2-D image, including particle size based on pixel count. Different image processing methods were applied depending upon the variations in background and particle intensity (grayscale images), but for the most part processing and and sizing analysis were performed in three steps. First, a scale was set from the calibration image using the built-in straight line tool. Next, the images were pre-processed. Here, pre-processing is defined as the image manipulation prior to performing particle size measurements, e.g., background subtraction. Lastly, particle characteristic measurements were extracted from the images from various calculations based on the enclosed area of each particle. Images for processing were selected based on image quality (ability to distinguish between particles and noise), particle count and whether or not they displayed an accurate representation of the flow. The number of images that were selected were given as "processed images" in Table 3.1 and Table 3.6. Plots of particle size distribution and sizing analysis were created from these measurements and will be discussed in Chapter 4.

3.3.3.1 Image Processing for Particle Sizing Experiments at AFIT.

Processing of an image began by excluding parts of the image that contained non-particle data, i.e. the shroud tube exit. A noise reduction median filter called "remove outliers" was then applied to the images. This operation was selected because it is very

useful in removing the "dead" pixels of a CCD camera, which are the thin lines observed in all of the particle shadow images. For this research, the removed outliers were replaced by a pixel by the median of the pixels in the surrounding radius if it deviated from the median threshold by more than 0 counts. A radius of 20 pixels for the "bright" pixels was used to calculate the median value. Next, a background subtraction called "sliding paraboloid" was performed to correct intensity fluctuations from an unevenly illuminated background. This method takes a 2-D grayscale image and computes the intensity value at every point, creating a surface plot with intensity as the third dimension. Then, a paraboloid of a specified curvature (user input in pixels) is "rolled" underneath the the intensity fluctuations of the surface plot. The area underneath the curve (intensity values) are then subtracted from the surface plot. A curvature of 50 pixels produced the best results. This process is shown in Figure 3.25. Next, the auto threshold tool was used to set upper and lower threshold values for the image to distinguish the background from the particles. The user was required to set a threshold for the images as it created a binary image of particles and background. This binary image (convert to mask) was later used to count the particles and calculate their respective areas. The default threshold setting in ImageJ was used because applying a certain upper limit and lower limit would not produce quality images. After applying a threshold, additional noise filtering was conducted via the "remove outliers" operation. This time, however, small dark pixels (radius of 2) with a threshold of 0 were removed from the images. After this step, an operation called "find edges" was applied. This highlights sharp changes in intensity using a Sobel operator (used in image processing, particularly with edge detection algorithms) that approximates the derivative of the continuous image intensity function, or sets the boundaries of a particle [30]. This was particularly useful in the next section when calculating the area of each particle. Figure 3.26 shows a sample image undergoing each processing step described above.
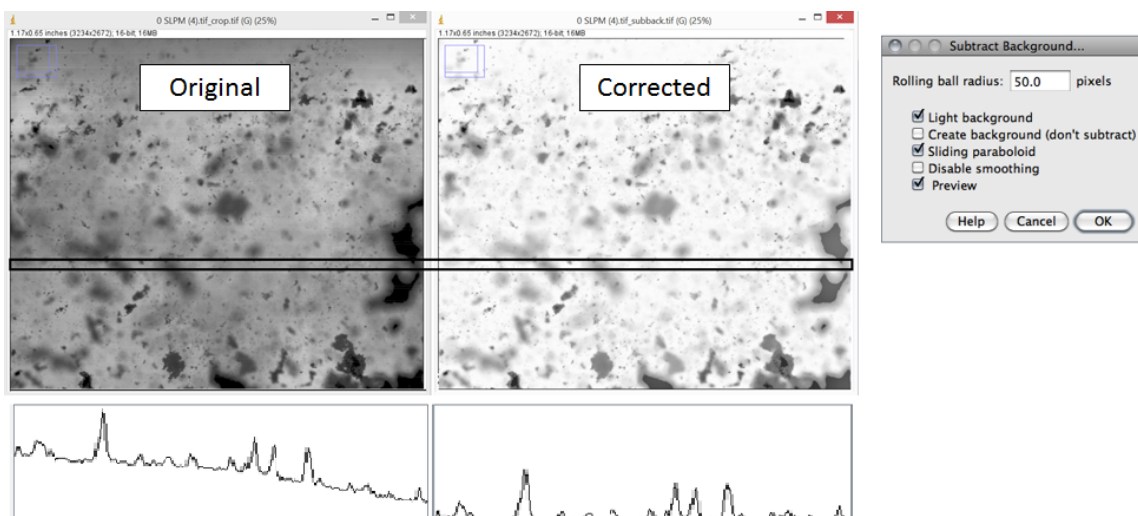
Figure 3.25: Sliding Paraboloid background subtraction demonstration [30]
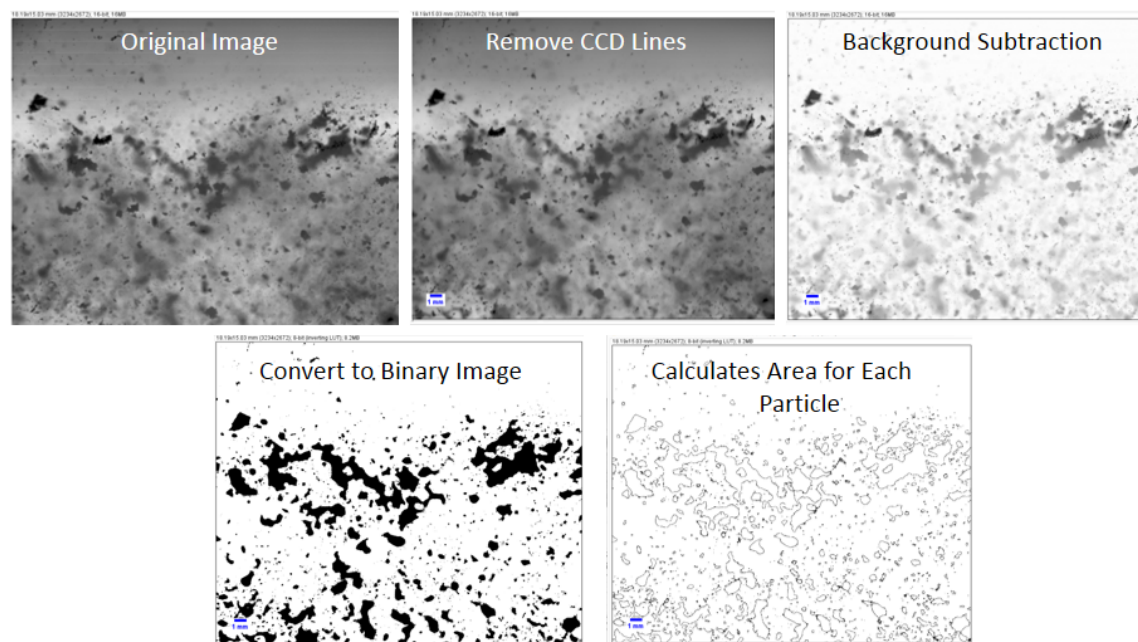
Figure 3.26: Sample image undergoing processing for bench test particle sizing experiments at AFIT

3.3.3.2 Image Processing for Particle Sizing Experiments at AFRL.

First, a sliding paraboloid background subtraction with a curvature of 100 pixels was performed to the images obtained in the AFRL particle sizing experiments. Next, a flat intensity level of 100 counts was subtracted from each image to further reduce background noise that added to erroneous particle size measurements. A default auto threshold was applied as with the image processing with the AFIT particle sizing experiments. Next, the "remove outliers" operation was applied to reduce noise of dark objects of 2 pixels or less. Figure 3.27 shows a sample image undergoing each processing step described above. The original image appears much darker than the processed images because the images were saved with a higher dynamic range (16-bit) and were later converted to 8-bit during the image processing.
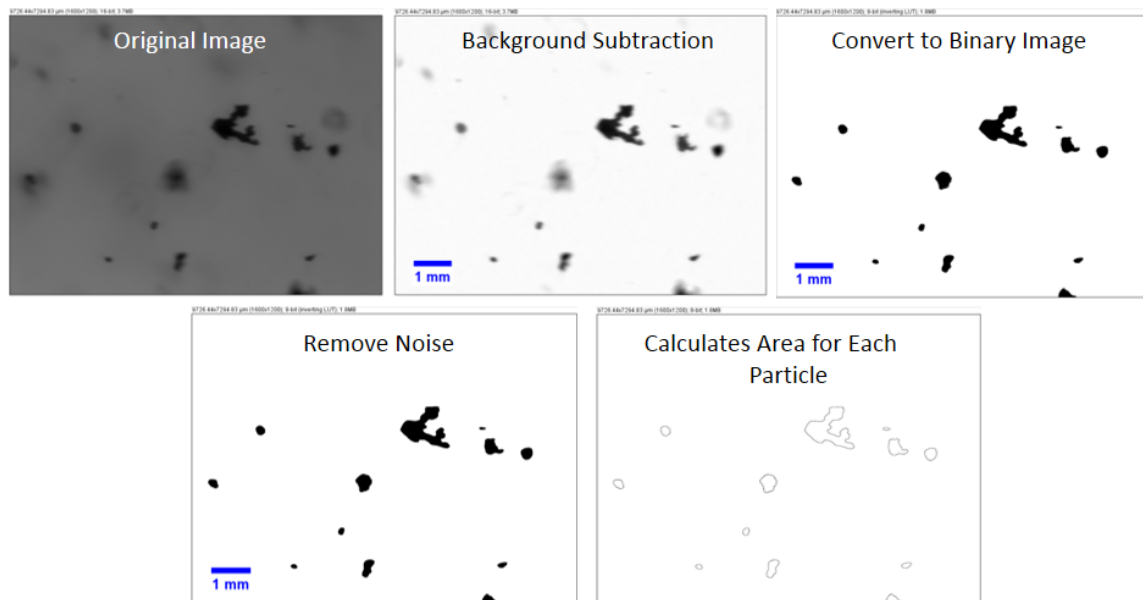
Figure 3.27: Sample image undergoing processing for particle sizing experiments in EWT at AFRL

3.3.3.3 *Particle Analysis.*

The particle analysis feature in ImageJ was used to measure the area, shape descriptors (circularity, aspect ratio, etc.), centroid and perimeter. The feature operates by scanning the entire image until it finds the edge of a particle (threshold value above 0 for a light background). It then creates an outline of each particle using the built-in "wand tool," measures each particle using the "measure" command (counts the number of pixels for each object), fills the particle with zeros to make it invisible, and then continues scanning the rest of the image until it reaches the last pixel of the image. The particle analysis feature includes other options such as only counting a specific particle size, particles with a certain circularity and exclusion of particles on the edges of an image. During the processing for this research, particles with a size of 0 to infinity (area in μm^2) and circularity of 0.00 to 1 were included for the images acquired in the AFIT particle sizing experiments and with a size of 0.06 to infinity and circularity of 0.00 to 0.99, respectively. The threshold limits on particle size were set by careful processing of select individual images and observing the particle count. Data output was given in the form of a spreadsheet and included the particle count, surface area and calculated area-equivalent diameter corresponding to each respective image.

IV.   Results

The results are broadly characterized by three different approaches to improving the fidelity of CO_2 seeding for PIV applications. First, re-processed results of a subset of the boundary layer PIV conducted at the AFRL/RQ TGF are presented. The results obtained by Wolfe [12] were previously not compared to any other experimental measurements. However, in the summer of 2013, AFRL collected boundary layer data using a Pitot probe. A conclusion of the PIV boundary layer measurements in the TGF was that particle size control would lead to better PIV results. In particular, a reduction in particle diameter and a more uniform size distribution would improve the flow tracking capability. This led to the particle sizing analysis tests at AFIT and AFRL. Particle distributions and particle statistics from the image-based particle sizing experiments are discussed second and compared to previous results that used a different experimental technique. Third, a demonstration of particle size control and the shadow imaging technique was conducted in the EWT at AFRL in order to document the changes in particle size distribution between the injection point and the test section. Particle distributions and statistics for the demonstration are summarized and compared to the data acquired at AFIT. Sublimation rate calculations were also performed using the wind tunnel data.

4.1   Turbulent Boundary Layer Measurements Compared to Previous Research

4.1.1   Summary of Previous Research.

Stereoscopic PIV boundary layer measurements in the TGF at AFRL were taken by Wolfe [12] in September 2011 using dry ice particles. Free stream velocities were set at Mach 0.3, 0.5, or Mach 0.8 at stagnation pressures ranging from 23.94 to 115 kPa (500 to 2400 psf). The particle generation system consisted of a distribution manifold with eight 20.9 mm (0.824 inch) ID shroud tubes that could be interchanged with 9.25

73
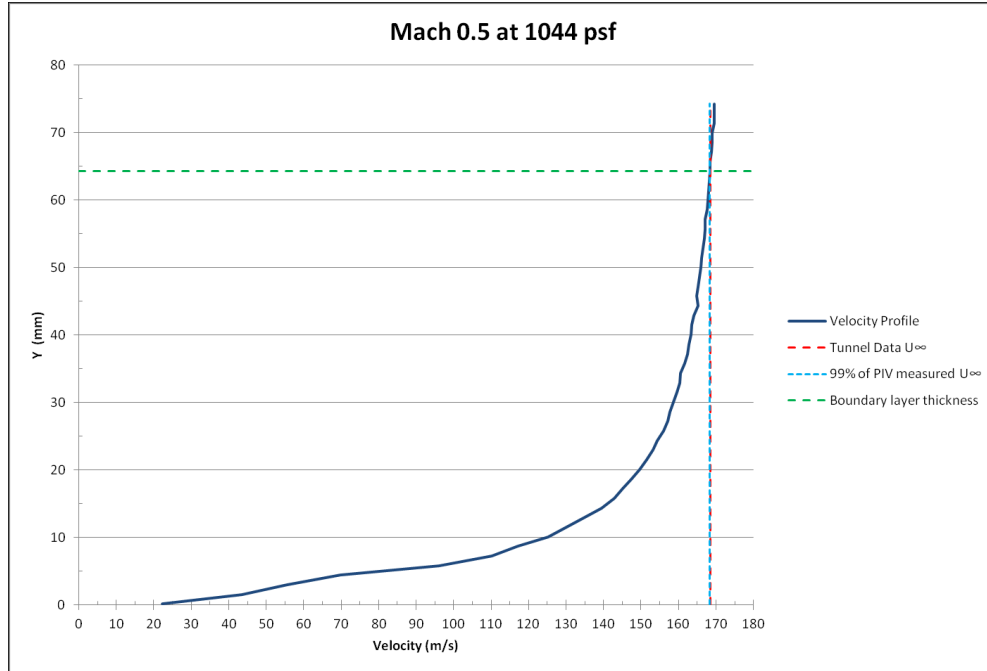
Figure 4.1: Velocity profile for 20.9 mm (0.824 inch) ID shroud tubes

mm (0.364 inch) ID shroud tubes. For further details regarding the boundary layer PIV experiments, including the experimental methodology and data processing, please refer to the introduction or Reference [12].

4.1.2   *Turbulent Boundary Layer Comparison.*

Velocity profiles from the PIV data were generated for the wind tunnel boundary layer for each experimental condition, however, special attention was given to the Mach 0.5 at 50 kPa (1044 psf) with the 20.9 mm ID shroud tubes case due to the high statistical sampling of images (10,000 image pairs). The original velocity profile measured by Wolfe is shown in Figure 4.1. The velocity profile resembles that of a typical compressible turbulent boundary layer profile over a flat plate, where streamwise velocity is slower at the wall and increases exponentially until it reaches the free stream. Nevertheless, the boundary layer thickness (δ) for the original PIV profile was more than double when compared to the Pitot probe velocity

74
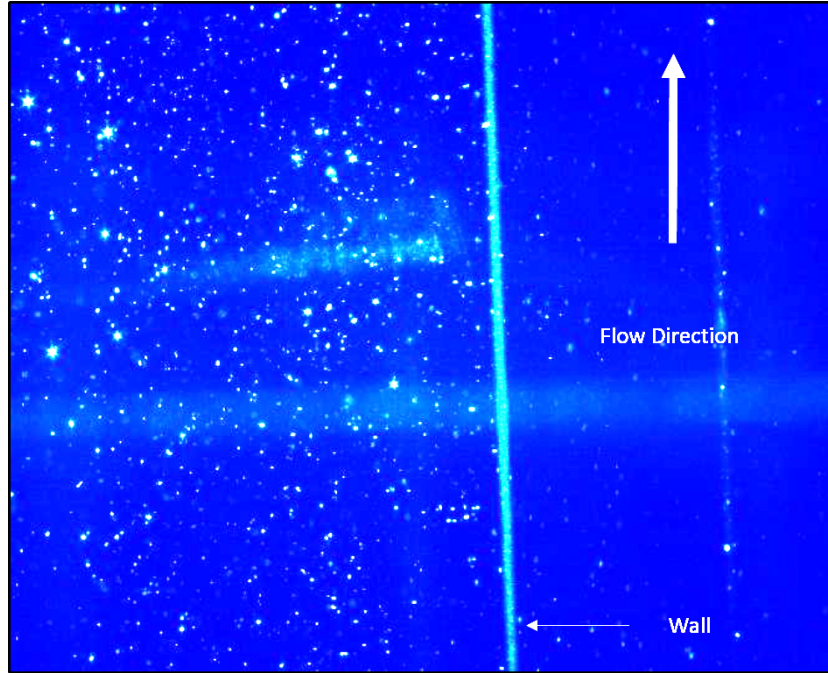
Figure 4.2: Sample PIV image taken from camera 1 for Mach 0.5 at 50 kPa (1044 psf)

profile in Figure 4.3. The boundary layer thickness for the original PIV profile was 64 mm, while δ for the Pitot probe data was determined to be 31 mm [12]. Reasons for the potential discrepancy are cited as due to "an unknown separation between the window and the edge of the calibration plate which introduced some ambiguity as to the precise location of the wall measurement in the calibrated images. This ambiguity, of just 3 or 4 mm, resulted in large shifts of the data when plotted [12]." Because there is some uncertainty in the exact location of the wall, there is a possiblility that the velocity measurements near the wall in the original PIV processing were not very accurate. Figure 4.1 shows the lowest measured velocity is approximately 22 m/s at y = 0 mm. In contrast, the Pitot probe data shows a velocity of 135.8 m/s (U_0 = 173 m/s) at y = 2.54 mm. A sample image (Figure 4.2) taken from the 10,000 image pair set reveals reduced particle concentration near the wall (given by the light sheet), which would make reliable velocity measurments in the interrogation regions near the wall very difficult with the original PIV processing. Therefore, refined

PIV processing was performed to improve the data processing through careful selection of image processing/image calibration techniques with the goal of increasing the accuracy for flow tracking.

Re-processing of the 10,000 image set was performed with additional noise reduction and calibration techniques for the refined PIV processing and with individual particle correlation for the PIV + PTV method as described in 3.1. A summary of the baseline image processing and improved image processing techniques is shown in Table 4.1. The most important step of the refined PIV technique was the application of the self-calibration feature, which reduced the disparity vector (see 3.1 for an explanation) by 10.6 pixels (0.47 mm). The re-processed PIV and PIV + PTV profiles are shown in Figure 4.3 and are compared against the previous data, two log law solutions for the boundary layer for an incompressible turbulent boundary layer (using the Pitot probe flow parameters) and data collected with a Pitot probe on a different day. Figure 4.4 provides a closer view from $U/U_0 = 0.7$ to $U/U_0 = 1$. Velocity data is normalized due to slight variations in stagnation pressures/ temperatures. The original PIV profile was taken across a region with minimal reflections, while the refined PIV profile was averaged over the entire FOV after additional noise reduction. The PIV + PTV profile was generated from Camera 1 only and taken across a region with minimal noise. Table 4.3 compares boundary layer thickness (δ_{99}), displacement thickness (δ^*), momentum thickness (θ) and shape factor (H) for four different profiles.

Table 4.1: Processing Changes

Process Change	Baseline Method (Previous Research)	Re-processed PIV Method	PIV + PTV Method	Advantages
Noise reduction settings	Background Subtraction	Sliding Average Subtraction + Background Subtraction	Background subtraction	Improved signal-to-noise ratio, reduction in false vectors
Correlation	Stereo cross-correlation: 512x128 pixel elliptical sub-regions with 50% overlap (1) 256x64 pixel elliptical IR with 50% overlap on second pass (1)	Stereo cross-correlation: 512x128 pixel elliptical sub-regions with 50% overlap (1) 256x64 pixel elliptical IR with 50% overlap multi pass (3)	Cross-correlation: Same vector calculation as re-processed PIV, however addition of individual particle window interpolation & single-particle correlation	Shifts interrogation window to include more particles in calculation
Calibration correction for stereoscopic images	None	Yes	None (single camera)	Reduces disparity between laser sheet and calibration plate misalignment
Minimum threshold of valid vectors	200	1000	200	Improved reliability/confidence in vector maps
Correlation Coefficient (Q)	<1.5	<1.3	None	Does not remove as many vectors in regions with high gradients. A higher Q-factor is ideal for flow averages and RMS
Masking	None	Data masked outside area of interest	Data masked outside best quality regions	Eliminates unwanted data that contributes to erroneous vector calculations
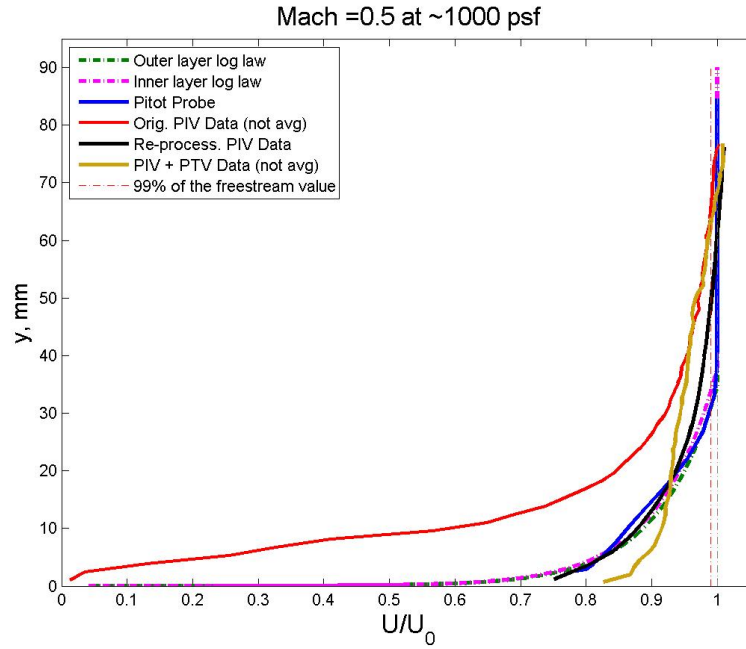
Figure 4.3: Velocity profile comparison of theoretical incompressible turbulent boundary layer log laws, Pitot probe data, original PIV data, re-processed PIV data and PIV + PTV data
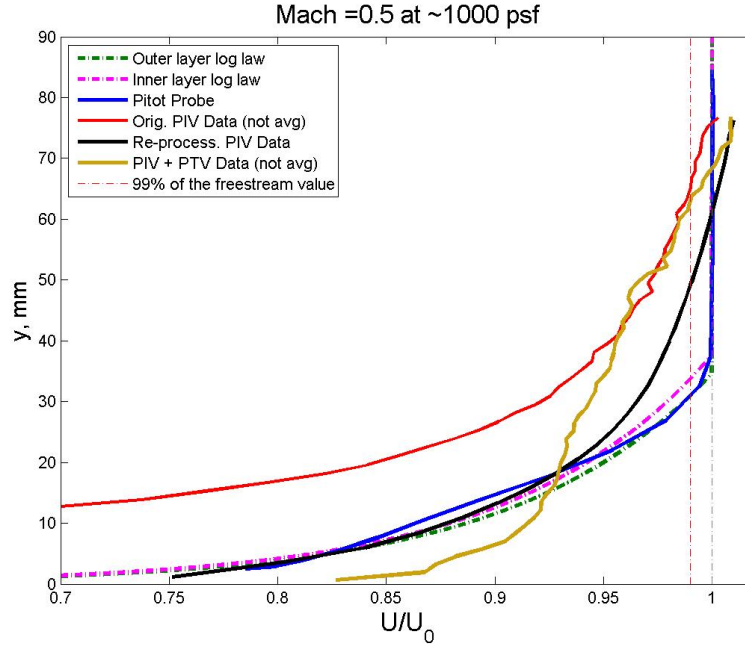
Figure 4.4: Close-up view of turbulent boundary layer velocity profiles

The theoretical log law profiles were calculated using the Pitot probe flow parameters. The re-processed PIV data most closely resembles the inner layer log law closer to the wall (approximately $y/\delta < 0.3$). Near the free stream, however, the re-processed PIV profile diverges from the inner log law and Pitot probe result near $U/U_0 = 0.9276$ and then continues past the free stream velocity. This free stream "drift" is evident in all PIV processed data and is described in further detail in Section 4.1.3. Near the free stream, Pitot probe data matches well with the outer log layer as expected ($y^+ > 50$). A table of values comparing the deviations between the Pitot probe and re-processed PIV data velocity profile is shown in Table 4.2. The re-processed PIV free stream difference was within 1% of wind tunnel calculations and within 1.76% of the previous PIV results, respectively. A table showing the wind tunnel conditions for that particular run is given in the Appendix A. The PIV + PTV profile does not resemble either the log law or Pitot probe profiles,

however, it does show an increase in streamwise velocity as the distance from the wall is increased.

Table 4.2: Velocity Profile Comparison of Pitot Probe Data and Re-processed PIV Data

Distance from wall (y in mm)	Pitot Probe Velocity (U/U_0)	Re-processed PIV Data (U/U_0)	Percent Difference (%)
2.54	0.7852	0.7812	0.51
2.90	0.7993	0.7885	1.35
3.84	0.8113	0.8065	0.59
5.44	0.8271	0.8323	0.63
7.57	0.8454	0.8569	1.36
10.54	0.8669	0.8819	1.73
13.79	0.8928	0.9039	1.24
17.68	0.924	0.9254	0.15
22.07	0.9542	0.9438	1.09
26.90	0.9788	0.9582	2.10
32.46	0.994	0.9699	2.42
37.64	0.9994	0.9772	2.22
43.46	0.9996	0.9841	1.55
49.43	0.9999	0.9902	0.97
55.55	1.0004	0.9955	0.49
61.80	1.0002	1.0002	0.00
67.49	0.9999	1.0041	0.42
73.25	1.0002	1.0075	0.73

Table 4.3: Comparison of Boundary Layer Parameters

Profile	δ (mm)	δ^* (mm)	θ (mm)	H
Outer Log Law Layer	31	3.15	2.58	1.22
Inner Log Law Layer	33.8	3.43	2.81	1.22
Pitot Probe	31	2.02	2.33	0.87
Refined PIV	49.3	3.89	3.35	1.16
PIV + PTV	63	3.55	3.29	1.08

4.1.3 Sources of Error for Refined Turbulent Boundary Layer Profiles.

A possible contributor to the free stream "drift" associated with PIV and PIV + PTV profiles was first hypothesized as due to the initial velocity of the particles when they were injected into the wind tunnel. Since coflow injection was accomplished in the stagnation chamber, it was conceivable that an initial velocity of the particles may have caused them to accelerate faster than the free stream. However, the validity of this assumption is disputable based on the particle sizing experiments conducted at AFIT. The initial average velocity of the particles entering a 20.9 mm (0.824 inch) ID shroud tube injector with no feed tube was calculated to be approximately 2 m/s, close to the velocity in the settling chamber. The distance from the injection point to the laser sheet was approximately 12.2 m (40 feet), which also shows that the particles had ample time to reach the free stream velocity.

4.2 Particle Size Analysis at AFIT

Particle size was controlled by introducing dry air or gaseous carbon dioxide into the solid carbon dioxide injector as described in Chapter 3. Reductions in particle size were observed for all experimental cases. It is important to note that the data provided in the next few sections was for comparative information only, and not an attempt to reach a desired particle size. The 20.9 mm (0.824 inch) CO_2 injector was purposely selected for the experiments due to resolution uncertainties with the new shadow imaging technique and because it had been applied in a wind tunnel environment. Data from experimental cases 1, 2, 5 and 6 were only included to provide the net effect of restricting $CO_{2(l)}$ mass flow rate prior to solid CO_2 production. The graphs for experimental cases 3 and 4 are provided in Appendix C.

4.2.1 *Effect on Particle Size Due to Mixing Air & Mixing Gaseous* CO_2.

In general, as the mass flow rate of the air mixing with the CO_2 particles was increased, particle size decreased. Using the readings from the weight scale between experimental runs, the mass flow rates of the CO_2 particles were calculated to be 17.4 g/s for a particle generation system without a feed tube, and 3.2 g/s for a particle generation system using the 0.76 mm (0.03 inch) ID feed tube, respectively. Particle concentration became significantly reduced when the mass flow rate of the air reached 160 SLPM, potentially eliminating the smaller particles. However, for the gaseous CO_2, particle concentration did not reduce at 160 SLPM with the 0.76 mm (0.03 inch) feed tube. Figs. 4.5 to 4.8 give a visual representation of the effects due to mixing air and mixing gaseous CO_2. for experimental cases 1, 2, 5 and 6.
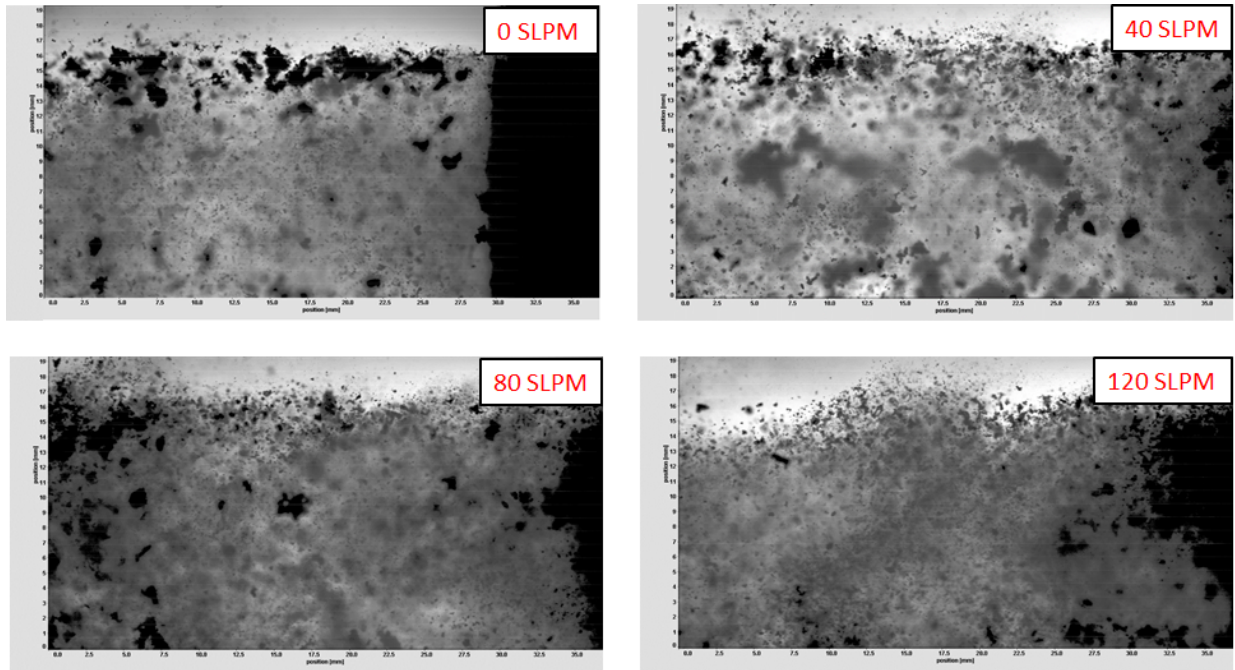
Figure 4.5: The effect of injecting dry air on CO_2 particle size (expansion nozzle only)
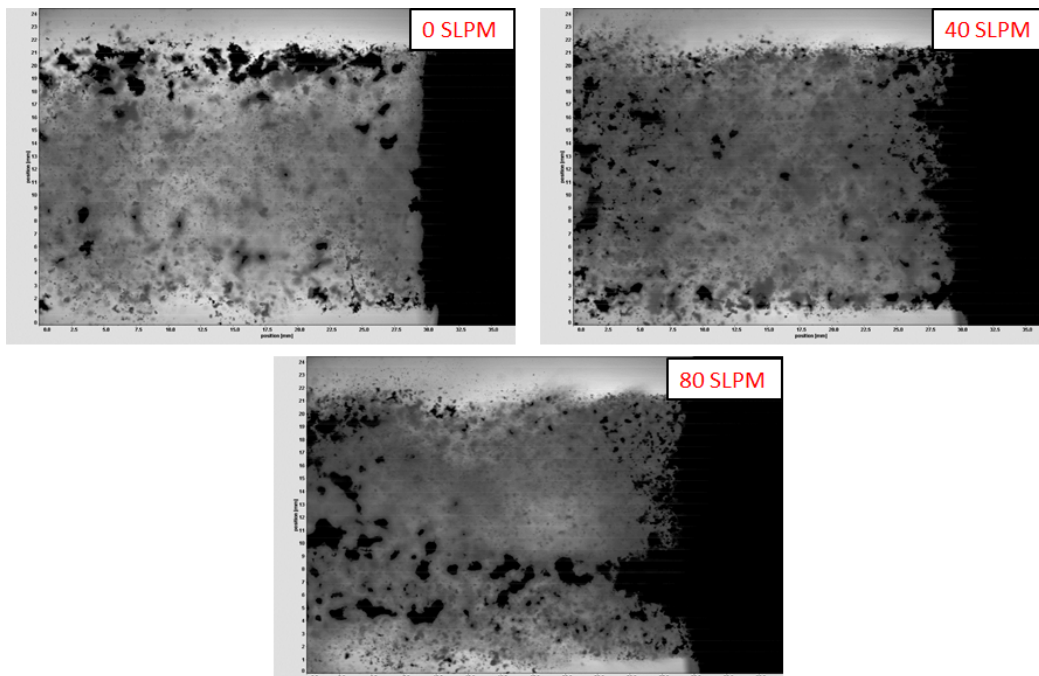
Figure 4.6: The effect of injecting gaseous CO_2 on CO_2 particle size (expansion nozzle only)
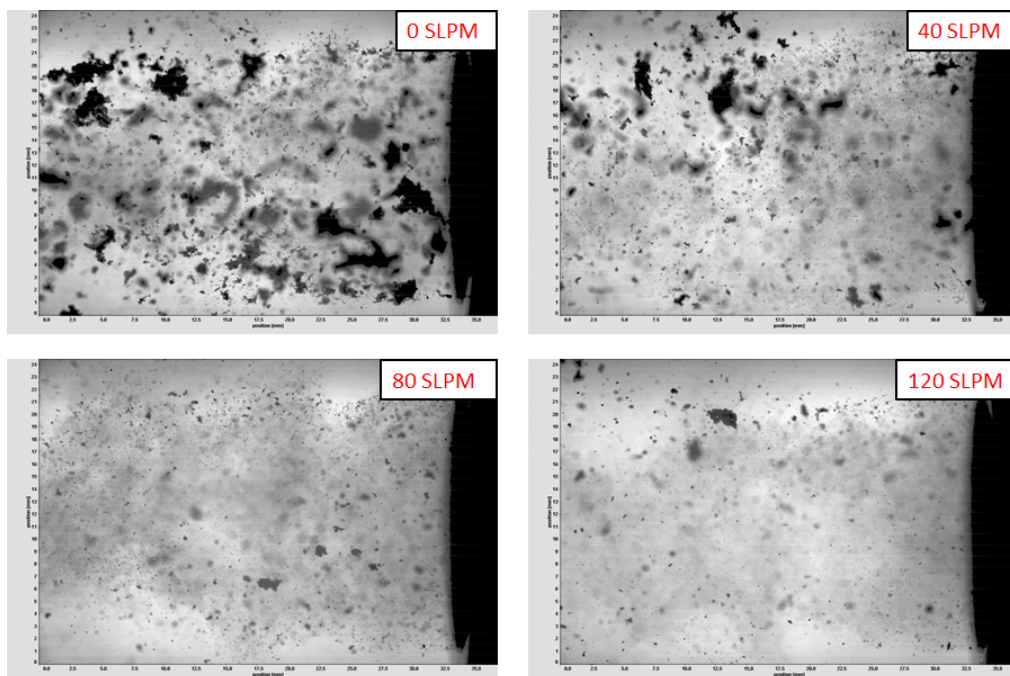
Figure 4.7: The effect of injecting dry air on CO_2 particle size (mass flow restricted with 0.76 mm (0.03 inch) ID feed tube)
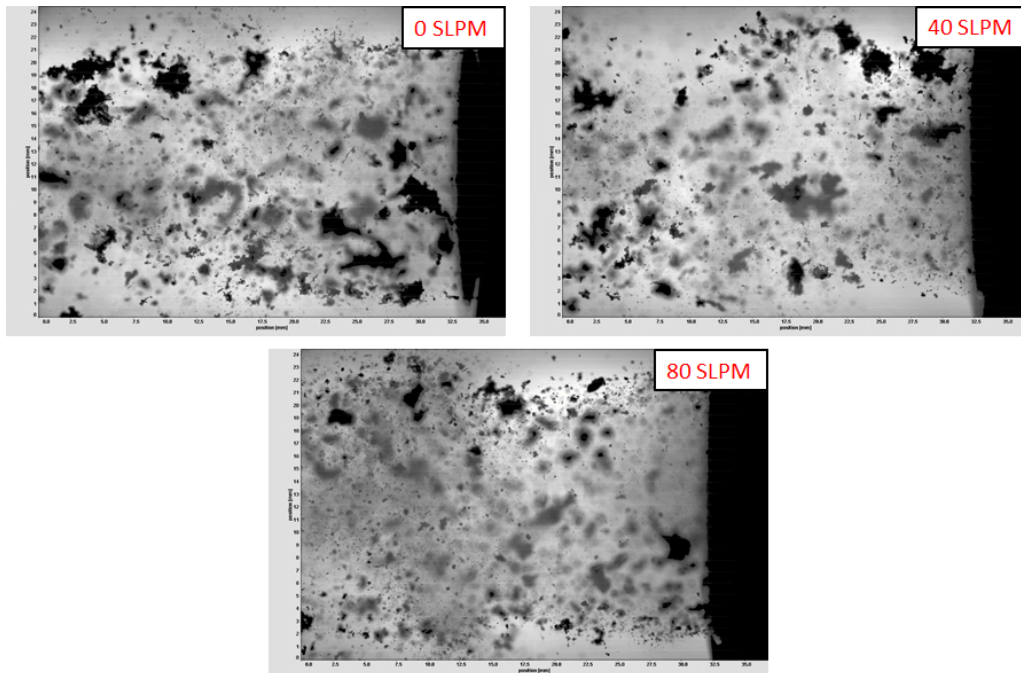
Figure 4.8: The effect of injecting gaseous CO_2 on CO_2 (mass flow restricted with 0.76 mm (0.03 inch) ID feed tube)

The upper limit of the mass flow rates for the injected air (160 SLPM) and injected gaseous CO_2 (80 SLPM) were selected based on the pressure set point limitations of the air supply line at AFIT and the supply of gaseous CO_2 from the same dewar as the solid CO_2 particles, respectively.

4.3 Particle Size Distributions and Statistics at AFIT

The particle size distributions for experimental cases 1, 2, 5 and 6 are shown in Figure 4.9, Figure 4.10, Figure 4.11, and Figure 4.12, respectively. The particle diameter is based on a surface area-equivalent diameter, which was calculated using the particle sizing analysis feature in ImageJ. For each case, the most frequent particle encountered was 80 μm or less. Bulk particle diameter was between 40 μm and 80 μm for each case, with the exception of Figure 4.10. Although not as profound with the injected air cases (Figure 4.9 and Figure 4.11), trends show an increase in the number of larger particles (distribution shift from 20-40 μm to 40-80 μm in Figure 4.10 and Figure 4.12) with the reduction of $CO_{2(l)}$ mass flow rate due to a longer residence time in the shroud tube. These observations are consistent with the conclusions made by Love in 2010.

It is important to note that the experimental technique and particle injector were different from the methods used by Greene [25] and Love [18] using the Malvern Spraytec particle analyzer. As a result, the particle diameters are much larger than the previous measurements. For the particle sizing experiments using shadow imaging, particle sizing was accomplished via image processing techniques. In comparison, the Malvern Spraytec system used a laser diffraction system that allowed real time measurements of particle size and distibution using Mie theory and Fraunhofer approximation models [23]. Greene used shroud tube IDs ranging from 3.18 mm to 9.53 mm (0.125 inch to 0.375 inch) and Love used shroud tube IDs ranging from 7.87 mm to 10.16 mm (0.31 inch to 0.40 inch), whereas the shroud tube ID used in this research was 20.9 mm (0.824 inch)–the same

injector used in the boundary layer wind tunnel experiments in 2011. Greene demonstrated that increased shroud tube diameters produced larger particles, which would also explain the larger particle diameters in this research.
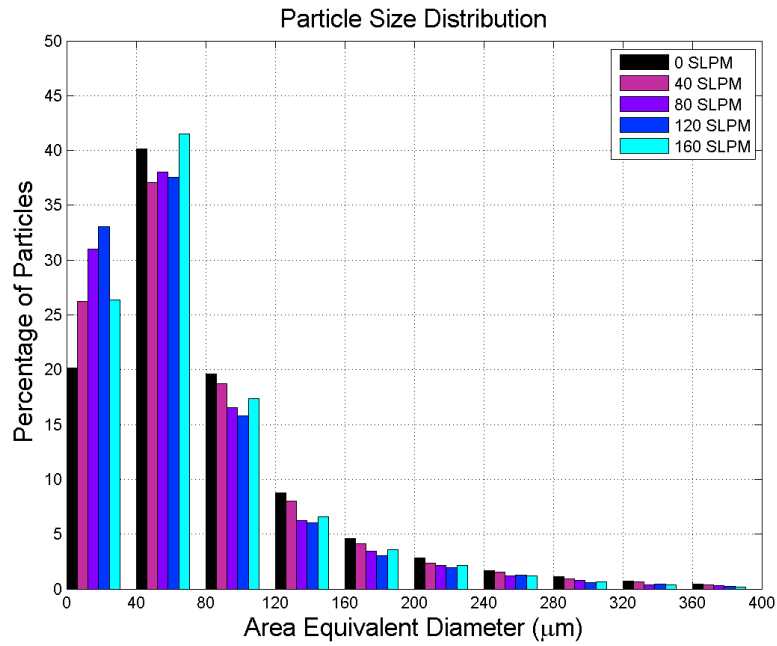
Figure 4.9: Particle Size Distribution: expansion nozzle only with injected air (mass flow rate of 17.4 g/s)
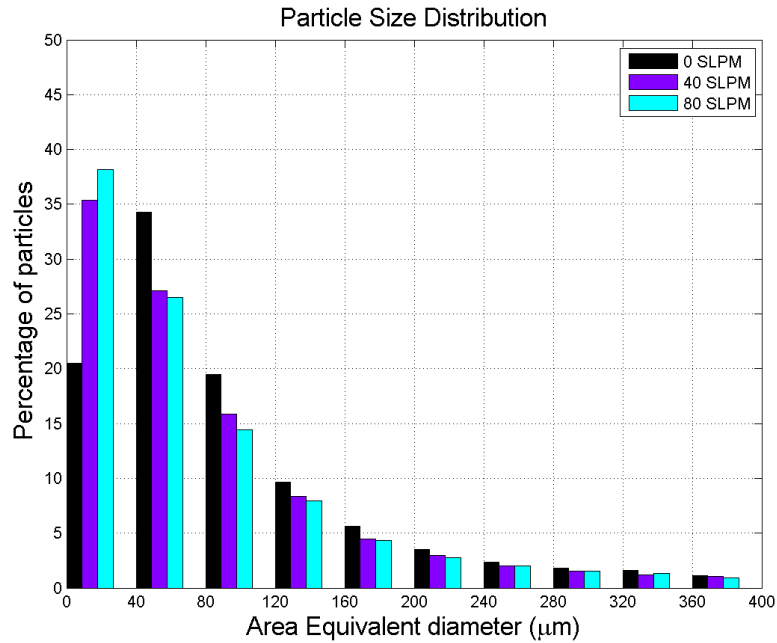
Figure 4.10: Particle Size Distribution: expansion nozzle only with injected gaseous carbon dioxide (mass flow rate of 17.4 g/s)
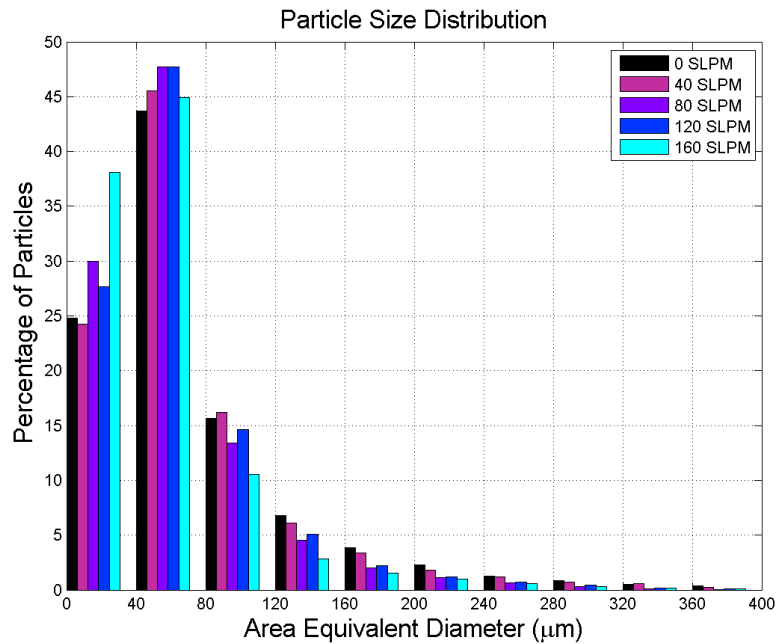
Figure 4.11: Particle Size Distribution: with 0.76 mm (0.03 inch) feed tube with injected air (mass flow rate of 3.2 g/s)
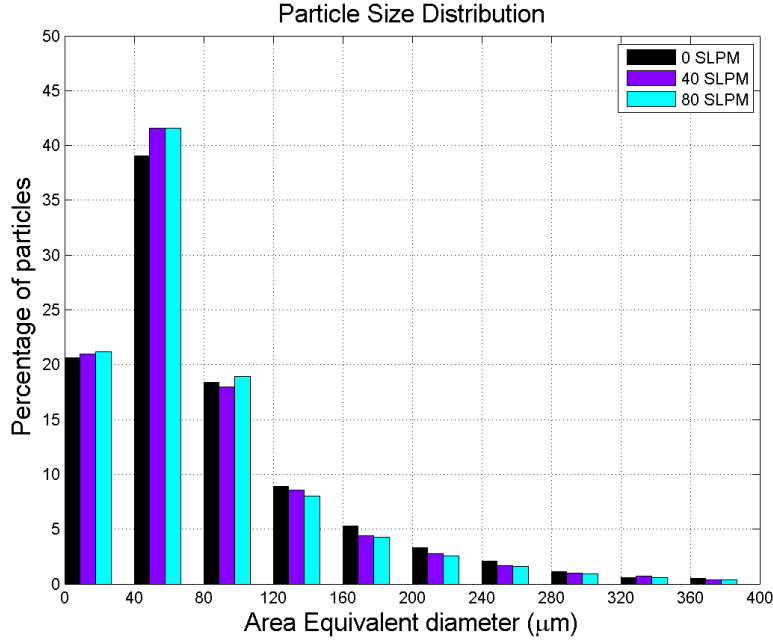
Figure 4.12: Particle Size Distribution: with 0.76 mm (0.03 inch) feed tube with injected gaseous carbon dioxide (mass flow rate of 3.2 g/s)

4.3.1 *Measured Average Particle Diameter and Sauter Mean Diameter.*

A comparison of the average area equivalent diameter and Sauter mean diameter (D_{32}) for the experiments using the injected air are shown in Figure 4.13 and Figure 4.15. Comparable graphs for the experiments using injected gaseous CO_2 are shown in Figure 4.14 and Figure 4.16. In previous research, the Sauter mean diameter was calculated using the Malvern Spraytec particle analyzer system, which produced a volume weighted distribution. The image analysis technique used in the current research produced both a number weighted distribution (area equivalent diameter), where each particle is given equal weighting irrespective of its size [31], and a volume weighted distribution. For the purposes of direct comparison with previous research using the Malvern system, D_{32} is calculated here.
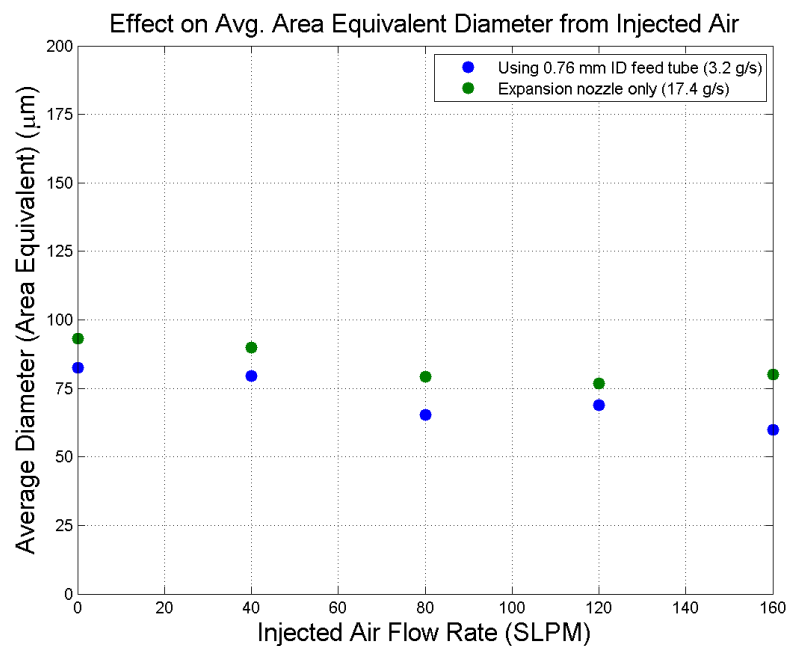
Figure 4.13: Particle statistics: effect of injected air on average area-equivalent diameter
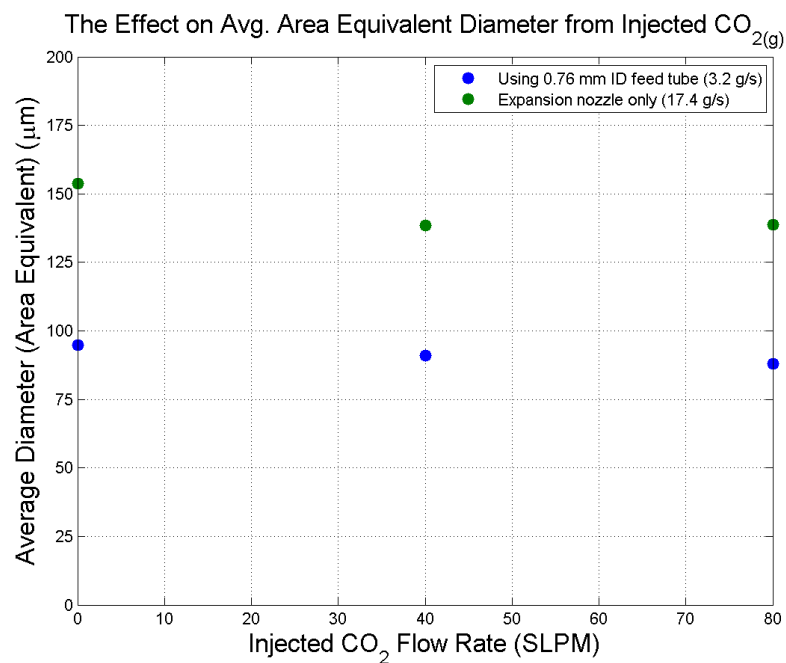
Figure 4.14: Particle statistics: effect of injected gaseous CO_2 on average area-equivalent diameter

In Figure 4.13, it is clear that there is a reduction in average area-equivalent particle diameter as the injected flow rate of air is increased for both experimental cases. For an accurate comparison between the experiments using injected dry air and gaseous CO_2, values above 80 SLPM will not be considered due to the supply limitation of the gaseous CO_2. The greatest observed decrease in average particle diameter in Figure 4.13 was with the 0.76 mm (0.03 inch) ID feed tube, where average particle diameter decreased by approximately 17 μm, or 21% from 0 SLPM to 80 SLPM of injected air. This is consistent with what was observed in the shadow images, as shown in Figure 4.7. A decrease in average area-equivalent diameter was less pronounced with the injection of gaseous CO_2 for the both experimental cases as shown in Figure 4.14, where a reduction of only 7 μm or 8% was observed for the experiment utilizing the 0.76 mm (0.03 inch) feed tube and approximately 15 μm or 10% with the absence of a feed tube.
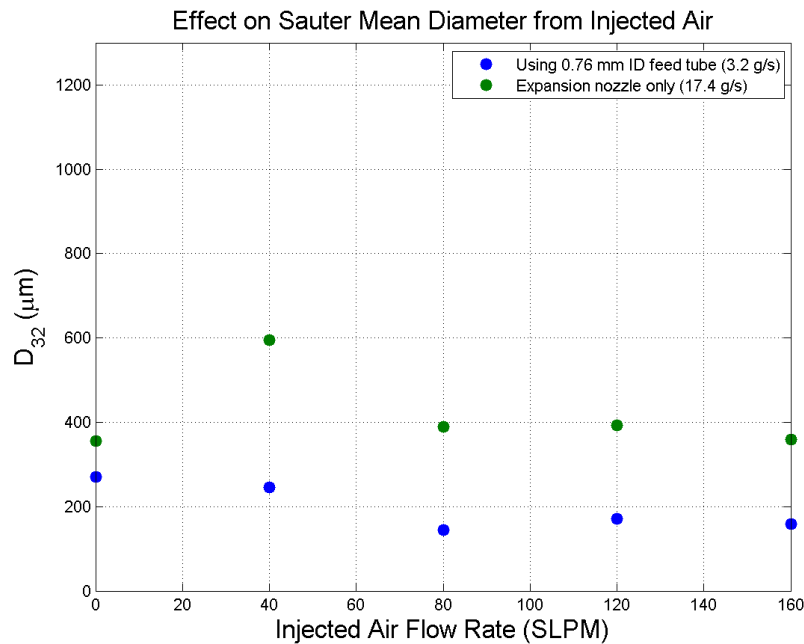
Figure 4.15: Particle statistics: effect of injected air on Sauter mean diameter.
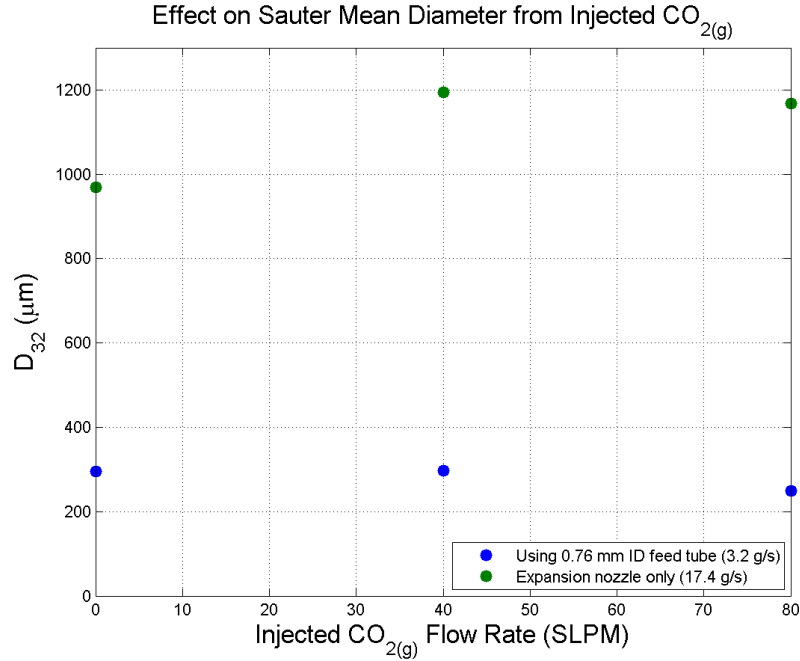
Figure 4.16: Particle statistics: effect of gaseous CO_2 on Sauter mean diameter. Clearly, mixing $CO_{2(g)}$ does not have the same effect on particle size reduction as mixing air.

In Figure 4.15, a reduction in Sauter mean diameter as the injected flow rate of air is increased for a particle generation system using the 0.76 mm (0.03 inch) ID feed tube corresponds to the trend observed with the area-equivalent diameter graph. Likewise, in Figure 4.16, D_{32} trends with the slight reduction in particle diameter as observed with the area-equivalent diameter graph. The D_{32} calculations with the absence of a feed tube do not trend as favorably with the average area-equivalent results, however. A possible explanation is that a few large particles in the images are weighting the measurements towards a higher D_{32}. This observation will be discussed further in the sources of error section.

4.3.2   *Particle Size Control Using Mesh Filters.*

An attempt was made to use three different mesh filters for particle size control as described in Chapter 3. The particle generation system with the 0.76 mm (0.03 inch) feed

tube was utilized as it had the lowest mass flow rate. Even with this configuration, solid CO_2 particles collected on the filters and caused blockage in the PVC pipe extension. The first attempted filter was the 0.127 mm (0.005 inch) wire diameter with mesh openings of 0.76 mm x 0.76 mm (0.03 inch x 0.03 inch). Operation of the particle generation system resulted in the blockage shown in Figure 4.17. This wire mesh was then removed and replaced with a 0.66 mm (0.026 inch) wire diameter stainless steel mesh with openings of 1 mm x 1 mm (0.04 inch x 0.04 inch). The same result occured when the particle generation system was opened. In a final attempt, an elongated mesh of 0.2032 mm (0.008 inch) wire diameter with mesh openings of 4.76 mm x 2.39 mm (0.1875 inch x 0.094 inch) was used in the feasibility experiment. Some particles were filtered through the mesh, but the majority of the particles collected on the screen as shown in Figure 4.18. The results of this experiment were a factor in removing the honeycomb flow straighteners and tunnel screens in the particle sizing analysis experiments at AFRL.
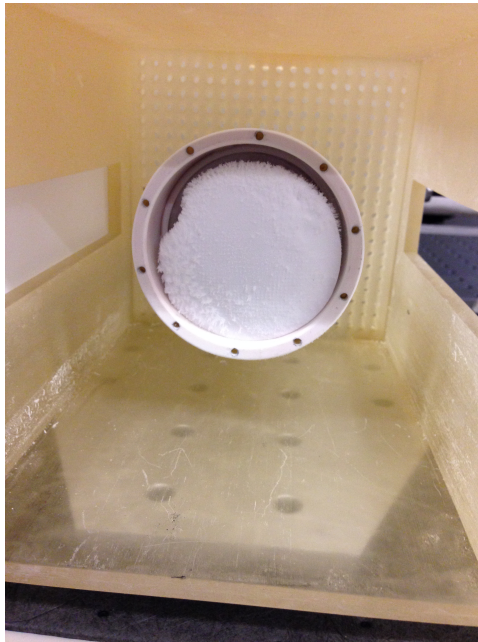
Figure 4.17: Result of feasibility experiment using the 0.76 mm x 0.76 mm (0.03 inch x 0.03 inch) mesh filter
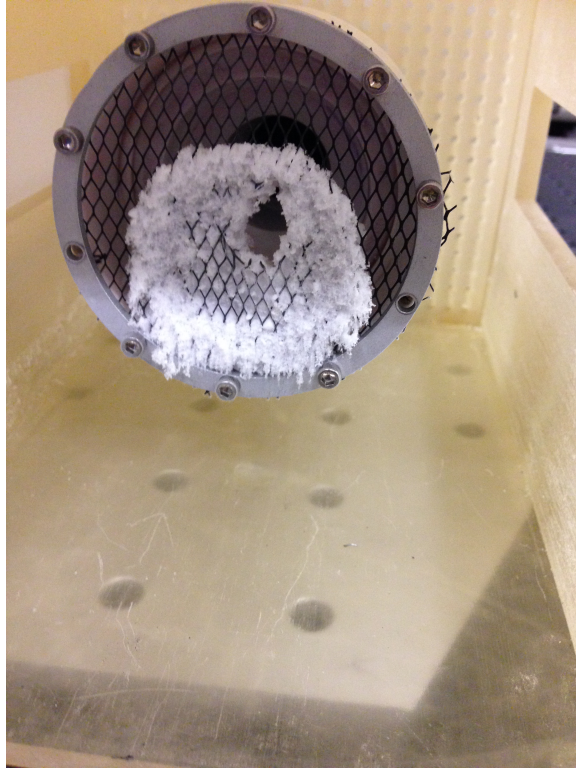
Figure 4.18: Result of feasibility experiment using elongated mesh filter

4.4   Particle Size Analysis at AFRL

A demonstration of particle size control using injected dry air was conducted in the Educational Wind Tunnel at AFRL using the image-based technique. For a description of experimental test runs and test equipment, please see Chapter 3. As with the particle sizing experiments at AFIT, particle size reduced as mass flow rate of dry air increased. Particle size also reduced as the Mach number was increased. In order to see a greater effect, only the results from the experiments conducted at Mach 0.026, Mach 0.08 and Mach 0.13 are presented in the following sections. Figs. 4.19 to 4.21 show the progression of particle size reduction of the aforementioned experiments at both the inlet and test sections of the EWT.
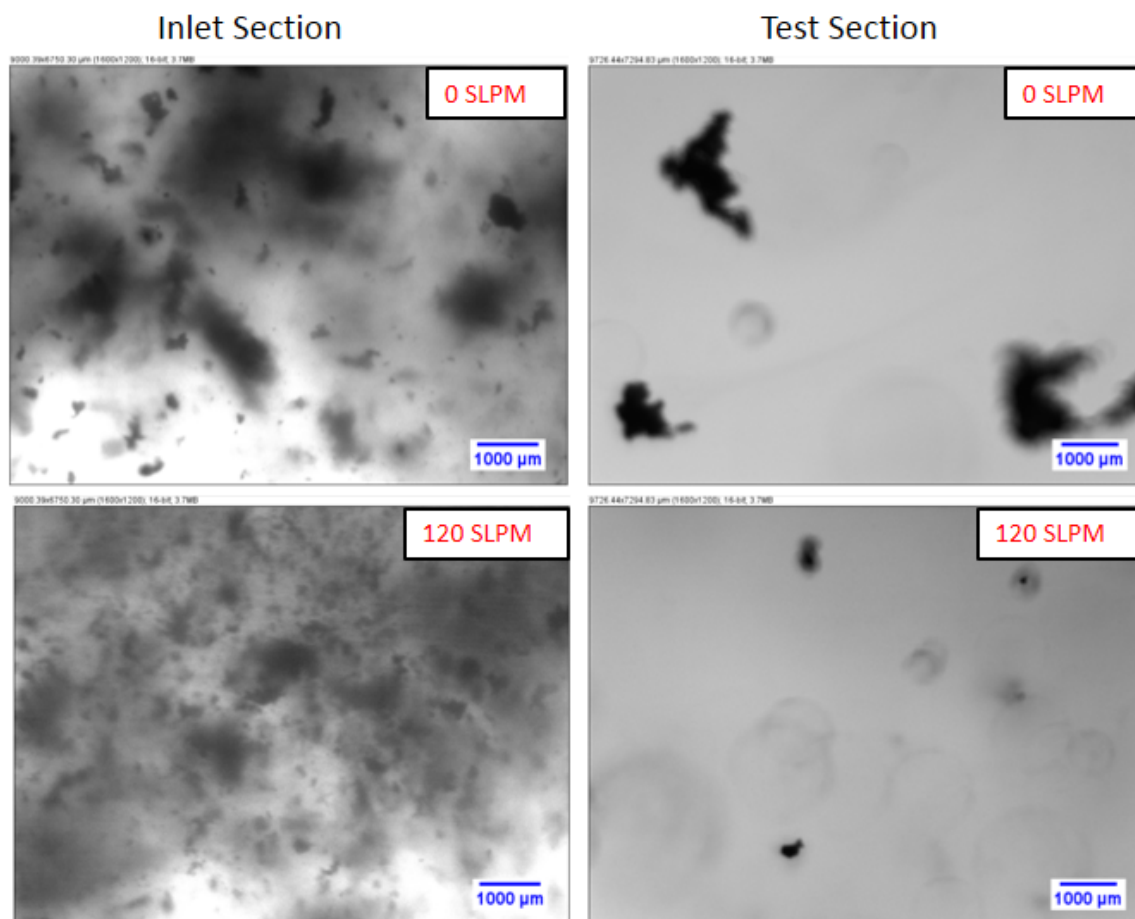
Figure 4.19: Comparison of particle size reduction at inlet and test sections of EWT at Mach 0.026
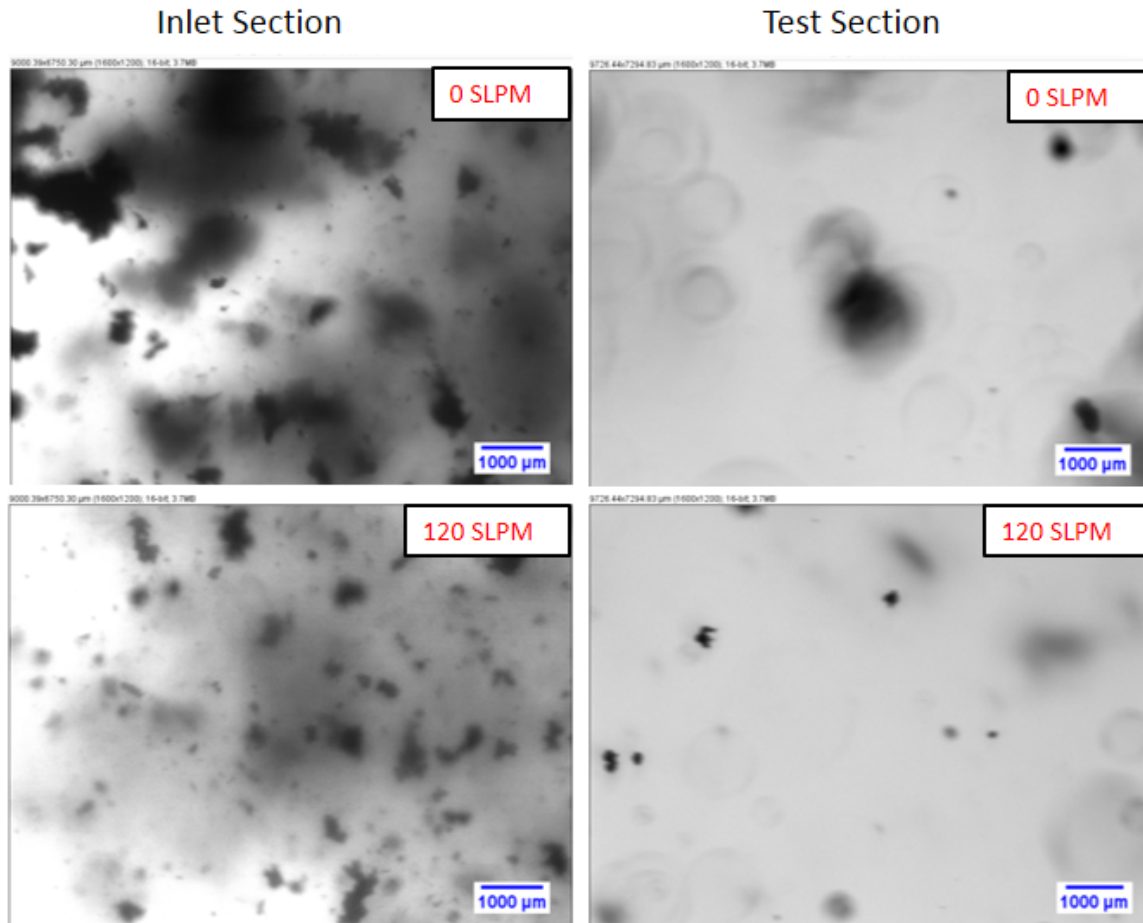
Figure 4.20: Comparison of particle size reduction at inlet and test sections of EWT at Mach 0.08
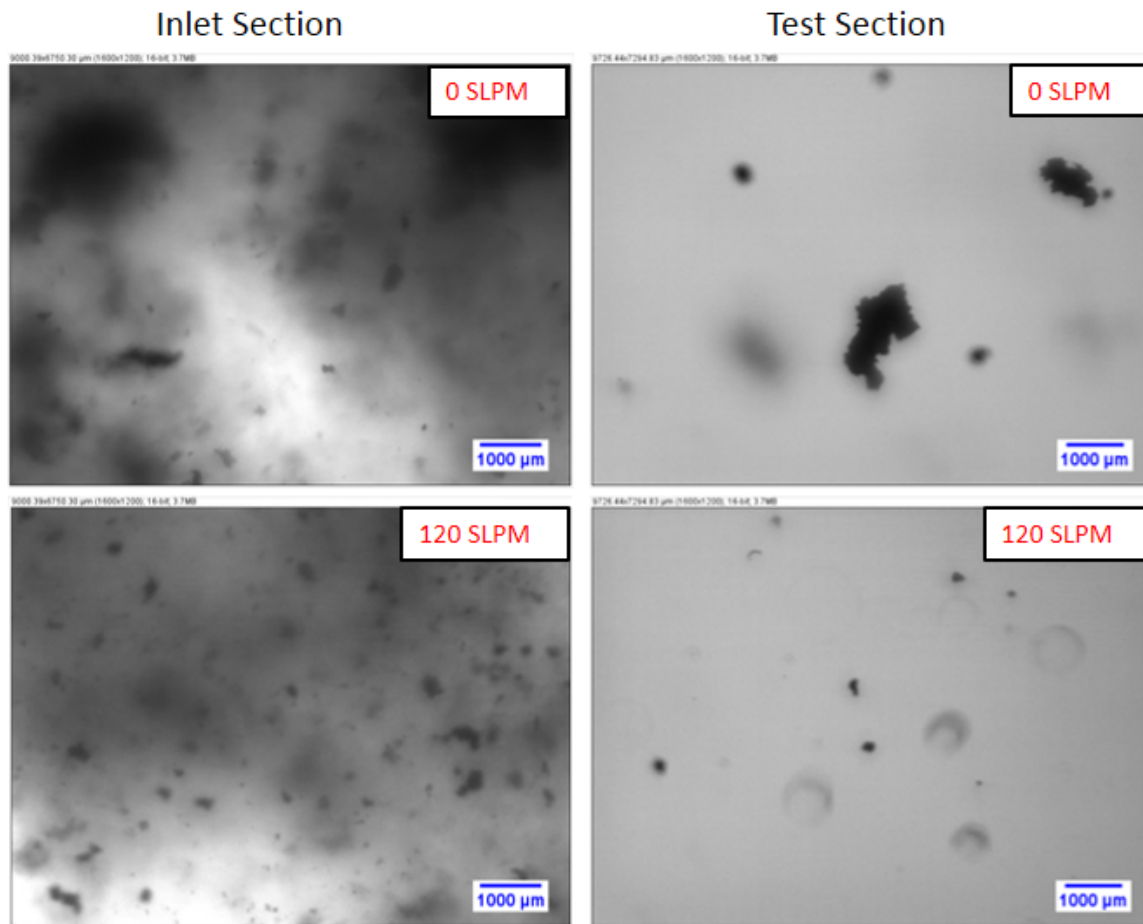
Figure 4.21: Comparison of particle size reduction at inlet and
test sections of EWT at Mach 0.13

As discussed in Chapter 3, the turbulence in the wind tunnel from the removal of the honeycomb flow straighteners and screens made it difficult to acquire dense seeding in the test section. However, it was determined that for sizing data, dense seeding was not as necessary as would be for velocity measurements. The images from the EWT inlet section contain many more CO_2 particles, as the flow has not yet fully spread and entered the turbulent environment of the wind tunnel. Unlike the shadow imaging conducted at AFIT, pictures were taken 0.076 m (3 inches) downstream of the shroud tube exit to better capture discrete particles and and increase amount of light entering the CCD in the camera.

4.4.1   *Particle Size Distributions and Statistics at AFRL.*

4.4.1.1   *Particle Size Distributions for the EWT Inlet Section.*

Particle size distributions are shown for the Mach 0.026, Mach 0.08, and Mach 0.13 test conditions for injected air rates of 0 SLPM, 40 SLPM, 80 SLPM and 120 SLPM in Figs. 4.22 to 4.24. As expected, all three distributions are nearly identical to one another because the images were taken with the same particle generation configuration and at the same distance from the shroud tube exit. As with the experiments conducted at AFIT, the most commonly encountered particle size was between the 40 μm to 80 μm range. However, an increase in the percentage of particles under 80 μm with increased mix air flow rate was not as evident as with the particle sizing experiments shown in Figure 4.9 and Figure 4.11.
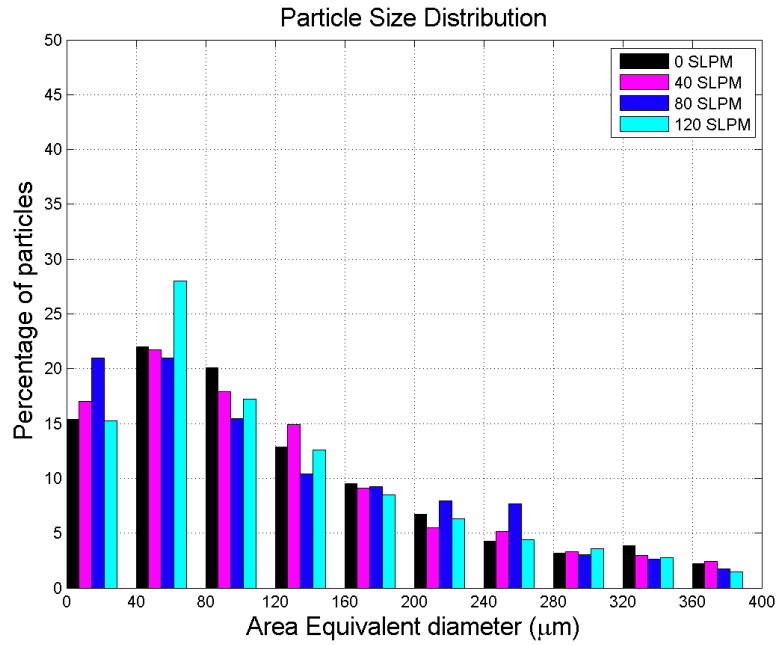
Figure 4.22: Particle size distribution: expansion nozzle only with injected air at Mach 0.026 (Inlet Section)
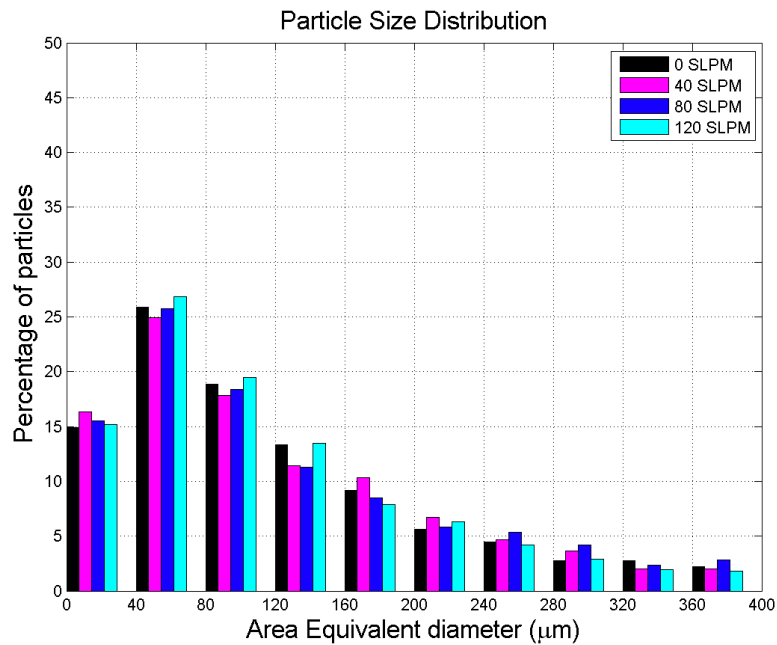
Figure 4.23: Particle size distribution: expansion nozzle only with injected air at Mach 0.08 (Inlet Section)
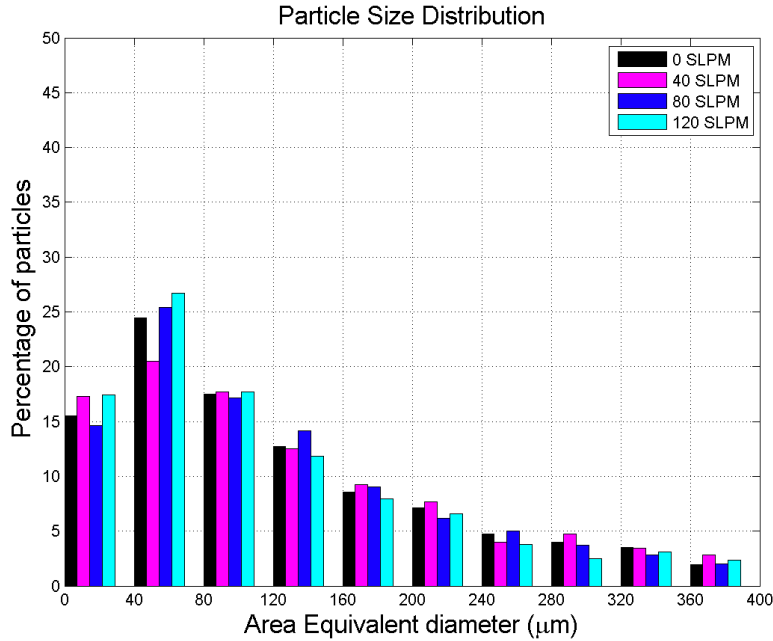
Figure 4.24: Particle size distribution: expansion nozzle only with injected air at Mach 0.13 (Inlet Section)

4.4.1.2 *Particle Size Distributions for the EWT Test Section.*

The particle size distributions for the EWT test section showed greater variability in area-equivalent particle diameter. Nonetheless, all three showed a distinct shift towards smaller particles when compared to the inlet section particle size distributions. Here, the most frequently encountered particle was within the 13 to 40 μm range. In Figure 4.25 and Figure 4.26, corresponding to Mach 0.026 and Mach 0.08, a noticeable spike with no mix air shows many more particles in the 13 to 40 μm range than if dry air was injected. A possible explanation for this trend is that the initial particles exiting the shroud tube without mixing air are larger than the particles injected with mixing air. Therefore, they persist longer downstream into the test section, while the smaller particles generated by the mixing air have already sublimated. In Figure 4.27, corresponding to Mach 0.13, a more random distribution of particle diameter is observed for all cases of injected air. Tunnel flow was the most turbulent at this speed, resulting in the lowest sampling size for the solid

99

carbon dioxide particles. For this particular test, a maximum mass flow rate of 100 SLPM could only be obtained, therefore the data range is only plotted from 0 SLPM to 80 SLPM.
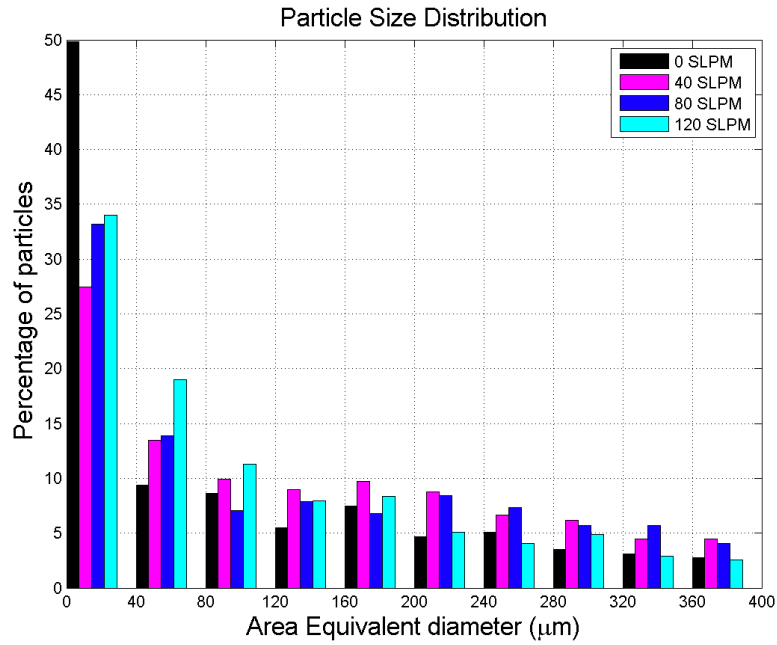
Figure 4.25: Particles size distribution: expansion nozzle only with injected air at Mach 0.026 (Test Section)
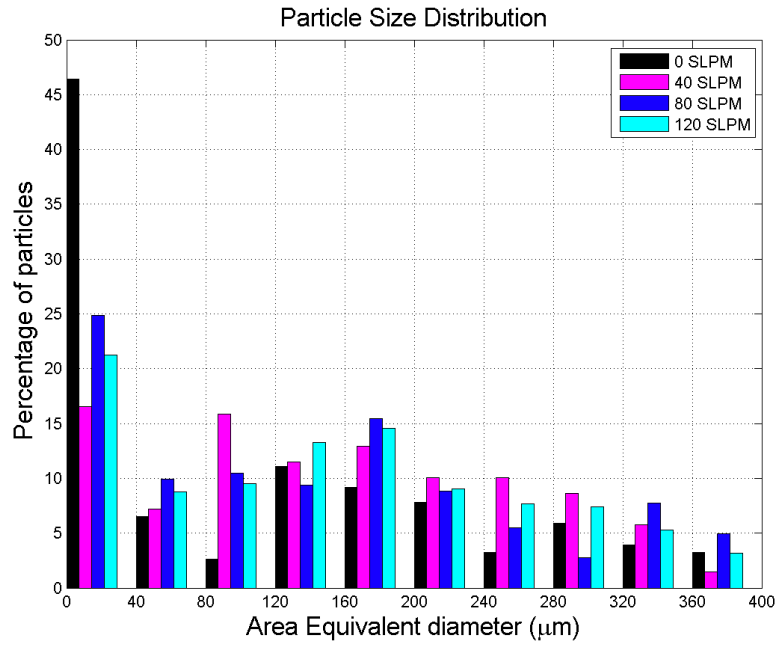
Figure 4.26: Particle size distribution: expansion nozzle only with injected air at Mach 0.08 (Test Section)
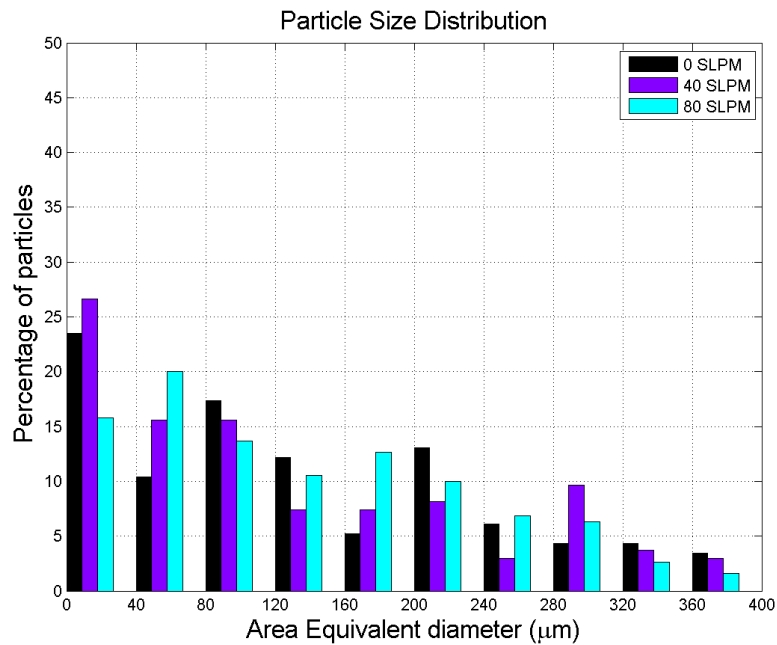
Figure 4.27: Particle size distribution: expansion nozzle only with injected air at Mach 0.13 (Test Section)

4.4.2 Comparison Between Average Area-Equivalent Particle Diameter at Tunnel Inlet and Test Section.

Figure 4.28 and Figure 4.29 clearly show a decrease in average area-equivalent particle size as the mass flow rate of injected air is increased. A much larger decrease in area-equivalent diameter was witnessed than with the particle sizing experiments at AFIT. For Mach 0.026 and Mach 0.08, average area-equivalent diameter decreased approximately by a factor of 1.65 in the test section and 1.46 in the inlet section from 40 SLPM to 120 SLPM of injected air. An unexpected trend is that the average particle diameter is higher in the test section than at the inlet section.

Figure 4.28: Particle statistics: average area-equivalent diameter comparison between inlet and test sections for Mach 0.026
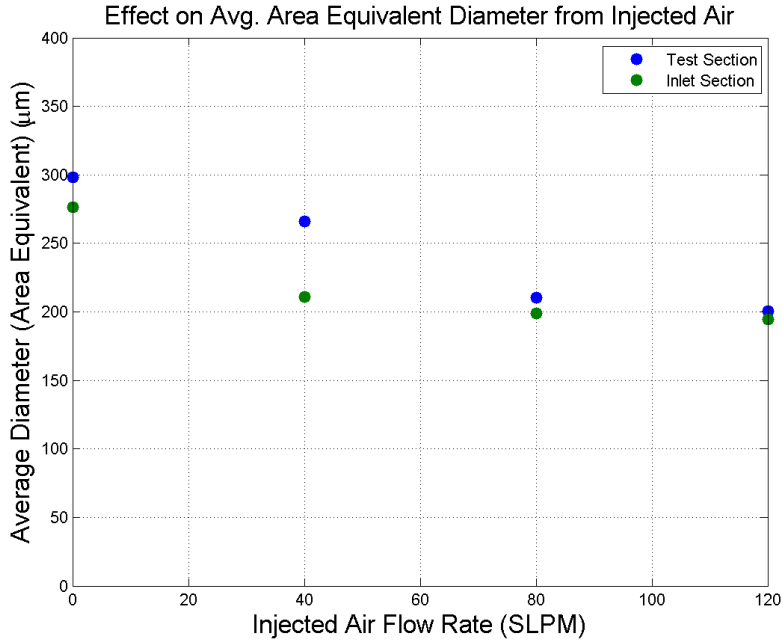
Figure 4.29: Particle statistics: average area-equivalent diameter comparison between inlet and test sections for Mach 0.08

When comparing some of the raw images between the inlet section and test sections, the inlet particles typically appear to be smaller than the particles in the test section. By the time they reach the test section, many smaller particles have sublimated, leaving a greater ratio of larger to smaller particles than in the inlet section. This presumption is best illustrated by Figs. 4.30 to 4.31 for the case using 120 SLPM of injected air. Over 90% of the particle distribution is under 250 μm for the inlet section compared to about 83-88% for the particle distribution in the test section.
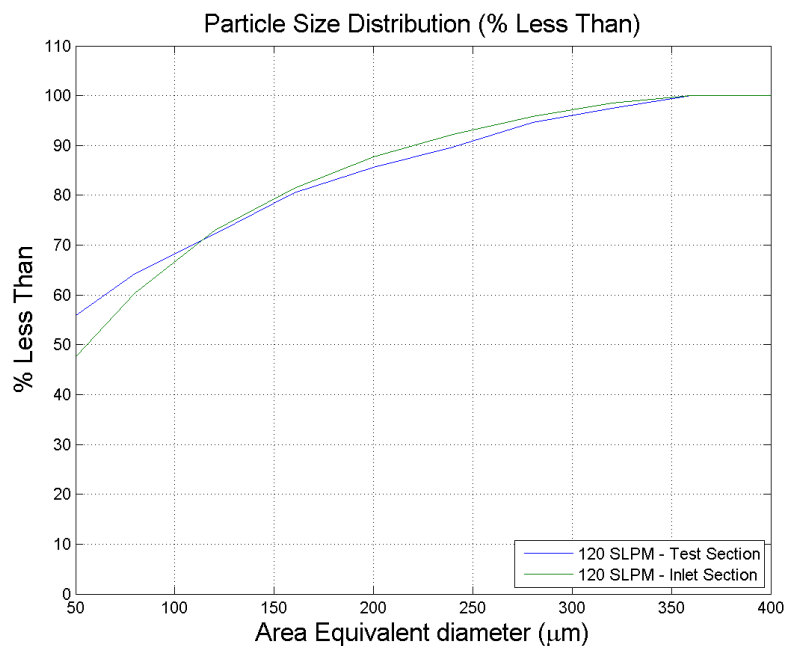
Figure 4.30: Particle statistics: percent less than comparison between inlet and test sections for Mach 0.026
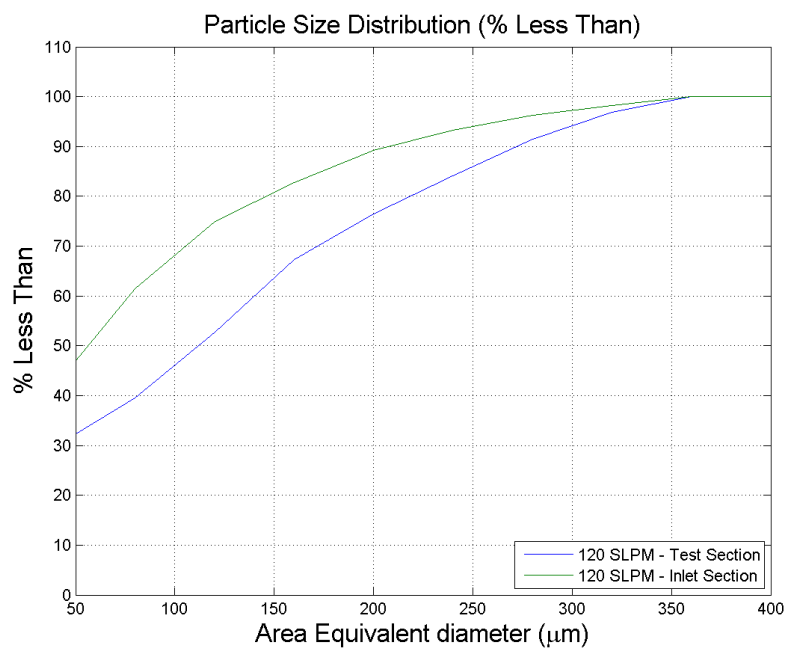
Figure 4.31: Particle statistics: percent less than comparison between inlet and test sections for Mach 0.08

104

The experiments conducted at Mach 0.13 draw a different conclusion in Figure 4.32, as average area-equivalent diameter does not significantly decrease with increased injected air. Average particle diameter is also smaller in the test section than in the inlet section. Once again, this may have been due to the limited sample size. Table 4.4, Table 4.5, and Table 4.6 show the total number of particles in each particle distribution at the inlet section and test section for a comparison of the sample size for each experimental case.
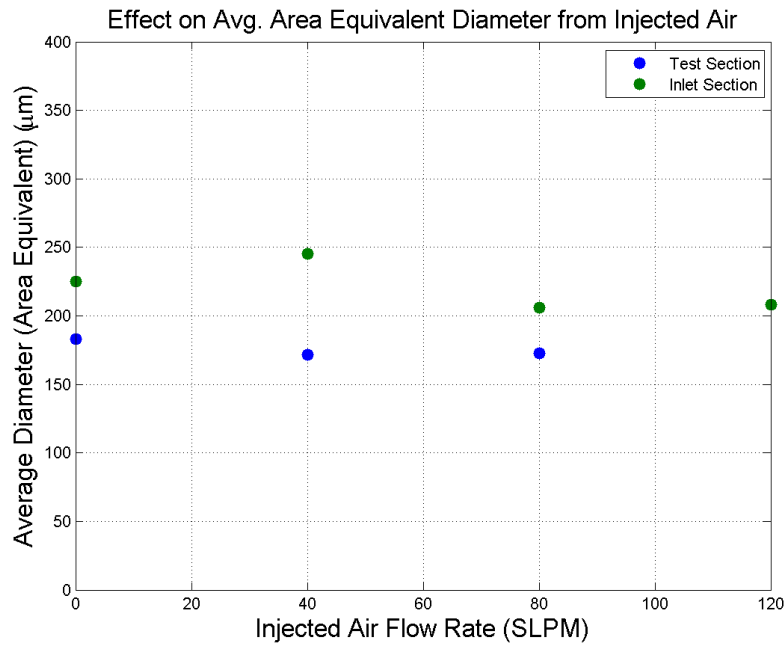
Figure 4.32: Particle statistics: average area-equivalent diameter comparison between inlet and test sections for Mach 0.13
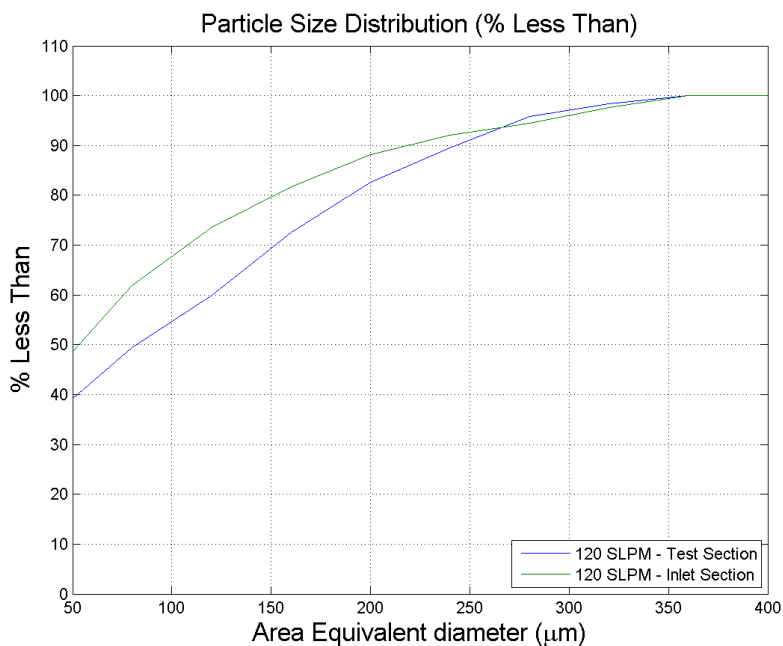
Figure 4.33: Particle statistics: percent less than comparison between inlet and test sections for Mach 0.13

Table 4.4: Sample Sizes for Mach 0.026

Experiment	Total # of particles	
	Inlet Section	*Test Section*
0 SLPM	2318	326
40 SLPM	1486	523
80 SLPM	771	439
120 SLPM	1291	563

Table 4.5: Sample Sizes for Mach 0.08

Experiment	Total # of particles	
	Inlet Section	*Test Section*
0 SLPM	2483	195
40 SLPM	2202	165
80 SLPM	2105	198
120 SLPM	2475	409

Table 4.6: Sample Sizes for Mach 0.13

Experiment	Total # of particles	
	Inlet Section	*Test Section*
0 SLPM	2071	124
40 SLPM	1095	146
80 SLPM	1667	201

4.4.3 Comparison Between Sauter Mean Diameter at Tunnel Inlet and Test Section.

In Figs. 4.34 to 4.36, there is a downward trend in D_{32} consistent with the average area-equivalent graphs. However, D_{32} size for the inlet section is larger than the test section, a reversal from the average area-equivalent graphs. Since the magnitude of D_{32} is strongly influenced by larger particles in the distribution, if the inlet section contained more smaller particles then the distribution would be shifted towards the larger particles.
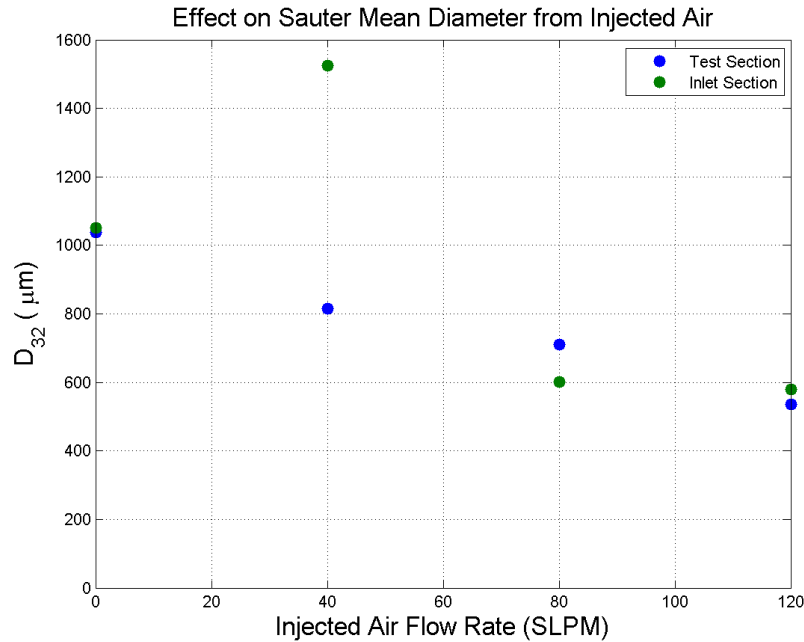
Figure 4.34: Particle statistics: Sauter mean diameter comparison between inlet and test sections for Mach 0.026
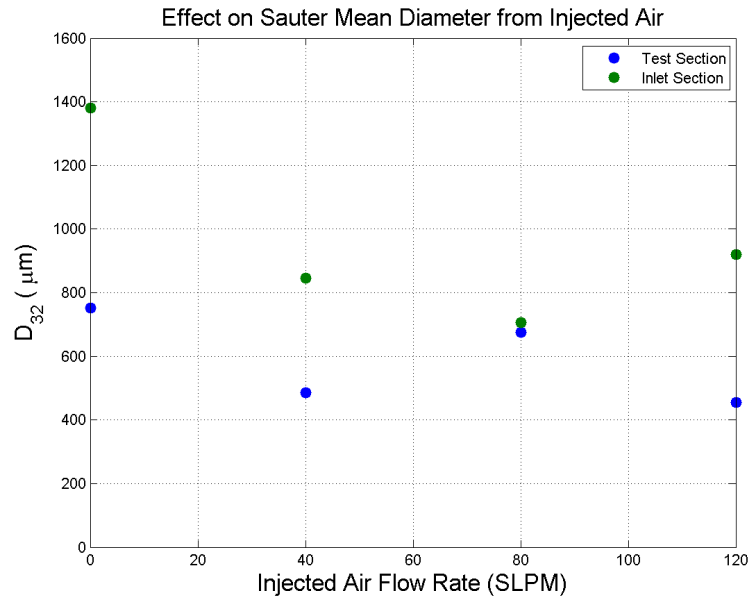
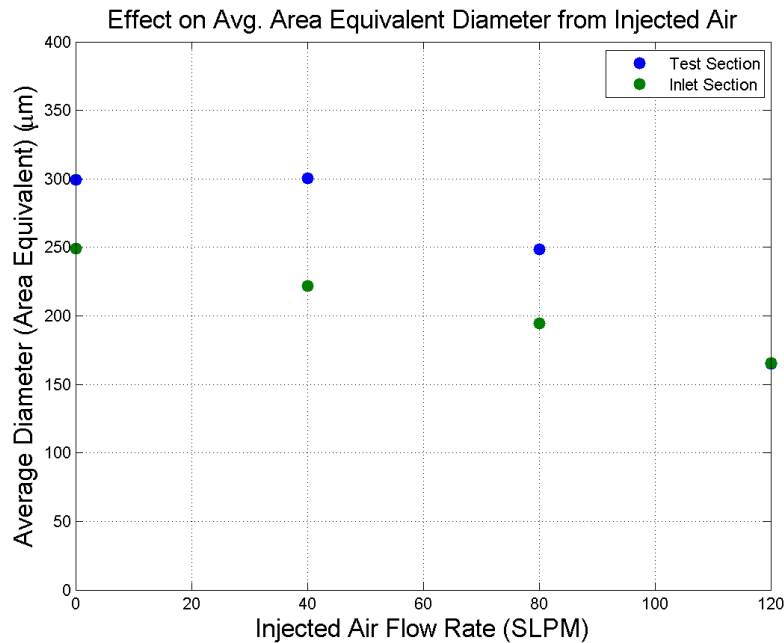**Figure 4.35:** Particle statistics: Sauter mean diameter comparison between inlet and test sections for Mach 0.08
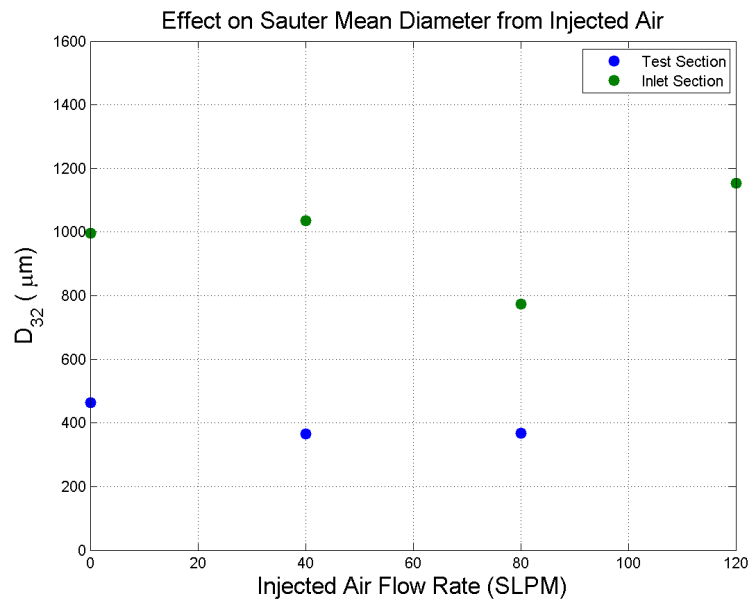
Figure 4.36: Particle statistics: Sauter mean diameter comparison between inlet and test sections for Mach 0.13

4.4.4 Sublimation Rate of CO_2 Particles.

Theoretical and experimental sublimation rates of the particles were calculated using the wind tunnel data at the Mach 0.026, Mach 0.08 and Mach 0.13 conditions. The theoretical sublimation rates were calculated using Equation (2.14). The constants and expressions used in the equation are summarized in Table 4.7. Although density and temperature measurements of the solid CO_2 particles were not measured experimentally, assumptions were made based on the material data properties in Reference [32]. The experimental sublimation rates were calculated by taking the difference between average "bulk" particle diameters in the inlet and test sections, then dividing by the time difference. The average "bulk" particle diameter was defined as the average diameter of the particles in the 10 μm to 80 μm range for each distribution. The time difference was calculated by dividing the distance between the shroud tube exit and the test section FOV (measured at 1.14 m) by the wind tunnel air speed.

Table 4.7: Constants and expressions used in the sublimation rate equation

Symbol	Definition	Expression or constant value
k_a	Thermal conductivity of air (W m^{-2} $°C^{-1}$)	$2.43 \times 10^{-2} + 7.3 \times 10^{-4}(T_a)$
Nu	Ratio of convective to conductive heat transfer normal to a surface	$2 + 0.6Re_p^{1/2}Pr^{1/3}$
ρ_c	Density of the particle (kg/m^3)	1500
L_{sd}	Specific latent heat of sublimation of dry ice (Jkg^{-1})	5.74×10^5
T_s	Temperature of the particle (°C)	-78.5
T_a	Temperature of the air (°C)	Ranged from 15 to 18

Summaries of the experimental conditions for each Mach number are shown in Table 4.8, Table 4.9 and Table 4.10, including the mean sublimation rate. The data clearly shows that the predicted sublimation rates are much higher than the measured sublimation

rates. For the Mach 0.026 case, predicted sublimation rates differ from the measured rates by as much as a factor of 12. In Reference [20], the predicted sublimation rates were within 10-20% of the experimental observations for warm, dry air wind tunnel conditions. The largest factor for the discrepancy between the accuracy of the predicted results in this research and the accuracy of the predicted results in Reference [20] is unquestionably due to the assumption that the particles are not moving with the fluid. Calculation of the predicted values assumed stationary CO_2 particles as wind tunnel air speed was increased. This was not the case in the EWT experiments, where the particles were injected into a moving flow. The EWT experimental mean sublimation rate results do support a conclusion that there is an effect on the Nusselt number (and therefore the particle sublimation rate) as wind tunnel speed is increased. However, it is difficult to quantify exactly how much the increase in speed contributed to the sublimation rate. There was a difference between the initial velocity of the particles and the wind tunnel speed, but the predicted sublimation rates were calculated using the wind tunnel speed as the difference. Consequently, the predicted sublimation rates are assumed to be a worst case sublimation rate for the EWT experiments.

In Table 4.8, the measured sublimation rates and the predicted sublimation rate both appear to decrease with increase in the mass flow rate of injected air. In Table 4.9, the predicted sublimation rate decreases with the increase in the mass flow rate of injected air, but the measured sublimation rate does not. From Equation (2.14), an increase in initial diameter of the particles should decrease the sublimation rate if all other parameters remain constant. It is difficult to observe trends in the sublimation rates for Mach 0.13 data because the average bulk initial diameters were approximately the same even when the mass flow rate of the injected air was increased. This was again attributed to the low sampling of particles at this condition.

Table 4.8: Summary of experimental conditions at Mach 0.026

Mass flow rate of injected air (SLPM)	Ambient Temperature (°C)	Average bulk D_i at inlet (μm)	Average bulk D_f at test section (μm)	Mean sublimation rate	
				Measured (μm s^{-1})	Predicted (μm s^{-1})
0	17	36.65	24.31	96.8	923
40	14	38.29	28.28	78.5	828
80	15	38.66	29.5	71.77	844
120	15	39.99	31.4	67.4	823

Table 4.9: Summary of experimental conditions at Mach 0.08

Mass flow rate of injected air (SLPM)	Ambient Temperature (°C)	Average bulk D_i at inlet (μm)	Average bulk D_f at test section (μm)	Mean sublimation rate	
				Measured (μm s^{-1})	Predicted (μm s^{-1})
0	17	41.43	30.49	257.3	1173
40	17	42.08	30.63	269.35	1161
80	17	42.67	30.54	285.53	1150
120	17	43.3	30.5	301.2	1139

Table 4.10: Summary of experimental conditions at Mach 0.13

Mass flow rate of injected air (SLPM)	Ambient Temperature (°C)	Average bulk D_i at inlet (μm)	Average bulk D_f at test section (μm)	Mean sublimation rate	
				Measured (μm s^{-1})	Predicted (μm s^{-1})
0	17	43.59	30.47	514.5	1355
40	18	43.58	30.68	505.8	1387
80	18	43.85	31.41	488.15	1382
120	18	43.92	N/A	N/A	1380

4.4.5 Sources of Error with Image Processing.

Some difficulties arose with obtaining good quality particle sizing information from certain experiments. For instance, in the bench test experiments conducted at AFIT, particle production was particularly dense for the experiments without the addition of a feed tube. This made processing extremely difficult with the imaging software, as particles could not be distinguished from the gaseous carbon dioxide. An example of a raw and resulting processed image is given in Figure 4.37 to demonstrate the limitations for accurate particle sizing.

For all experiments, variations due to non-uniform lighting (image contrast), differentiation between the particles in focus and background, and transparency of the particles for each image for each case tended to bias the sizing measurements toward larger pixel values and larger particles. The software also had difficulty separating particles in focus versus particles in the rear of the depth of field. This issue is demonstrated in Figure 4.38 for the AFIT experiment using injected dry air with no feed tube. Nevertheless, since each image for this particular experiment was processed using the same methodology, comparative information for each case can be ascertained even if the true particle sizing information contains error.
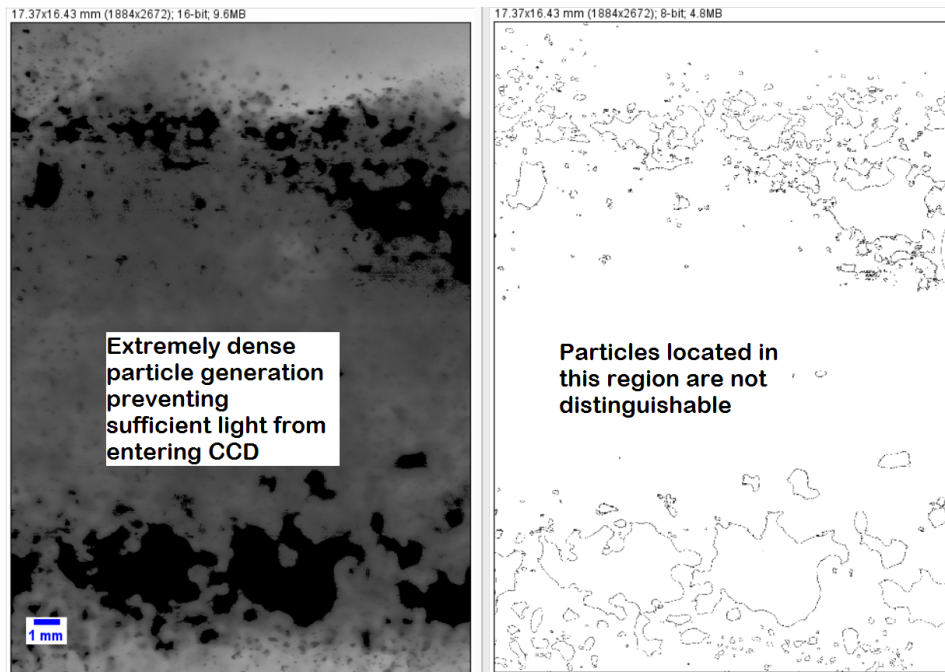
Figure 4.37: Example raw and resulting processed image using injected $CO_{2(g)}$ with no feed tube
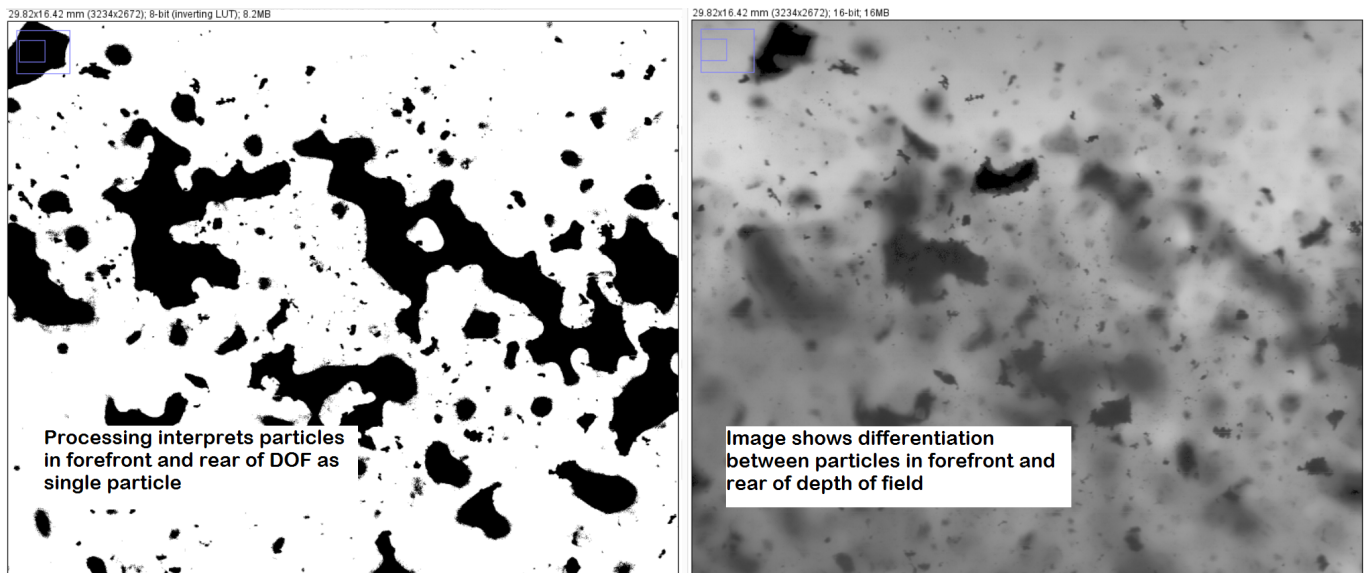
Figure 4.38: Comparison of raw image and processed image using ImageJ for AFIT experiment #1 (expansion nozzle only with injected air)

V.   Conclusions

5.1   Overview of Research Effort

In essence, the research effort had two approaches to improve clean seeding for PIV. One approach was to utilize the non-ideal particles produced from the boundary layer measurement testing and improve flow tracking accuracy with respect to another experimental method. The second approach was to improve the particle size distribution through intelligent injector design with more consideration for particle size in the test section rather than at the injector exit.

Data from previous research using solid carbon dioxide as a seeding material for particle image velocimetry was analyzed and processed using carefully chosen parameters. The analyzed data included 10,000 image pairs of turbulent boundary layer measurements in the AFRL Trisonic Gasdynamics Facility. Processing techniques to improve fidelity with other experimental techniques were implemented, such as noise reduction, multi-pass iterations, reduction of invalid vectors, improved correlation coefficient and the use of a calibration method to reduce image disparity in stereoscopic PIV. A particle tracking capability based on previous PIV results was used to generate velocity data. New boundary layer profiles were created and compared with the previous velocity profile.

The challenges of producing right-sized, discrete solid carbon dioxide particles for acceptable flow tracking in a variety of flow conditions have been addressed. New experimental techniques were utilized to control and measure particle diameter and compared with data from previous experimental techniques. Particle size was controlled via the injection of dry air or gaseous carbon dioxide. Particle concentration was controlled by restricting the mass flow rate of the liquid carbon dioxide prior to its phase change into solid particles. Particle diameters were measured using a modified particle shadow velocimetry

114

technique that allowed for sizing measurements. The images captured from the shadow imaging were collected and processed using the ImageJ particle sizing analysis software. Particle distributions and statistics were created from the resulting data and analyzed.

5.2 Conclusions

After refined processing of the stereoscopic PIV images, the boundary layer profile trended with the Pitot probe data. A new boundary layer thickness was calculated and the maximum deviation was determined to be approximately 2.5 % with Pitot probe data. The previous boundary layer thickness was more than double the thickness of the Pitot probe boundary layer thickness. Free stream velocity measurements from the re-processed data were within 0.97 % of wind tunnel free stream calculations.

The results of the particle sizing and control experiments conducted at AFIT and AFRL confirmed the expected trends of particle size reduction and decreased CO_2 concentration with the increase in mass flow rate of mixing air or gaseous CO_2. In the particle sizing experiments conducted at AFIT, injecting dry air normal to the CO_2 flow had a much more substantial effect in reducing average area-equivalent particle diameter than injecting gaseous carbon dioxide. The greatest effect was produced when dry air was injected into the reduced CO_2 mass flow configuration (0.76 mm ID feed tube) in conjunction with the expansion nozzle and shroud tube, where a 21% decrease in average area-equivalent diameter was observed. In contrast, only about an 8% decrease in in average area-equivalent diameter was observed using the same particle generation configuration with injected gaseous carbon dioxide. Particle diameters below 80 μm were the most frequently produced using either a 0.76 mm (0.03 inch) ID feed tube in conjunction with a 0.864 mm (0.034 inch) ID expansion nozzle and 20.9 mm (0.824 inch) ID shroud tube or with a 0.864 mm (0.034 inch) ID expansion nozzle and 20.9 mm (0.824 inch) ID shroud tube alone. Particle size was determined to be large compared to previous

particle sizing experiments at AFIT. However, this was expected due to a different particle generation configuration (a larger ID shroud tube) and a new experimental technique with resolution that ranged from 5.63 μm/pixel to 9.26 μm/pixel. Particle sizing experiments conducted in the Educational Wind Tunnel demonstrated the ability to influence particle size in the test section with the addition of injected air into the shroud tube. Shadow images were first taken in the test section of the EWT and then at the inlet for a comparison of the particle size distribution at each location at Mach 0.026, Mach 0.08, and Mach 0.13. A shift in the particle size distributions between the inlet and test sections showed that the most frequently encountered particle in the inlet section was in the 40-80 μm range and below 40 μm in the test section for all experiments. However, average area-equivalent particle diameter was determined to be higher than the average particle diameter in the inlet section. The conclusion was made that by the time the particles reach the test section, the smaller ones have already sublimated. This increases the ratio of larger to smaller particles and translates into a higher average particle diameter.

5.3   Impact of Research

An image-based experimental method for measuring CO_2 particle size and potentially velocity measurements was set up and used successfully at AFIT. Particle diameter measurements can be compared with images to gain not only quantitative but qualitative information about the particle size distribution and the effects of varying different mechanisms of particle control. An important part of this method was the successful implementation of image processing (ImageJ) software to measure particle diameters. The software has the potential for greater accuracy if experimental factors, such as increased back lighting and optical zoom for sizing smaller particles, are improved.

New image processing methods produced better quality vector maps for future PIV work in the TGF, particularly stereoscopic PIV. The new methods improved signal-to-noise,

reduced false vectors and improved reliability in the vector maps. A new calibration method for stereo PIV will enable future researchers in developing maps with increased velocity measurement accuracies and stronger correlation between particle images.

5.4   Future Work

It was observed during this research that the key to generating discrete, small particles was by controlling the mass flow rate of the liquid CO_2 prior to entry into the shroud tube. Mass flow rate control was accomplished via various sizes of feed tube, however, issues arose when the tubes clogged during experimental runs. A different flow control mechanism is recommended for future work with particle generation, although it must be suitable for cryogenic temperatures.

Successful image processing of the particles was highly dependent upon background variations and light transparency through the particles. To improve particle distinction from noise, a monochromatic, collimated light source such as a RGB LED lamp is recommended for all future particle shadow imaging. Small field of views with narrow depth of fields are recommended for even higher resolution of the particles down to the 1 μm size.

It is suggested that particle sizing experiments using shadow imaging should be conducted in a full-scale wind tunnel such as the AFRL TGF or one of the AFIT tunnels with a flow straightener in place. Particle sizing data at multiple locations downstream of the CO_2 injector(s) could be used to determine sublimation rates with higher confidence than the rates calculated in this research.

Appendix A: Wind Tunnel Instrumentation Data for Refined Turbulent Boundary Layer Measurements

	P0PSF	PSPSF	T0	MACH_STD	Q_STD	Velocity_STD	Velocity_STD	Re	Re/ft	TS_STD	TS_STD	Rho
	PSFA	PSFA	°R		PSF	ft/sec	m/sec			°R	°K	
	1043.42	881.05	529.75	0.498	152.69	547.77	166.960296	3E+06	396404	504.76	280.4222	0.032723
	1044.62	881.87	529.8	0.498	153.04	548.14	167.073072	3E+06	397016	504.79	280.4389	0.032752
	1044.39	876.34	534.15	0.507	157.66	559.92	170.663616	3E+06	398394	508.06	282.2556	0.032338
	1045.73	870.94	533.46	0.518	163.53	571.02	174.046896	3E+06	406292	506.29	281.2722	0.03225
AVERAGE	1044.54	877.55	531.79	0.50525	156.73	556.7125	169.68597	3E+06	399526.5	505.975	281.0972	0.032516

GAMMA	1.4	
R	287	J/kgK

Figure A.1: TGF instrumentation data (13 September 2011)

Appendix B: Test Point Matrices for AFIT Particle Size Analysis Experiments

$\dot{m}$ of mixing air (SLPM)	$\dot{m}$ of surrounding air (SLPM)	Test time (s)	Pulse Δ t (ms)	Pulse duration (μs)	# of Images Processed	W_i CO$_2$ dewar (kg)	W_f CO$_2$ dewar (kg)	$\dot{M}$ (g/s)	Calculated Velocity (cm/s)	Temp (°C)	RH (%)
Air Test Point Matrix (atomizer nozzle only)											
Distance from tube (at nozzle exit)											
0	60	20	500	20	11					22	20
10	60	25	500	20						22	20
20	60	30	500	20						21	16
30	60	29	500	20						21	16
40	60	42	500	20	20	316.2	315.7	11.90	126.85	19	16
50	60	30	500	20		315.7	315.3	13.33	142.07	19	16
60	60	29	500	20		315.3	314.8	17.24	183.71	20	22
70	60	28	500	20		314.8	314.3	17.85	190.27	20	20
80	60	28	500	20	16	314.3	313.7	21.42	228.33	19	20
90	60	30	500	20		313.7	313.2	16.66	177.59	19	20
100	60	29	500	20		313.2	312.5	24.13	257.20	19	20
110	60	37	500	20		312.5	311.9	16.21	172.79	19	22
120	60	29	500	20	17	311.9	311.4	17.24	183.71	19	22
130	60	40	500	20		311.4	310.7	17.5	186.47	19	22
140	60	29	500	20		310.7	310.2	17.24	183.71	20	22
150	60	33	500	20		310.2	309.7	15.15	161.44	20	22
160	60	30	500	20	18	309.7	309.1	20	213.11	20	20
Average			500	20				**17.37**	**185.17**	**19.88**	**19.76**

Table B.1: Air Test Point Matrix (atomizer nozzle only)

						Air Test Point Matrix (with 1.4 mm feed tube)				
						Distance from tube (at nozzle exit)				
$\dot{m}$ of mixing air (SLPM)	$\dot{m}$ of surrounding air (SLPM)	Test time (s)	Pulse Δ t (ms)	Pulse duration (μs)	# of Images Processed	W_i CO_2 dewar (kg)	W_f CO_2 dewar (kg)	$\dot{M}$ (g/s)	Temp (°C)	RH (%)
0	60	27	500	20	13	293.6	293.3	11.11	21	20
10	60	30.16	500	20		293.3	293	9.94	20	16
20	60	33.71	500	20		293	292.7	8.89	19	16
30	60	35	500	20		292.7	292.3	11.42	19	16
40	60	32.4	500	20	19	292.3	292	9.25	19	20
50	60	33.65	500	20		292	291.6	11.88	19	20
60	60	31.38	500	20		291.6	291.3	9.56	19	20
70	60	28.83	500	20		291.3	291	10.40	19	22
80	60	31.7	500	20	16	291	290.6	12.61	20	22
90	60	30	500	20		290.6	290.3	10	20	20
100	60	29.13	500	20		290.3	289.7	20.59	19	20
110	60	30.38	500	20		289.7	289.4	9.87	21	16
120	60	32.35	500	20	19	289.4	289	12.36	21	16
130	60	31.45	500	20		289	288.6	12.71	21	16
140	60	36.65	500	20		288.6	288.3	8.18	21	16
150	60	33	500	20		288.3	287.9	12.12	21	16
160	60	31.48	500	20	17	287.9	287.6	9.52	21	16
170	60	31.06	500	20		287.6	287.3	9.65	21	16
Average								11.12		

Table B.2: Air Test Point Matrix (with 1.4 mm feed tube)

						W_i	W_f			
						CO_2	CO_2			
$\dot{m}$	$\dot{m}$			Pulse	# of	dewar	dewar		Temp	
of mixing air	of	Test time	Pulse Δ t	duration	Images	(kg)	(kg)	$\dot{M}$ (g/s)	(°C)	RH (%)
(SLPM)	surrounding	(s)	(ms)	(μs)	Processed					
	air (SLPM)									
0	60	31	500	20	22	271.5	271.4	3.22	21	16
10	60	39.46	500	20	28	271.4	271.2	5.06	20	16
20	60	35	500	20	23	271.2	271	5.71	20	16
30	60	39.96	500	20	26	271	270.9	2.50	20	16
40	60	33.21	500	20	24	270.9	270.7	6.02	20	16
50	60	30.8	500	20	26	270.7	270.3	12.98	19	16
60	60	88	500	20	73	270.3	270.1	2.27	19	16
70	60	76	500	20	53	270.1	269.8	3.94	19	16
80	60	84	500	20	63	269.8	269.6	2.38	19	16
90	60	66	500	20	46	269.6	269.4	3.03	18	16
100	60	66	500	20	47	269.4	269.2	3.03	19	16
110	60	63	500	20	46	269	268.9	1.58	19	16
120	60	57.25	500	20	40	268.9	268.7	3.49	19	16
130	60	91	500	20	66	268.7	268.5	2.19	19	16
140	60	76	500	20	53	268.5	268.3	2.63	19	16
150	60	62	500	20	44	268.3	268.1	3.22	19	16
160	60	60	500	20	42	268.1	267.9	3.33	19	16
170	60	61	500	20	43	267.9	267.7	3.27	19	16
Average			500	20				3.2		

Air Test Point Matrix (with 0.76 mm feed tube)
Distance from tube (at nozzle exit)

Table B.3: Air Test Point Matrix (with 0.76 mm feed tube)

$\dot{m}$ of mixing air (SLPM)	$\dot{m}$ of surrounding air (SLPM)	Test time (s)	Pulse Δ t (ms)	Pulse duration (μs)	# of Images	W_i CO_2 dewar (kg)	W_f CO_2 dewar (kg)	$\dot{M}$ (g/s)	Temp (°C)	RH (%)	Tank Pressure (psi)
0	60	30	500	20	24	264.9	264.5	13.33	21	16	328
10	60	30	500	20	21	264.5	263.9	20	20	16	321
20	60	30	500	20	24	263.9	263.2	23.33	20	16	321
30	60	30	500	20	23	263.2	262.6	20	19	16	320
40	60	31	500	20	25	262.6	261.8	25.80	19	16	320
50	60	30	500	20	23	261.8	260.9	30	18	16	320
60	60	30	500	20	24	260.9	260	30	18	16	320
70	60	30	500	20	24	260	259	33.33	18	16	319
80	60	60	500	20	32	259	257.6	18	17	16	
Average			500	20				**27**			
90											
100											
110											
120											
130			Could not perform experiment due to inadequate supply of gaseous CO2									
140											
150											
160											
170											

Table header: CO_2 **Test Point Matrix (atomizer nozzle only)** — **Distance from tube (at nozzle exit)**

Table B.4: CO_2 Test Point Matrix (atomizer nozzle only)

$\dot{m}$ of mixing air (SLPM)	$\dot{m}$ of surrounding air (SLPM)	Test time (s)	Pulse Δ t (ms)	Pulse duration (μs)	# of Images	W_i CO$_2$ dewar (kg)	W_f CO$_2$ dewar (kg)	$\dot{M}$ (g/s)	Temp (°C)	RH (%)
CO$_2$ Test Point Matrix (with 1.4 mm feed tube)										
Distance from tube (at nozzle exit)										
0	60	38.05	500	20	27	279.5	279.3	5.25	20	16
10	60	38.36	500	20	31	279.3	278.9	10.42	20	16
20	60	31.05	500	20	22	278.9	278.5	12.88	20	16
30	60	33.7	500	20	26	278.5	278.1	11.86	19	16
40	60	32.73	500	20	25	278.1	277.6	15.27	19	16
50	60	35.31	500	20	26	277.6	277.1	14.16	18	16
60	60	35.26	500	20	27	277.1	276.4	19.85	18	16
70	60	35.9	500	20	27	276.4	275.8	16.713	18	16
80	60	40	500	20	28	275.8	275.1	17.5	18	16
90	60	36.06	500	20	27	275.1	274.2	24.95	18	16
Average			**500**	**20**				**16**		
100										
110										
120										
130										
140										
150				supply of CO2 gas inadequate for mass flow rate						
160										
170										

Table B.5: CO$_2$ Test Point Matrix (with 1.4 mm feed tube)

Appendix C: Particle Size Distributions and Statistics for injector utilizing 1.4 mm feed tube
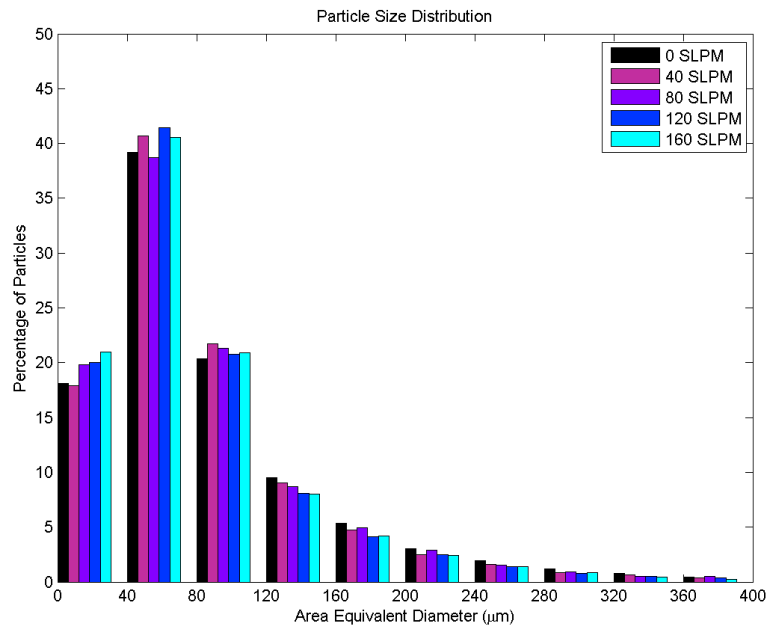

Figure C.1: Particle size distribution: with 1.4 mm feed tube with injected air
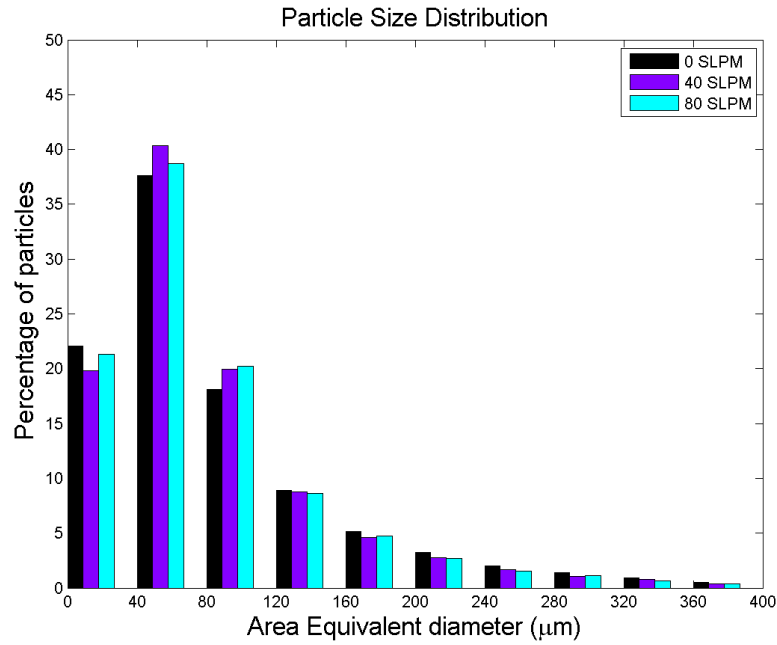
Figure C.2: Particle size distribution: with 1.4 mm feed tube with injected gaseous carbon dioxide
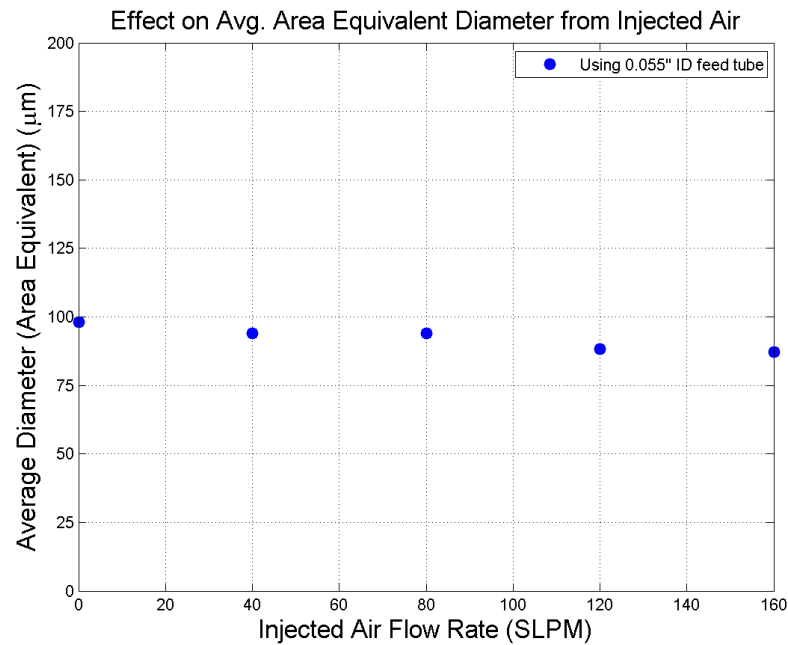

Figure C.3: Particle statistics: effect of injected air on average area-equivalent diameter
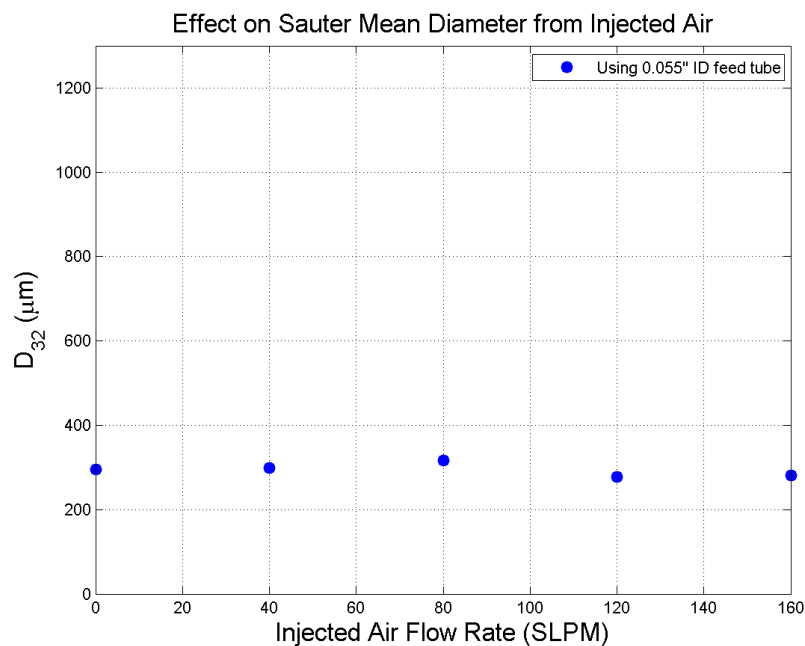
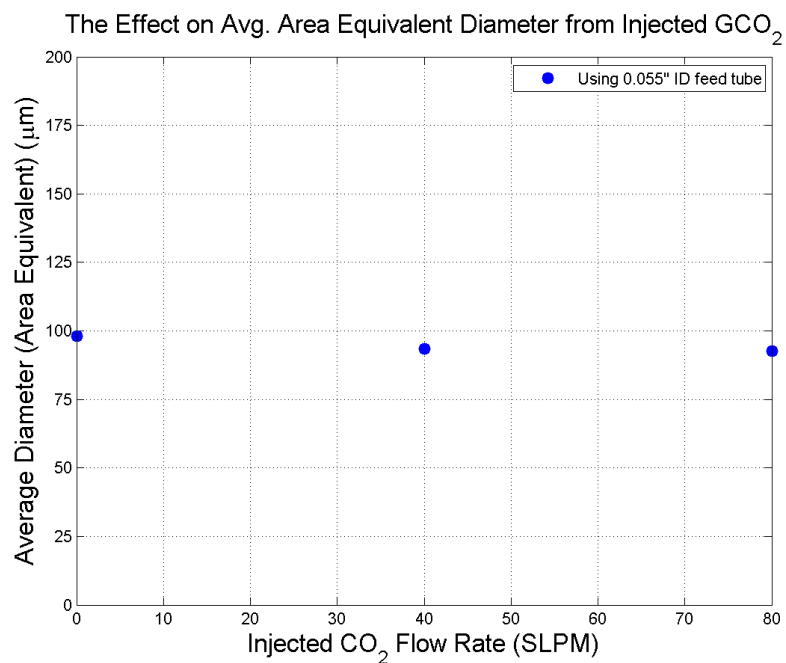**Figure C.4:** Particle statistics: effect of injected air on Sauter mean diameter

Figure C.5: Particle statistics: effect of injected gaseous CO_2 on average area-equivalent diameter
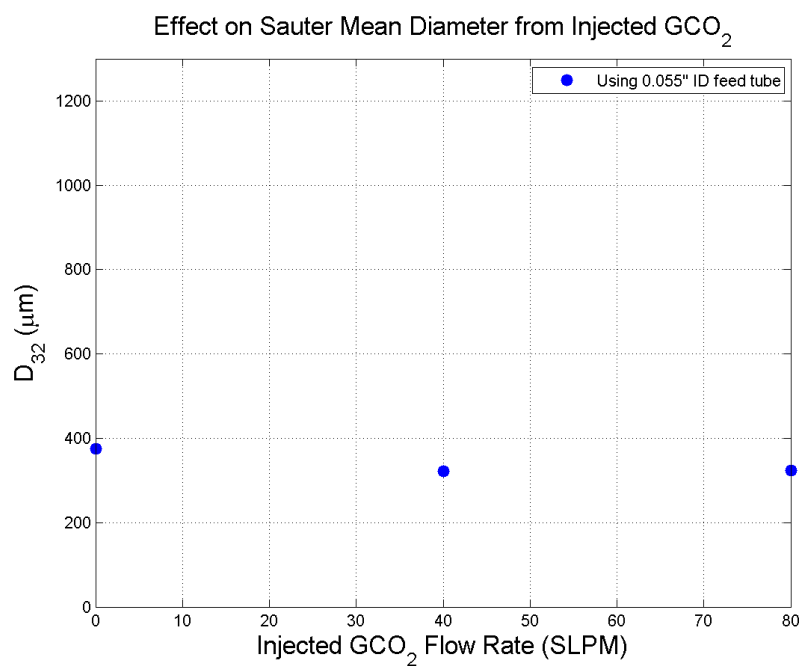
Figure C.6: Particle statistics: effect of gaseous CO_2 on Sauter mean diameter

Bibliography

[1] Garbrecht, G. *Hydrologic and Hydraulic Concepts in Antiquity in Hydraulics and Hydraulic Research: A Historical Review*. IAHR, Rotterdam, 1st edition, 1987.

[2] Raffel, M., C.E. Willert, S.T. Wereley, and J. Kompenhans. *Particle Image Velocimetry: A Practical Guide*. Springer, Verlag, 2nd edition, 2007.

[3] Tropea, C., A.L. Yarin, and J. Foss. *Springer Handbook of Experimental Fluid Mechanics*. Springer, Verlag, 1st edition, 2007.

[4] Adrian, R.J. "Twenty Years of Particle Image Velocimetry". *Experiments in Fluids*, 39:159–169, 2005.

[5] Melling, A. "Tracer Particles and Seeding for Particle Image Velocimetry". *Measurement Science and Technology*, 39:1406–1416, 1997.

[6] S. A. Resetar, R. W. Hess, J. Rogers. *Advanced Measurement Techniques at ONERA GMT (PIV Only)*. Technical report, ONERA, 1991.

[7] Adrian, R. and J. Westerweel. *Particle Image Velocimetry*. Cambridge, New York, 1st edition, 2011.

[8] Eaton, A.R., S.F. Frey, D.M Cusano, M.W. Plesniak, and P.E. Sojka. "Development of a Full-Field Planar Mie Scattering Technique for Evaluating Swirling Mixers". *Experiments in Fluids*, 21:325–330, 1996.

[9] LaVision. *FlowMaster*. LaVision, 2007.

[10] Reeder, M., J. Crafton, J. Estevadeordal, J. DeLapp, C. McNiel, D. Peltier, and T. Reynolds. "Clean Seeding for Flow Visualization and Velocimetry Measurements". *Experimental Fluids*, 48:889–900, 2010.

[11] Szeliga, M. R. "S-PIV-3D". http://www.uepg.br/denge/lhc/pivs3d.htm. [Online; accessed 26 Jan 2014].

[12] Wolfe, D.B. *Boundary Layer Measurements in the Trisonic Gas-Dynamics Facility Using Particle Image Velocimetry With CO2 Seeding*. Air Force Institute of Technology, 2012.

[13] Theunissen, R., A. Stitou, and M. Riethmuller. "A Novel Approach to Improve the Accuracy of PTV Methods". *Experiments in Fluids*, 21:325–330, 1996.

[14] Estevadeordal, J. and L. Goss. "PIV with LED: Particle Shadow Velocimetry (PSV)". *AIAA*. 2005.

[15] Estevadeordal, J. and L. Goss. "An Investigation Of Particle-Shadow Velocimetry (PSV) For Transonic-Flow Applications". *35th AIAA Fluid Dynamics Conference and Exhibit*. 2005.

[16] Estevadeordal, J. and L. Goss. "Particle Shadow Velocimetry". http://www.freepatentsonline.com/y2006/0175561.html, August 2006. [Online; accessed 1 Jan 2014].

[17] Ehrman, S. "Particle Size Analysis". http://terpconnect.umd.edu/~sehrman/particle-class/PSA-05-1-and2.ppt. [Online; accessed 26 Jan 2014].

[18] Love, B.T. *Particle Size Control for PIV Seeding Using Dry Ice*. Master's thesis, 2010.

[19] Masutti, D., S. Bernhardt, C. O. Asma, and M. R. Vetrano. "Experimental Characterization of Liquid Jet Atomization in Mach 6 Crossflow". *39th AIAA Fluid Dynamics Conference*. 2009.

[20] Kochtubajda, B. and E.P. Lozowsi. "The Sublimation of Dry Ice Pellets Used for Cloud Seeding". *Journal of Climate and Applied Meteorology*, 24:597–605, 1985.

[21] White, F. *Viscous Fluid Flow*. McGraw-Hill Higher Education, New York, 3rd edition, 2005.

[22] Pope, S. *Turbulent Flows*. Cambridge University Press, New York, 1st edition, 2000.

[23] DeLapp, C.J. *Particle Image Velocimetry Using Novel, Non-Intrusive Particle Seeding*. Master's thesis, 2006.

[24] McNiel, C.M. *Demonstration of Clean Particle Seeding For Particle Image Velocimetry in a Closed Circuit Supersonic Wind Tunnel*. Master's thesis, 2007.

[25] Greene, B.G. *Characterization and Control of Carbon Dioxide Seed Particles in Particle Image Velocimetry*. Master's thesis, 2008.

[26] Ostendorp, H. *Educational Wind Tunnel (EWT) System Brochure*. Aerolab, 2005.

[27] Ostendorp, H. *Educational Wind Tunnel (EWT) Owner's Manual*. Aerolab, 2005.

[28] Kumara, J., K. Hayano, and K. Ogiwara. "Image Analysis Techniques on Evaluation of Particle Size Distribution of Gravel". *Internation Journal of GEOMATE*, 3:2186–2990, 2012.

[29] Nuwaysir, E., W. Huang, and T. Albert. "Gene Expression Analysis Using Oligonucleotide Arrays Produced by Maskless Photolithography". *Genome Research*, 12:1749–1755, 2002.

[30] Rasband, Wayne. *ImageJ User Guide*. National Institutes of Health, USA, 2012.

[31] *A Basic Guide to Particle Characterization*. Technical report, Malvern Instruments Limited, 2012.

[32] "Carbon Dioxide". https://www.mathesongas.com/industrialgas/pdfs/bulk-carbon-dioxide.pdf. [Online; accessed 11 Mar 2014].

REPORT DOCUMENTATION PAGE

Form Approved
OMB No. 0704–0188

1. REPORT DATE *(DD–MM–YYYY)*
27–03–2014

2. REPORT TYPE
Master's Thesis

3. DATES COVERED *(From — To)*
Sep 2013–Mar 2014

4. TITLE AND SUBTITLE

Measurement and Image Processing Techniques for Particle Image Velocimetry Using Solid-Phase Carbon Dioxide

5a. CONTRACT NUMBER

5b. GRANT NUMBER

5c. PROGRAM ELEMENT NUMBER

6. AUTHOR(S)

Liber, Mei-Ling, Captain, USAF

5d. PROJECT NUMBER

5e. TASK NUMBER

5f. WORK UNIT NUMBER

7. PERFORMING ORGANIZATION NAME(S) AND ADDRESS(ES)

Air Force Institute of Technology
Graduate School of Engineering and Management (AFIT/EN)
2950 Hobson Way
WPAFB, OH 45433-7765

8. PERFORMING ORGANIZATION REPORT NUMBER

AFIT-ENY-14-M-32

9. SPONSORING / MONITORING AGENCY NAME(S) AND ADDRESS(ES)

Larry Leny
AFRL/RQ
2130 Eighth Street
WPAFB, OH 45433
lawrence.leny@wpafb.af.mil

10. SPONSOR/MONITOR'S ACRONYM(S)

11. SPONSOR/MONITOR'S REPORT NUMBER(S)

12. DISTRIBUTION / AVAILABILITY STATEMENT

DISTRIBUTION STATEMENT A:
APPROVED FOR PUBLIC RELEASE; DISTRIBUTION UNLIMITED

13. SUPPLEMENTARY NOTES

This work is declared a work of the U.S. Government and is not subject to copyright protection in the United States.

14. ABSTRACT

Proper seeding material for particle image velocimetry (PIV) should not contaminate closed circuit wind tunnels and minimize residual deposits on walls. Solid carbon dioxide (dry ice) particles are ideally suited to meet this requirement. However, to obtain accurate velocity measurements, either particle size must be controlled or advanced image filtering and processing must be implemented. Both of these approaches are explored and advanced in the following research. Refined data processing was conducted on previously collected turbulent boundary layer PIV data utilizing a similar particle generation system. The re-processed data trended more closely with corresponding pitot probe data than the original results. Free stream velocity measurements were within 0.97% of wind tunnel data free stream calculations. Particle sizing measurements of solid-phase carbon dioxide (CO_2) were demonstrated in bench test experiments using an image-based approach. Dry air and gaseous CO_2 were introduced into a specific CO_2 injector in an attempt to control particle diameter, for diameters that ranged from 20 μm to 2800 μm. Average particle diameter was represented by an area-equivalent diameter and Sauter mean diameter. The greatest reduction in particle diameter was measured using dry air in conjunction with the CO_2 injector, where a 21% decrease in average area-equivalent diameter was observed. In contrast, there was only about an 8% decrease in the average area-equivalent diameter with gaseous CO_2.
Dry air was introduced into the same CO_2 injector for particle sizing experiments in the test section of an Air Force Institute of Technology (AFIT) Educational Wind Tunnel (EWT). Shadow images were taken at the inlet section of the EWT and at the test section for a comparison of the particle size distribution at each location. Changes in particle size with free stream velocity and increased mass flow rates of air were observed.

15. SUBJECT TERMS

Particle Image Velocimetry, Particle Shadow Velocimetry, Turbulent Boundary Layer, ImageJ

16. SECURITY CLASSIFICATION OF:

a. REPORT	b. ABSTRACT	c. THIS PAGE
U	U	U

17. LIMITATION OF ABSTRACT
UU

18. NUMBER OF PAGES
153

19a. NAME OF RESPONSIBLE PERSON
Dr. Mark F. Reeder (ENY)

19b. TELEPHONE NUMBER *(include area code)*
(937) 255-3636 x 4530 mark.reeder@afit.edu

Standard Form 298 (Rev. 8–98)
Prescribed by ANSI Std. Z39.18